Department of Physics and Astronomy
University of Heidelberg

Master thesis in Physics
handed in by

Daniel Unverzagt

born in Frankfurt, Germany

Sept 2019

Measurement of time-dependent Charge-Parity asymmetries in neutral charm meson decays

This Master thesis has been carried out by Daniel Unverzagt at the
Physikalisches Institut Heidelberg
under the supervision of
Prof. Dr. Ulrich Uwer

Abstract

In this thesis the measurement of the time-dependent *CP* asymmetries in $D^0 \to \pi^+\pi^-$ and $D^0 \to K^+K^-$ decays using proton-proton collision data corresponding to 5.4 fb^{-1} of integrated luminosity is presented. The data has been taken with the LHCb detector during the years 2016-2018 at a center-of-mass energy of 13 TeV. Neutral D^0 mesons that arise from semileptonic decays of b-flavoured hadrons, where the charge of the accompanying muon identifies the flavour of the charm meson at the time of production, are used. The time-dependent *CP* asymmetry manifests itself in the parameter A_Γ, the asymmetry of the effective lifetime in decays of D^0 and $\overline{D}^0$ to *CP* eigenstates. A_Γ is measured in both decays to be:

$$A_\Gamma(D^0 \to \pi^+\pi^-) = (\ \ 2.2 \pm 7.0 \pm 0.8) \times 10^{-4},$$
$$A_\Gamma(D^0 \to K^+K^-) = (-4.3 \pm 3.6 \pm 0.5) \times 10^{-4},$$

with statistic and systematic uncertainties, respectively. The measurement is consistent with the hypothesis of CP conservation.

Zusammenfassung

In dieser Arbeit wird die Messung der zeitabhängigen *CP*-Asymmetrien bei $D^0 \to \pi^+\pi^-$ und $D^0 \to K^+K^-$ Zerfällen mit Proton-Proton-Kollisionsdaten, die 5,4 fb^{-1} integrierter Luminositat entsprechen, vorgestellt. Die Daten wurden mit dem LHCb-Detektor in den Jahren 2016-2018 bei einem Massenschwerpunktenergie von 13 TeV aufgenommen. Neutrale D^0-Mesonen, die durch semileptonische Zerfälle von b-flavoured Hadronen entstehen, bei denen die Ladung des begleitenden Myons den flavour des Charme-Mesons zum Zeitpunkt der Herstellung identifiziert, werden verwendet. Die zeitabhängige *CP*-Asymmetrie manifestiert sich im Parameter A_Γ, die Asymmetrie der effektiven Lebensdauer bei Zerfällen von D^0 und $\overline{D}^0$ zu *CP*-Eigenzuständen. A_Γ wird in beiden Zerfällen gemessen und ist:

$$A_\Gamma(D^0 \to \pi^+\pi^-) = (\ \ 2.2 \pm 7.0 \pm 0.8) \times 10^{-4},$$
$$A_\Gamma(D^0 \to K^+K^-) = (-4.3 \pm 3.6 \pm 0.5) \times 10^{-4},$$

mit statistischen und systematischen Unsicherheiten, jeweils. Die Messung steht im Einklang mit der Hypothese der CP-Erhaltung.

Preface

The results shown in this thesis have been approved for publication in a peer-reviewed journal by the LHCb collaboration and a paper is currently in preparation:

- "Updated measurement of decay-time-dependent *CP* asymmetries in $D^0 \to K^+K^-$ and $D^0 \to \pi^+\pi^-$ decays", to be submitted to Physical Review D [1].

The author of this thesis is the main person responsible of the analysis work presented in the above planned publication. The analysis was performed with a small analysis team within the LHCb collaboration. The LHCb collaboration is an international association of more than 1200 scientists and engineers from 77 institutes in 17 countries. This implies the usage of common software to analyse the data collected by the LHCb experiment. Both the collection of the data and the development of common software used to analyse the data result from the effort of many current and former collaboration members. For this analysis the already preselected data from the measurement presented in Ref. [2] is used. A more technical and detailed description of the analyses is available internally to the LHCb collaboration in Ref. [3].

Contents

1 Introduction

The goal of particle physics is to describe matter and its interactions. Currently, there are many open questions in particle physics. So far two well established theories are used to describe most fundamental physics processes. One to describe gravity and interactions at large scales and secondly the Standard Model of particle physics (SM) which describes the three fundamental forces, which are the weak, strong and electromagnetic interaction. No significant deviations from its predictions have been observed so far. However, there are many reasons to doubt that the SM will be the final model. One of these open questions is the large matter-antimatter asymmetry in the universe predicted by current astronomical observations [4]. Proposed by Sakharov [5], three so called "Sakharov conditions" have to be fulfilled in order to explain the large matter-antimatter asymmetry:

1. Interactions out of thermal equilibrium
2. Baryon number violation
3. Charge conjugation Parity violation (*CP* violation)

In particular, the last condition, the amount of *CP* violation necessary to produce such large baryonic asymmetry in the universe, cannot be explained by the SM [4]. The only source of *CP* violation in the SM today arises from the irreducible complex phase used in the parametrisation of the Cabibbo-Kobayashi-Maskawa (CKM) quark mixing matrix, which quantifies the strength of the coupling between quarks in the weak interaction [1].

High precision measurements of processes involving higher order quantum loops are a method to test the SM as they are a promising source to observe the effect of new physic contributions. These new physics contributions can, in the form of new particles, introduce additional sources of *CP* violation or enhance the rate of such processes and therefore might manifest themselves at energies much lower than the typical energy scale of the new particles.

This motivates the interest for high precision measurements of *CP* violation in the decays of particles containing charm quarks. The SM contribution to *CP* violation in D^0 ($c\overline{u}$) meson decays is very small $\mathcal{O}(10^{-3})$, since mainly quarks of the first two generations are involved and the corresponding part of the CKM matrix is real in the lowest order. As a consequence, charm decays are of interest as they might be subject to new phenomena of *CP* violation.

[1] Technically *CP* violation would also be possible for the strong interaction in the SM, but so far no evidence of *CP* violation has been detected. This absence of *CP* violation is often referred to as *strong CP problem*.

Just this year for the first time ever direct *CP* violation in the charm sector has been observed, by measuring the difference of time-integrated *CP* asymmetries in $D^0 \to K^+K^-$ and $D^0 \to \pi^+\pi^-$ decays at LHCb [6].

This thesis presents the measurement of the time-dependent *CP* asymmetry (A_Γ) in $D^0 \to K^+K^-$ and $D^0 \to \pi^+\pi^-$ from semileptonic B-decays.

The structure of the thesis is as follows: In section 2, the theoretical background is presented, focusing on the mixing formalism of neutral mesons and the *CP* observable A_Γ. Additionally, the measurement procedure to extract A_Γ is presented. The LHC accelerator with special interest in the LHCb detector is described in section 3. Section 4 discusses the decay topology and how decay candidates are reconstructed and selected. From these selected decays then the time-dependent asymmetry A_Γ is estimated by a simultaneous χ^2 fit, as explained in section 5. Afterwards, with the help of pseudo experiments, all dominant systematic uncertainties are estimated as explained in section 6. In section 7 several crosschecks are presented to test the robustness of the measurement and search for possible neglected systematic biases, followed by a brief summary in section 8.

2 Phenomenology of neutral meson mixing and *CP* violation

This chapter covers the theoretical background needed for the measurement of the CP violation sensitive observable A_Γ.

First the mixing formalism for neutral mesons is introduced and the phenomenology of the mixing phenomena is shortly described. The classifications in which *CP* violation manifests itself are explained. Afterwards, the observable A_Γ is introduced and the analysis procedure to measure A_Γ in semileptonicly tagged charm decays is explained.

2.1 Neutral meson mixing

Mesons are subatomic particles composed of one quark and one anti-quark, bound together by strong interactions. Mesons made of two different kind of quarks are usually referred to as flavoured mesons with a corresponding flavour quantum number.

In the SM four neutral mesons, K^0 ($d\bar{s}$), D^0 ($c\bar{u}$), B^0 ($d\bar{b}$), and B_s^0 ($s\bar{b}$), can mix with their antiparticles. These particles are produced as flavour eigenstates. These neutral mesons are not eigenstates of the free Hamiltonian governing the time evolution, owing to the violation of the flavour quantum number by the weak interaction. As a consequence the neutral mesons have a certain probability to oscillate into their antiparticles and vice versa before decaying, the so called *mixing phenomena*.

The initial state, at $t_0 = 0$, is given by a pure superposition of neutral mesons in their flavour eigenstates M^0 and $\overline{M}^0$, for particle and antiparticle, respectively, where M^0 corresponds to D^0, K^0, B^0 or B_s^0:

$$|\psi(t_0)\rangle = a(t_0)\,|M^0\rangle + b(t_0)\,|\overline{M}^0\rangle \tag{2.1}$$

For times larger than the typical strong interaction timescale ($10^{-22}s$), it is possible to determine the time evolution by a 2×2 effective Hamiltonian $\mathbf{H}$ [7] . The Hamiltonian is not Hermitian, otherwise the mesons would only oscillate and not decay, and can therefore be written in terms of two Hermitian matrices $\mathbf{M}$ and $\mathbf{\Gamma}$, with their corresponding elements $\mathrm{M_{ij}}$ and Γ_{ij}. The state itself will evolve over time by the Schrödinger equation given by:

$$ih\frac{\mathrm{d}}{\mathrm{d}t}\Psi(t) = \mathbf{H}\Psi(t), \quad \mathbf{H} = \mathbf{M} - \frac{i}{2}\mathbf{\Gamma} \tag{2.2}$$

The diagonal elements of $\mathbf{M}$ and $\mathbf{\Gamma}$ are associated to $M^0 \to M^0$ and $\overline{M}^0 \to \overline{M}^0$ transitions, whereas the off-diagonal elements are associated to flavour changing $M^0 \to \overline{M}^0$ and

$\overline{M}^0 \to M^0$ transitions. The time evolution is given by the superposition of the flavour eigenstates and all final states $|f_k\rangle$:

$$|\psi(t)\rangle = a(t)\,|M^0\rangle + b(t)\,|\overline{M}^0\rangle + \sum_k c_k(t)\,|f_k\rangle \tag{2.3}$$

The mass eigenstates of $\mathbf{H}$ have well-defined masses (m_+, m_-) and decay widths (Γ_+, Γ_-). For the case of CPT invariance, like given in the SM, the eigenstates are defined by:

$$\begin{aligned} M_- &= p\,|M^0\rangle + q\,|\overline{M}^0\rangle\,, \\ M_+ &= p\,|M^0\rangle - q\,|\overline{M}^0\rangle \end{aligned} \tag{2.4}$$

with

$$\frac{q}{p} = -\sqrt{\frac{\mathrm{M}_{12}^* - \frac{i}{2}\Gamma_{12}^*}{\mathrm{M}_{12} - \frac{i}{2}\Gamma_{12}}}, \tag{2.5}$$

additionally, holds $M := M_{11} = M_{22}$ and $\Gamma := \Gamma_{11} = \Gamma_{22}$. The corresponding eigenvalues are given by:

$$\lambda_\mp = \mathrm{M} \pm \frac{q}{p}\mathrm{M}_{12} - \frac{i}{2}\left(\Gamma \pm \frac{q}{p}\Gamma_{12}\right) := m_\mp - \frac{i}{2}\Gamma_\mp \tag{2.6}$$

Solving the Schrödinger equation yields the following time evolution for the mass eigenstates:

$$|M_\mp(t)\rangle = e^{im_\mp t}e^{-\Gamma_\mp \frac{t}{2}}\,|M_\mp(t_0)\rangle \tag{2.7}$$

The time evolution of a particle, which is created at t_0, is obtained by substituting the time-evolution of $|M_\mp(t)\rangle$ into the definition of $M_\mp$:

$$\begin{aligned} |M^0(t)\rangle &= g_+(t)\,|M^0(t_0)\rangle + g_-(t)\frac{q}{p}\,|\overline{M}^0(t_0)\rangle\,, \\ |\overline{M}^0(t)\rangle &= g_+(t)\,|\overline{M}^0(t_0)\rangle + g_-(t)\frac{p}{q}\,|M^0(t_0)\rangle \end{aligned} \tag{2.8}$$

with

$$g_\pm(t) = \frac{1}{2}\left(e^{-i\lambda_- t} \pm e^{-i\lambda_+ t}\right) \tag{2.9}$$

With help of equation 2.8, it is possible to calculate the probability of the flavour state during the decay. The probability to measure a state with the same flavour after a time t is given by:

$$\begin{aligned} |\,\langle M^0(t)|M^0(t_0)\rangle\,|^2 &= |g_+(t)|^2 \\ |\,\langle \overline{M}^0(t)|\overline{M}^0(t_0)\rangle\,|^2 &= |g_+(t)|^2 \end{aligned} \tag{2.10}$$

and the probability to measure a state with opposite flavour than the initial flavour state is given by:

$$\begin{aligned} |\langle M^0(t)|\overline{M}^0(t_0)\rangle|^2 &= \left|\frac{q}{p}\right|^2 |g_-(t)|^2 \\ |\langle \overline{M}^0(t)|M^0(t_0)\rangle|^2 &= \left|\frac{p}{q}\right|^2 |g_-(t)|^2 \end{aligned} \tag{2.11}$$

with

$$|g_\pm(t)|^2 = \frac{1}{2}e^{-\Gamma t}\left[\cosh\left(\frac{\Delta\Gamma t}{2}\right) \pm \cos(\Delta m t)\right] \tag{2.12}$$

where $\Delta m := m_+ - m_-, \quad \Delta\Gamma := \Gamma_+ - \Gamma_-$. Equation 2.12 is often expressed in terms of the *mixing parameters* $x := \frac{\Delta m}{\Gamma}$ and $y := \frac{\Delta\Gamma}{2\Gamma}$:

$$|g_\pm(t)|^2 = \frac{1}{2}e^{-\Gamma t}\left[\cosh\left(y\Gamma t\right) \pm \cos(x\Gamma t)\right] \tag{2.13}$$

The probability for a neutral meson to conserve its flavour is equal for M^0 and $\overline{M}^0$ over time, whereas the probability to oscillate in their antiparticle can be different if $|q/p| \neq 1$. Although the formalism is similar for all neutral mesons, the phenomenology is quite different for the neutral mesons, owing to the different matrix elements of the effective Hamiltonian $\mathbf{H}$ and the resulting mixing parameters x and y, see Table 1. In Figure 1 the resulting probability, as function of decay-time, for the neutral mesons to oscillate into their antiparticles or preserve their flavour quantum number is demonstrated. Particular for the D^0, the probability to oscillate into its antiparticle is very small.

System	$x = \Delta m/\Gamma$	$y = \Delta\Gamma/2\Gamma$
K^0-$\overline{K}^0$	-0.95	0.997
D^0-$\overline{D}^0$	0.003	0.007
B^0-$\overline{B}^0$	0.77	-0.001
B_s^0-$\overline{B}_s^0$	26.7	0.06

Table 1: Approximate mixing parameters of the four flavoured neutral meson systems. Values taken from Ref. [8–11].

In general, there are two types of contributions to the mixing amplitudes, *long distance contribution* and *short distance contribution*. The short distance contribution are from intermediate virtual particles as illustrated in Figure 2 on the right. Whereas, the long distance contribution, to the mixing, arise from intermediate real particles as illustrated in Figure 2 on the left. Both contributions involve weak interaction processes.

2.2 *CP* violation in particle physics

The *CP* transformation is the combination of charge conjugation and parity transformation. Charge conjugation interchanges particles with their antiparticles whereas parity transformation flips the sign of the spatial coordinates. A general state transforms under the *CP* transformation as $CP\,|f\rangle = \omega_f\,|\overline{f}\rangle$, where ω_f is a complex phase ($|\omega_f| = 1$). In the special case that f is a *CP* eigenstate f_{CP} ($f_{CP} = \pi^+\pi^-$ and $f_{CP} = K^+K^-$ are *CP* eigenstates), one obtains:

$$CP\,|f\rangle = \eta_{CP}\,|f\rangle \tag{2.14}$$

with $\eta_{CP} = \pm 1$ for CP-even and CP-odd states, respectively.

From now on the decay amplitudes of M^0 and $\overline{M}^0$ to a final state f or $\overline{f}$ will be denoted as:

$$A_f = \langle f|\mathcal{H}|M^0\rangle\,, \quad \overline{A}_f = \langle f|\mathcal{H}|\overline{M}^0\rangle\,, \quad A_{\overline{f}} = \langle \overline{f}|\mathcal{H}|M^0\rangle\,, \quad \overline{A}_{\overline{f}} = \langle \overline{f}|\mathcal{H}|\overline{M}^0\rangle$$

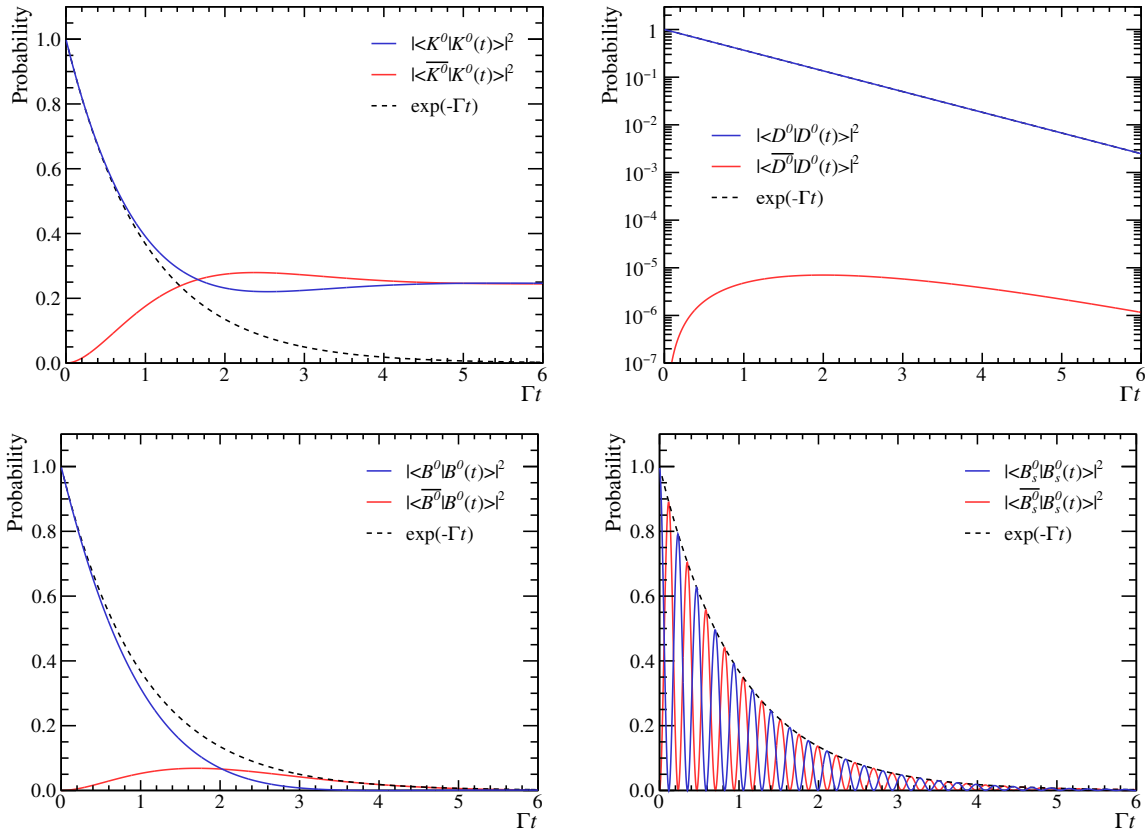

Figure 1: Probability for a meson to oscillate in its anti-meson (red) or to preserve its flavour(blue) as a function of its proper time, for the four different neutral mesons, K^0, D^0, B^0 and B_s^0. The black dashed line is the exponential function which would be measured in absence of mixing. Note the logarithmic scale in the plot for the D^0-$\overline{D}^0$ mixing. The figure is taken from Ref. [12].

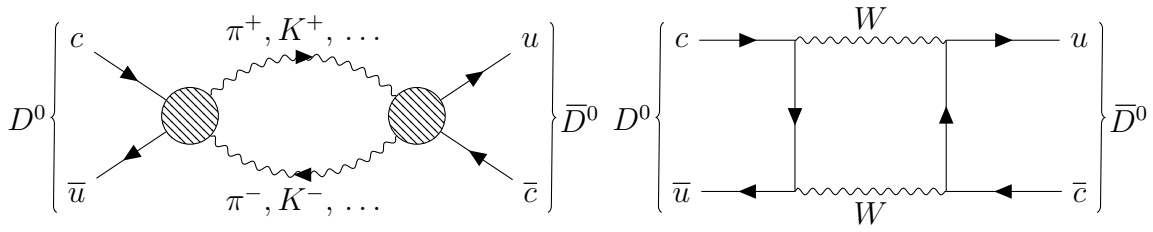

Figure 2: Long distance contribution via intermediate particles, on the left, and the short distance box-diagram, on the right.

where $\mathcal{H}$ is the decay Hamiltonian of the neutral meson.

CP transformation of an individual decay amplitude does not change its absolute value but at most the phase of the amplitude. The phase for a decay amplitude can therefore be split into a *CP*-odd phase, *weak phase*, and a *CP*-even phase, *strong phase*. For example, consider a process which proceeds through several amplitudes a_i:

$$A_f = \sum_i |a_i| e^{i(\delta_i + \phi_i)}, \quad \overline{A}_{\overline{f}} = \sum_i |a_i| e^{i(\delta_i - \phi_i)}$$

with weak phase ϕ_i and strong phase δ_i. The difference between an original and its *CP*-conjugated total amplitude squared is:

$$|A_f|^2 - |\overline{A}_{\overline{f}}|^2 = -2 \sum_{i,j} |a_i||a_j| \sin(\phi_i - \phi_j) \sin(\delta_i - \delta_j) \tag{2.15}$$

Therefore, by definition, it is only possible to observe *CP* violation if at least two amplitudes with different weak *and* strong phases are present.

2.3 Phenomenology of *CP* violation

Experimentally, there are three possibilities for CP violation to occur, *CP* violation in decay, *CP* violation in mixing and *CP* violation in interference between decay with and without mixing.

2.3.1 *CP* violation in decay

CP violation in decay occurs if the magnitude of the decay amplitude for *CP* conjugated processes are not equal *i.e.*:

$$R_f := \left| \frac{\overline{A}_{\overline{f}}}{A_f} \right| \neq 1$$

This type of CP violation is often quantified by the direct CP asymmetry $\mathcal{A}_{CP}^{\text{dir}}$, given by:

$$\mathcal{A}_{CP}^{\text{dir}} := \frac{|A_f|^2 - |\overline{A}_{\overline{f}}|^2}{|A_f|^2 + |\overline{A}_{\overline{f}}|^2} = \frac{1 - R_f^2}{1 + R_f^2} \tag{2.16}$$

CP violation in decay is often referred to as direct *CP* violation.

2.3.2 *CP* violation in mixing

CP violation in mixing occurs if the mixing probability for a meson M^0 after a time t to oscillate to $\overline{M}^0$ is different from this of its antiparticle. Therefore, for *CP* violation in mixing, by equation 2.11, is required that:

$$R_m := \left|\frac{q}{p}\right| \neq 1$$

2.3.3 Interference between decay with and without mixing

CP violation in interference occurs if the *CP* symmetry is violated by the interference between the decay without mixing, $M^0 \to f$, and with mixing, $M^0 \to \overline{M}^0 \to f$. This is the case if

$$\mathcal{I}m(\lambda_f) + \mathcal{I}m(\lambda_{\overline{f}}) \neq 0 \tag{2.17}$$

with

$$\lambda_f := \frac{q}{p}\frac{\overline{A}_f}{A_f}. \tag{2.18}$$

This simplifies for the final CP eigenstates K^+K^- and $\pi^+\pi^-$ to

$$\mathcal{I}m(\lambda_{f_{CP}}) \neq 0. \tag{2.19}$$

In this case λ_f is usually written as

$$\lambda_f = -\eta_{CP}(f) \cdot R_m R_f e^{i\phi_f} \tag{2.20}$$

where $\eta_{CP}(f)$ is the *CP*-parity of the final state and the phase ϕ_f is defined by:

$$\phi_f := \arg\left(-\eta_{CP}(f) \cdot \frac{q}{p}\frac{\overline{A}_f}{A_f}\right) \tag{2.21}$$

For *CP* in interference therefore is required that $\phi_f \neq \{0, \pi\}$.

2.4 CP violation in the D^0 system and A_Γ

In the following the discussion is now specialised to $D^0 \to \pi^+\pi^-$ and $D^0 \to K^+K^-$ decays, whereas the final *CP* eigenstates $\pi^+\pi^-$ and K^+K^- are denoted as f_{CP}.

2.4.1 Time-dependent *CP* asymmetry

A useful observable for D^0-mixing is the asymmetry of the decay rate in D^0 and $\overline{D}^0$ to final states f_{CP}. The time-dependent *CP* asymmetry is defined by the asymmetry between the decay rates of the D^0 and $\overline{D}^0$ into final state f:

$$\mathcal{A}_{CP}(t) := \frac{\Gamma(D^0(t) \to f_{CP}) - \Gamma(\overline{D}^0(t) \to f_{CP})}{\Gamma(D^0(t) \to f_{CP}) + \Gamma(\overline{D}^0(t) \to f_{CP})} \tag{2.22}$$

The time-dependent decay rates of D^0 and $\overline{D}^0$ decays into final state f are defined as:

$$\Gamma(D^0(t) \to f) = N_f |\langle f_{CP}|\mathcal{H}|D^0(t)\rangle|^2, \qquad \Gamma(\overline{D}^0(t) \to f) = N_f |\langle f_{CP}|\mathcal{H}|\overline{D}^0(t)\rangle|^2 \tag{2.23}$$

N_f is a common, time-independent normalisation factor. By inserting the above equations into the definition of $\mathcal{A}_{CP}$ and using equation 2.13, $\mathcal{A}_{CP}$ can be rewritten as:

$$\mathcal{A}_{CP}(t) = \mathcal{A}_{CP}^{\text{dir}} + \mathcal{A}_{CP}^{\text{ind}} \cdot \Gamma t + \mathcal{O}((x\Gamma t)^2) + \mathcal{O}((y\Gamma t)^2). \tag{2.24}$$

$\mathcal{A}_{CP}^{\text{dir}}$, defined in equation 2.16, is only non-zero if *CP* violation in decay is present ($R_f \neq 1$), whereas the slope of $\mathcal{A}_{CP}$ is given by

$$\mathcal{A}_{CP}^{\text{ind}} := -\frac{2\eta_{CP}(f_{CP})R_f^2}{(1+R_f^2)^2}\left[(R_m R_f + R_m^{-1}R_f^{-1})y\cos\phi_f - (R_m R_f + R_m^{-1}R_f^{-1})x\sin\phi_f\right] \tag{2.25}$$

and therefore sensitive to all three sources of *CP* violation. For more details on the derivation see appendix A.1.

2.4.2 Observable A_Γ

A_Γ is defined as the asymmetry between the effective lifetimes of initially produced D^0 and $\overline{D}^0$ mesons decaying into *CP*-even final states:

$$A_\Gamma := \frac{\hat{\tau}(\overline{D}^0 \to f_{CP}) - \hat{\tau}(D^0 \to f_{CP})}{\hat{\tau}(\overline{D}^0 \to f_{CP}) + \hat{\tau}(D^0 \to f_{CP})} \tag{2.26}$$

$\hat{\tau} = 1/\hat{\Gamma}$ is the effective lifetime as obtained from the decay-time spectrum assuming an exponential decay law. Among all *CP* violating observables is A_Γ one of the more promising observables. Especially as most potential systematic effects are constant in time and therefore, by construction, only have a small to non-existing influence to the measurement. By inserting the effective lifetime into the definition of A_Γ follows:

$$A_\Gamma = \frac{\eta_{CP}(f)}{2}\left[(R_m R_f + R_m^{-1}R_f^{-1})y\cos\phi_f - (R_m R_f + R_m^{-1}R_f^{-1})x\sin\phi_f\right] \tag{2.27}$$

From this expression it is possible to see that A_Γ receives contributions from *CP* violation in decay (R_f), in mixing (R_m) and in interference (ϕ_f). The above expression can now be further simplified by inserting the definition of $\mathcal{A}_{CP}^{\text{ind}}$.

$$A_\Gamma = -\frac{1}{4}\frac{\left(1+R_f^2\right)^2}{R_f^2}\cdot\mathcal{A}_{CP}^{\text{ind}} \approx -\mathcal{A}_{CP}^{\text{ind}} \tag{2.28}$$

The above approximation uses that the current experimental values for direct *CP* violation of $\mathcal{O}(10^{-3})$ [2] allow to neglect the contribution of R_f ($R_f \approx 1$). Therefore, by equation 2.24, A_Γ is the negative slope of the linearised *CP* asymmetry over the decay-time t/τ_{D^0}, where τ_{D^0} is the lifetime of the D^0.

$$\mathcal{A}_{CP}(t) = \mathcal{A}_{CP}^{\text{dir}} - A_\Gamma\frac{t}{\tau_{D^0}} \tag{2.29}$$

For a more detailed derivation please see appendix A.2. Using the same approximation as above A_Γ is expressed in the following way:

$$A_\Gamma = \frac{\eta_{CP}(f)}{2}\left[\left(R_m - R_m^{-1}\right)y\cos\phi_f - \left(R_m + R_m^{-1}\right)x\sin\phi_f\right] \tag{2.30}$$

A non-null value of A_Γ indicates indirect *CP* violation in the neutral charm system, produced either by *CP* violation in mixing or in the interference of decay with and without mixing or a mixture of both. The current theoretical prediction for indirect *CP* asymmetry in the SM are of $\mathcal{O}(10^{-4}-10^{-5})$ [13, 14] which is still far from any sensetivity of current experiments can reach. Therefore, if any asymmetry is observed with the present experimental precision it must come from *CP* violation introduced by new physics. In appendix A the full derivation of A_Γ as the negative slope of $\mathcal{A}_{CP}$ can be found.

2.5 How to measure A_Γ

A_Γ is measured by estimating the number of the different flavoured D^0 and $\overline{D}^0$ candidates in $D^0 \to \pi^+\pi^-$ ($D^0 \to K^+K^-$) decays time-dependently. The flavour of the D^0, in semileptonic decays of B hadrons, is identified by tagging the charge of the muon. The signal yield, or more precisely, directly the asymmetry between D^0 and $\overline{D}^0$ candidates is estimated by a fit to the mass spectrum to the D^0 and $\overline{D}^0$ spectrum. Both methods are in the following briefly explained. Finally, the decay-time is reconstructed with help of the measured decay vertices. For more details on the decay-time reconstruction see section 4.

2.5.1 Flavour tagging

To identify the D^0 and $\overline{D}^0$ mesons flavour tagging is used. Flavour tagging is a common tool in flavour physics which allows to identify the flavour of a particle. For this purpose

$B \to D\mu X$ decays are used, where X stands for any possible not reconstructed particle. It is possible to identify the flavour of the D meson by looking at $B \to D^0\mu^-\nu_\mu X$ and $\overline{B} \to \overline{D}^0\mu^+\nu_\mu X$ decays as the muon charge directly indicates the flavour of the D meson. In figure 3 schematically the decays $B^- \to D^0\mu^-\nu_\mu$ and $B^+ \to \overline{D}^0\mu^+\nu_\mu$ are outlined. As $B \to \overline{D}^0\mu^-\nu_\mu X$ and $\overline{B} \to D^0\mu^+\nu_\mu X$ decays are not allowed in the SM, a μ^- indicates a D^0 and a μ^+ a $\overline{D}^0$ candidate. The D^0 candidate is *semileptonically tagged*.

The same procedure is also possible using $D^{*+} \to D^0\pi^+$ decays, where the pion is used to identify the flavour of the D^0. The D^0 is called *promptly tagged*.

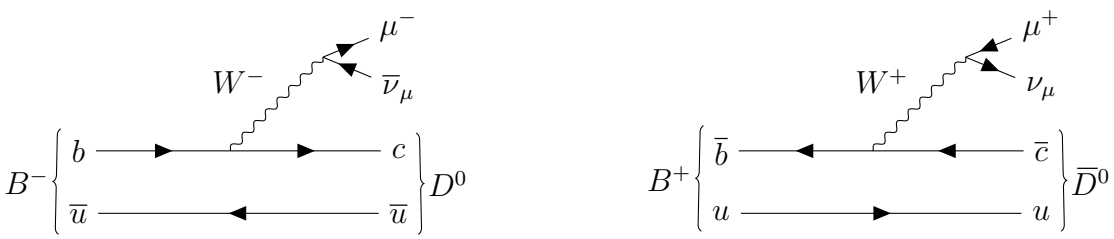

Figure 3: The leading Feynman diagram for $B \to D^0\mu^-\nu_\mu$ decays on the left. On the right the leading Feynman diagram for $B \to \overline{D}^0\mu^+\nu_\mu$ decays.

2.5.2 Estimating A_Γ

The raw asymmetry $\mathcal{A}_{raw}$ is the observed asymmetry between the number of D^0 and $\overline{D}^0$ mesons to final state f_{CP} decays and defined in the following way:

$$\mathcal{A}_{\text{raw}}(t) = \frac{N(D^0(t) \to f_{CP}) - N(\overline{D}^0(t) \to f_{CP})}{N(D^0(t) \to f_{CP}) + N(\overline{D}^0(t) \to f_{CP})}. \tag{2.31}$$

The asymmetry is constructed in such a way that most detector (*i.e.* detector efficiency) and other effects except of CP violating effects largely cancel out. For small asymmetries, it is possible to linearise the asymmetry in the following way:

$$\mathcal{A}_{\text{raw}}(t) = \mathcal{A}_{CP}(t) + A_{det} + A_{prod} + O(A^3) \tag{2.32}$$

The main contribution to $\mathcal{A}_{raw}$ are the time-dependent CP-violating asymmetry $\mathcal{A}_{CP}(t)$, the time-independent muon detection asymmetry A_{det}, which arises due to the fact that antiparticles interact differently with the detector material than particles and therefore, are differently detected. The production asymmetry A_{prod} arises from possible asymmetries in the number of produced B^+ and B^- candidates. Equation 2.29 approximates $\mathcal{A}_{CP}$ by a time-independent part and time dependent part:

$$\mathcal{A}_{CP}(t) = \frac{\Gamma(D^0(t) \to f_{CP}) - \Gamma(\overline{D}^0(t) \to f_{CP})}{\Gamma(D^0(t) \to f_{CP}) + \Gamma(\overline{D}^0(t) \to f_{CP})} \approx \mathcal{A}_{CP}^{\text{dir}} - \frac{t}{\tau_{D^0}} A_\Gamma \tag{2.33}$$

Where now the only time-dependent contribution of the raw asymmetry $\mathcal{A}_{\text{raw}}$ is A_Γ. This allows to directly measure the time-dependent asymmetry of the decay rate A_Γ by estimating the negative slope of the time-dependent raw asymmetry $\mathcal{A}_{\text{raw}}$. This simplifies the measurement tremendously as only the number of $D^0 \to f_{CP}$ and $\overline{D}^0 \to f_{CP}$ decays need to be estimated as function of decay-time.

$$\mathcal{A}_{\text{raw}}(t) = \mathcal{A}_{raw}(0) - \frac{t}{\tau_{D^0}} A_\Gamma \tag{2.34}$$

2.6 Measure procedure and blinding

The measurement of the time-dependent asymmetry can be divided into four different steps:

1. *Data selection.* A selection is applied to reduce backgrounds to obtain a clean data sample.

2. *Fit to the decay-time integrated mass spectrum.* All parameters for the mass shape are extracted from the decay-time integrated data sample.

3. *Fit in each decay-time bin.* The data is split in 20 approximately equally populated decay-time bins and $\mathcal{A}_{CP}(t)$ is estimated in every decay-time bin.

4. *Linear fit.* A linear fit to $\mathcal{A}_{CP}(t)$ is performed to directly extract A_Γ.

Before starting with performing these steps on $D^0 \to \pi^+\pi^-$ and $D^0 \to K^+K^-$ decays all steps will be validated with $D^0 \to K^-\pi^+$ decays. For $D^0 \to K^-\pi^+$ decays A_Γ is expected to be zero, this is used to validate the measurement procedure. Afterwards a common blinding is implemented for $D^0 \to \pi^+\pi^-$ and $D^0 \to K^+K^-$ decays. A blinding is used in most modern physics measurements to not introduce a bias by the observers expectations on the measurement. The blinding used in this measurement is directly applied to the linear fit of A_Γ. First, the measured slope is altered by a random number $a \in [-2, 2] \times 10^{-3}$ and then shifted by a constant $c \in [-2, 2] \times 10^{-2}$, to safely cover more than 5σ deviation from the world average of A_Γ.

$$\mathcal{A}_{raw}^{blind} = \mathcal{A}_{raw} + a \cdot < \frac{t}{\tau} > + c \tag{2.35}$$

This analysis was first performed blind and was afterward unblinded. All results shown are unblinded.

3 The LHCb experiment

This chapter briefly describes the LHC and in more detail the LHCb detector. The focus is on all relevant subsystems for the analysis presented in this thesis. A more detailed description of the experiment can be found in Ref. [15].

3.1 LHC

The Large Hadron Collider (LHC [16]), the largest circular accelerator in the world, is situated at the European Organization for Nuclear Research (CERN). The LHC is located inside a 27 km tunnel across the French and Swiss border and is designed to collide two beams of protons at a center of mass energy of around 13 TeV. The LHC is the end of a complex accelerator system which increases the energy of the beams to 450 GeV before they are injected to the LHC ring. The proton beams are kept on a circular orbit by superconducting magnets and brought to collision at four different points where the main experiments (CMS, ATLAS, ALICE and LHCb) are located. ATLAS and CMS are general purpose detectors which are designed to cover a wide spectrum of high energy physics. The ALICE experiment is specialised in study heavy ion collisions aiming to achieve a better understanding of QCD. The LHCb experiment is dedicated to measure the properties of c- and b-hadrons and their decays.

At the end of 2009 the LHC started with colliding protons. In 2010 and 2011 the LHC ran at a centre of mass energy of $\sqrt{s} = 7\,\text{TeV}$ and in 2012 with $\sqrt{s} = 8\,\text{TeV}$. The run period between 2010 and 2012 is referred to as Run 1. After Run 1 followed a long shut down period of two years on which modifications to the LHC dipole magnets have been performed with the goal to increase the center of mass energy at the LHC. The second run period between 2015-2018 is referred to as Run 2. In Run 2 a center of mass energy of 13 TeV was reached. At the end of 2018 another shut down was performed with the goal to prepare the detectors and the LHC for higher luminosities, which is planned to be followed by a third run period, Run 3.

Besides proton-proton collisions also proton-lead and lead-lead collisions were successfully realised at the LHC under a variety of specific operating conditions.

3.2 LHCb experiment

The LHCb detector is designed to study heavy b and c flavoured hadrons, *i.e.* heavy mesons consisting of a b-quark or c-quark. As bottom quarks typically decay within the detector, a large amount of c-hadrons are produced within the LHCb experiment. The

world largest samples of charm and bottom decays have been collected by LHCb, with the help of these data samples the LHCb collaboration has made significant contributions to the field of flavour physics. At the energies provided by the LHC heavy quarks, typically produced as $q\bar{q}$ pairs, are produced mainly in the forward region at the LHC, to measure these hadrons the LHCb detector is built as a forward spectrometer[2]. One of the main requirements to accurately measure decays of heavy flavoured hadrons is the capability to exactly measure the position of the primary vertex and the decay vertex of unstable heavy particles. An excellent resolution for the momenta of all final state particles and lastly the capability of particle identification is needed.

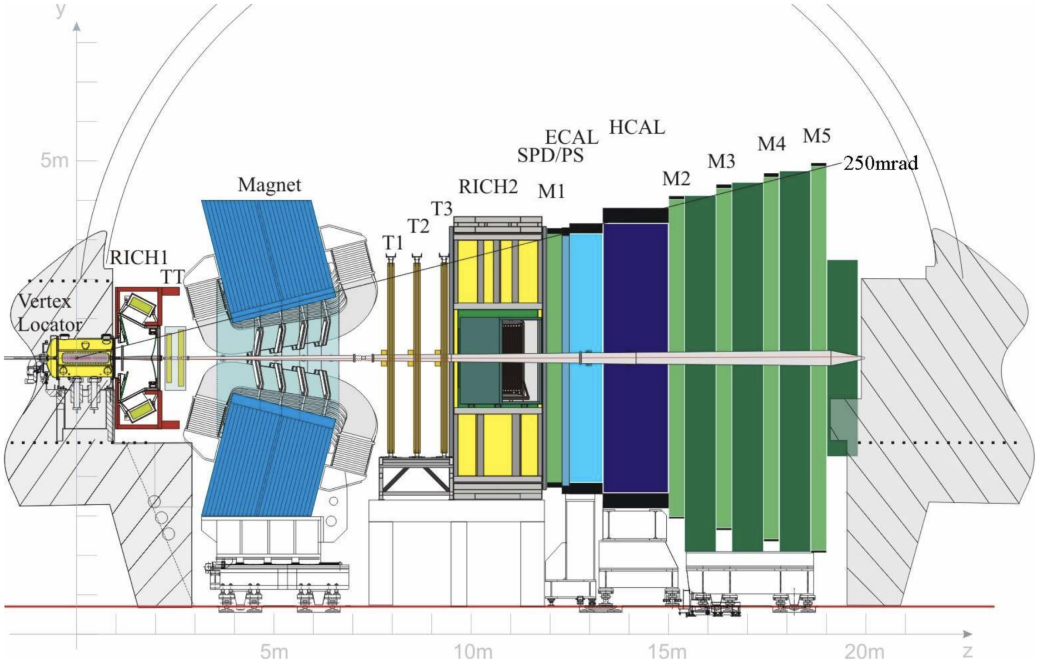

Figure 4: LHCb detector with its sub-system. The figure is taken from Ref. [15].

The LHCb detector with its various sub-systems is shown in figure 4. A right-handed cartesian coordinate system is used with the z-axis pointing in the direction of the beam, while the y-axis is pointing upwards.

3.2.1 Tracking system

For the correct reconstruction of the decay chain and all decay vertices the LHCb tracking system is responsible. A track is defined as the trajectory of a charged particle. The first

[2]Forward represents here both directions along the beam pipe. For practical reasons the LHCb detector is equipped only in one direction.

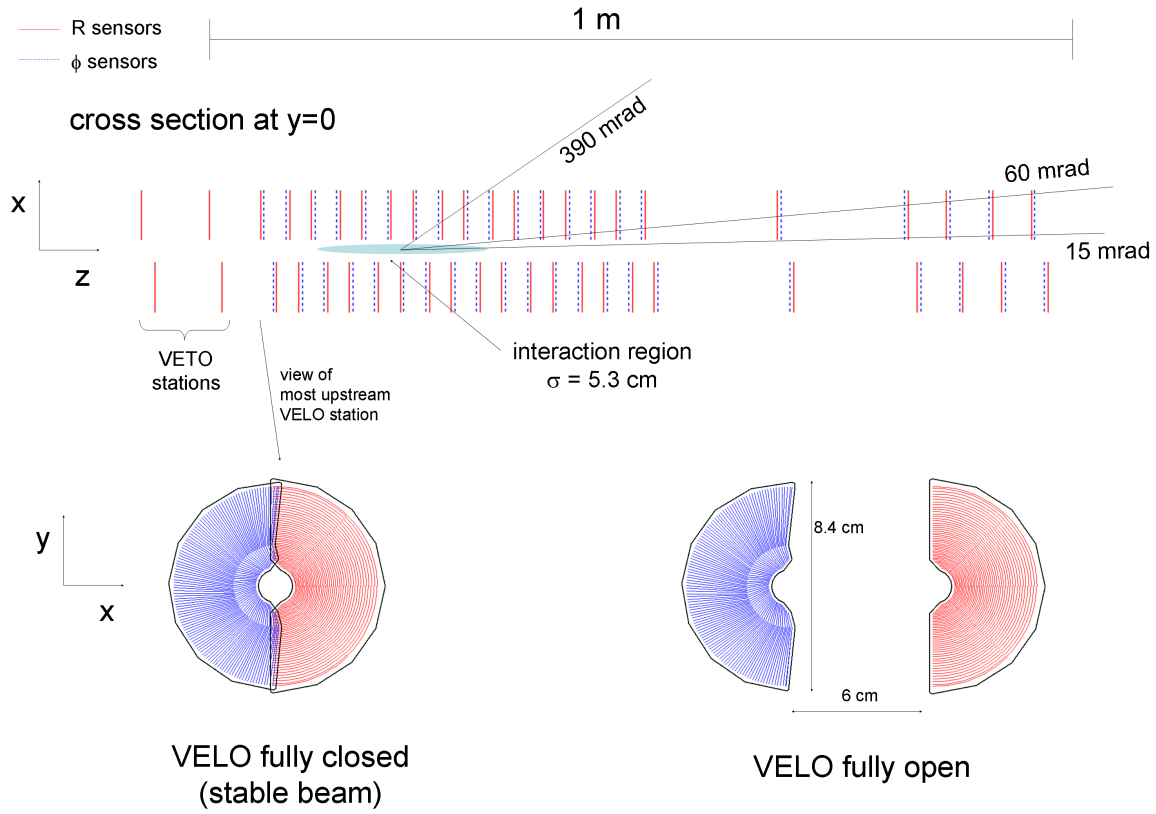

Figure 5: Schematic view of the Vertex Locator. At the top the overall arrangement of the stations along the z-axis. At the bottom the two halves of one station. The figure is taken from Ref. [17].

component of the LHCb tracking system is the VErtex LOcator (VELO), which is placed as close as 8 mm to the collision point. The detector consists of 21 stations in a row in z-direction with two different types of silicon-strip sensors, one is used to measure the radial component of a particle and one the azimuthal component. The z component is measured by the position of the stations, see figure 5. The VELO is used to precisely reconstruct the decay of heavy-flavoured hadrons. The typical b- and c-hadrons lifetime of approximately 1 ps and their high boost allow a travel distance of about 1 cm before decaying. Therefore, it is possible to precisely measure the position of the decay vertices and to determine the decay-time with help of these well displaced vertices.

The main purpose of the Track Turiencies (TT) is to allow the reconstruction of low-momentum particles ($< 2\,\mathrm{GeV}/c$), which are bent by the magnetic field out of the acceptance of the tracking stations downstream, and long-lived particles, which decay outside of the VELO. The TT is a micro-strip detector consisting of four silicon sensor

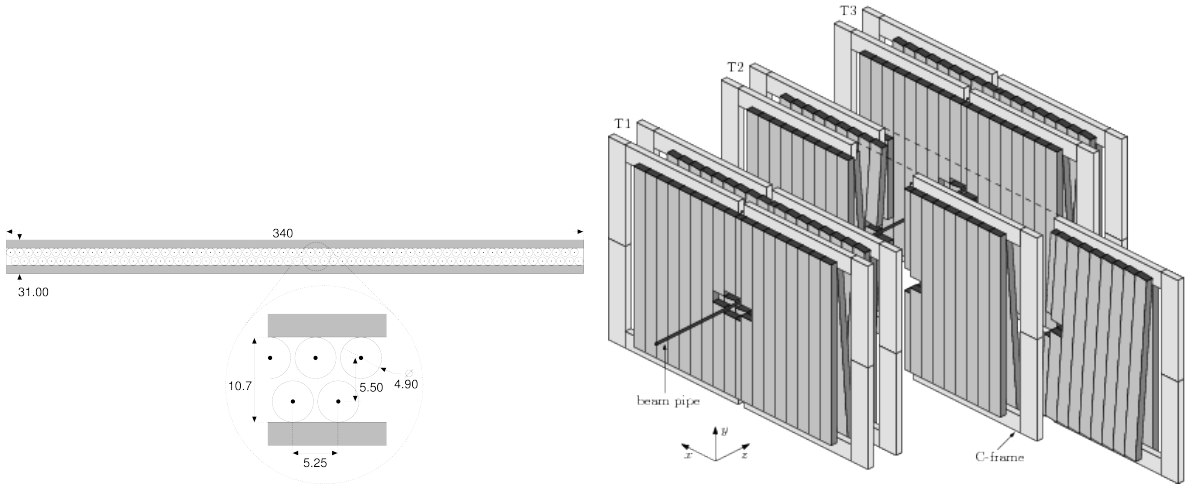

Figure 6: Schematic view of the cross section of one double layer on the left with the straw tubes and on the right the overall arrangement of the different tracking stations. The figure is taken from Ref. [18].

layers, which are grouped in two stations. These stations have a distance of 30 cm to each other along the beam axis. The first and last layer are aligned vertically in y-direction. The middle layers are rotated by an angle of $+5°$ and $-5°$ to provide the necessary resolution in y-direction. A dipole magnet, placed between the TT and the tracking stations, with an integrated strength of above 4 Tm is used to measure the momentum. The main component of the magnetic field is along the y-axis therefore, the (x, z)-plane is in good approximation the bending plane. A special feature of LHCb is the ability to change the polarity of the magnet. This allows that any charge asymmetry introduced by the detector, to a large extend, is canceled out, if the collected data samples with the two different polarities (*MagUp* and *MagDown*) have approximately the same size. Therefore, the magnet polarity is reversed approximatively every two weeks. Lastly, after the magnet, the three tracking stations (T1, T2, T3) are located, which are used to measure the trajectory of high momentum particles and the decay vertices of lighter particles, which do not decay inside the VELO and TT. The three tracking stations consist overall of 24 layers, whereas each station is split into four double layers. Each layer consists of two rows of straw tubes, which are filled with gas. In Figure 6 the cross section of a single layer and the arrangement of all layers within the detector is shown. This sub-detector is constructed to cover a large area $6 \times 5\,\mathrm{m}^2$.

3.2.2 Particle identification system

To study processes at the LHCb it is necessary to identify particles with a high reliability. Particles are identified by the particle identification system of the LHCb. The particle identification system consists out of the main components a Cherenkov detector system, the calorimeter system, and the muon stations. The first Ring Imaging CHerenkov detector (RICH 1) is located directly behind the VELO. The second RICH detector (RICH 2) is located between the tracking stations and the calorimeter system. The two RICH detectors work with help of Cherenkov radiation. If a charged particle crosses a medium, with refractive index $n > 1$, with a velocity, v, larger than the local phase velocity of light Cherenkov light is emitted. The photons are emitted under the Cherenkov angle, θ, with respect to the particle momentum direction.

$$\theta = \frac{c}{nv} \tag{3.1}$$

This way it is possible to measure the velocity of a particle. With the measured momentum and trajectory of a particle different mass hypotheses for the particle can be tested. RICH 1 is used for particles with low momentum 1-60GeV/c, whereas RICH 2 is used for particles with higher momentum 15-100GeV/c.

The Scintillating Pad Detector (SPD) is used to separate photons and electrons, as only the latter is detected by the SPD. Directly behind the SPD is the PreShower detector (PS) located which measures the energy deposited in the lead. Afterwards the energy deposit, for electrons and photons, is measured in the Electromagnetic CALorimeter (ECAL). The ECAL consists out of 2 mm thick lead and 4 mm thick scintillating material installed alternately. Downstream of the ECAL the Hadronic CALorimeter (HCAL) is located which is used to measure the energy of hadrons, and identify said hadrons. The HCAL is in principal similarly built than the ECAL only with larger cells consisting of iron in between the scintillators. When a particle deposits parts of its energy or is stopped in the absorber material, charged particles and photons are emitted. These particles are then converted to photons in the scintillating material, which are then detected by photomultipliers. The number of detected photons is proportional to the energy of the original particle. The complete arrangement of the calorimeter system is shown in figure 7 on the left.

Outermost, as the muons produced at LHCb penetrate all the inner detector subsystems, including calorimeters, the muon stations (M1-M5) are located. The muon stations are separated by 80 cm thick iron plates. This way it is ensured that only muons can reach the last station. Therefore the muon stations play an important role in the trigger. The arrangement of the muon station in the detector is illustrated in figure 7 on the right. As

a summary the RICH 1, RICH 2 and HCAL are used to identify charged hadrons, SPD and ECAL electrons and photons and lastly the muon system muons.

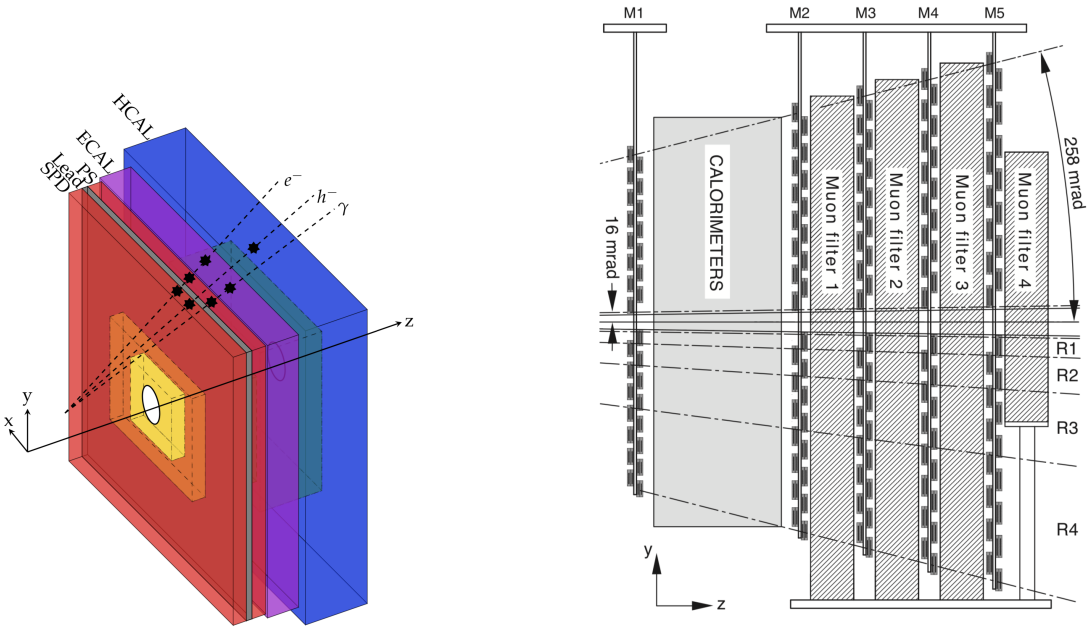

Figure 7: Schematic view of the calorimeter system on the left and on the right the location of the muon stations including the position of the calorimeter system. The figures are taken from Ref. [19, 20].

3.2.3 Trigger/Turboline

To access the large amount of data the LHCb trigger system is used which discards most of randomly detected particles and events which are not of interest before sending the data to mass storage. The trigger is build up in three levels:

- Level-0 (`L0`): The Level-0 trigger is implemented on hardware level. Informations obtained directly from the detector are used to select decay candidates, *e.g.* a hit in the last muon station. The reason for this is the fixed latency of the trigger of 4 μs in which it is not possible to perform complicated elaboration.

- High Level Trigger 1 (`Hlt1`): The first software based trigger mainly is used to trigger for loose topological requirements. At this trigger level the event is only partially reconstructed.

- High Level Trigger 2 (`Hlt2`): The second level software trigger is used to trigger for stronger topological conditions, for specific final states, than the `Hlt1`. This is

possible because the decay chain is already fully reconstructed during the trigger process.

The turbo stream saves decays which are fully reconstructed in HLT2. All other data, of the event, is discarded to save storage. The advantage of the turbo stream is that no offline reconstruction is needed, as the online reconstruction already used the most updated calibrations. Therefore, it is only necessary to store the relevant data for further processing, which means that less memory is required. For Run 2 data both data streams are available for analysis; in the future, the turbo stream is foreseen to become the standard.

4 Reconstructing and selecting charm decays at LHCb

A_Γ is measured from data taken in proton-proton collision during the years 2016-2018, at a center-of-mass energy of 13 TeV which correspond to an integrated luminosity of 5,4 fb^{-1}. For this analysis the already preselected data from the measurement presented in Ref. [2] is used. In this chapter is discussed how the data is reconstructed and additionally introduced selection steps are explained.

In the following $D^0 \to \pi^+\pi^-$ and $D^0 \to K^+K^-$ decays are referred to as the signal modes, while $D^0 \to K^-\pi^+$ decays are denoted as control channel.

4.1 Reconstruction and background identification

Two main categories of background contributions can imitate the signal decays. Physical background and randomly associated tracks, which accidentally pass the selection requirements. A mixture of these two categories is also possible. Physical background is where either parts of the decay chain are not correctly reconstructed or particles are misidentified. Processes leading to a wrong flavour tag of the D^0 meson are discussed in the systematic studies subsection 6.3.

- *Partially reconstructed multi-body decays.* Decays which are not completely reconstructed can mimic the signal topology. But these decays are not expected to peak in the mass range of the D^0 candidate and can therefore be estimated statistically.

- *Muon coming from intermediate particles.* Muons that arise from intermediate particles, *i.e.* muons which do not originate directly from the B vertex, do directly bias the decay-time, because for the reconstruction of the decay-time the D^0 decay vertex and the B decay vertex, which is reconstructed directly from the muon, are used. However, the fraction of this background source is reduced to a negligible level after the selection, due to the tight constraints imposed from the decay topology.

- *Combinatorial background.* These candidates are entirely made of randomly associated tracks. Even with tight constraints on the decay topology their fraction cannot be reduced to a negligible level.

- *Misidentified particles.* These are candidates which fulfil the same topology constraints as the signal decays, but the decays consist of particles which are

wrongly identified. The largest fraction of wrongly identified particles comes from $D^0 \to K^-\pi^+$ decays where the wrong mass hypothesis is applied to the pion (kaon) which then are wrongly identified as $D^0 \to K^+K^-$ ($D^0 \to \pi^+\pi^-$). Another source for misidentified particles are final state particles coming from *e.g.* $B^0 \to J/\psi K\pi$ decays. The fraction of this background sources are reduced to a negligible level after the selection.

Normally, at LHCb, the event reconstruction of the collected data is done centrally after the trigger lines are applied. But for this analysis the so called turbo line is used, therefore the already at `Hlt2` level reconstructed events are used.

The event reconstruction is done in a bottom-up approach, meaning that first the stable final state particles are combined to then reconstruct the intermediate particles. Candidates are identified by combining two oppositely charged tracks which are consistent with coming from a common secondary vertex to form a D^0 candidate. As next step a muon, which is coming from a common secondary vertex with the D^0 candidate to form a B candidate, is chosen. An illustration of the decay topology can be found in figure 8. The additionally produced neutrinos are not detected by the detector.

To ensure a certain quality of the reconstructed events and discard wrongly associated $D^0 \to h^+h^-$ decay candidates, certain selection criteria are applied in the trigger. Recon-

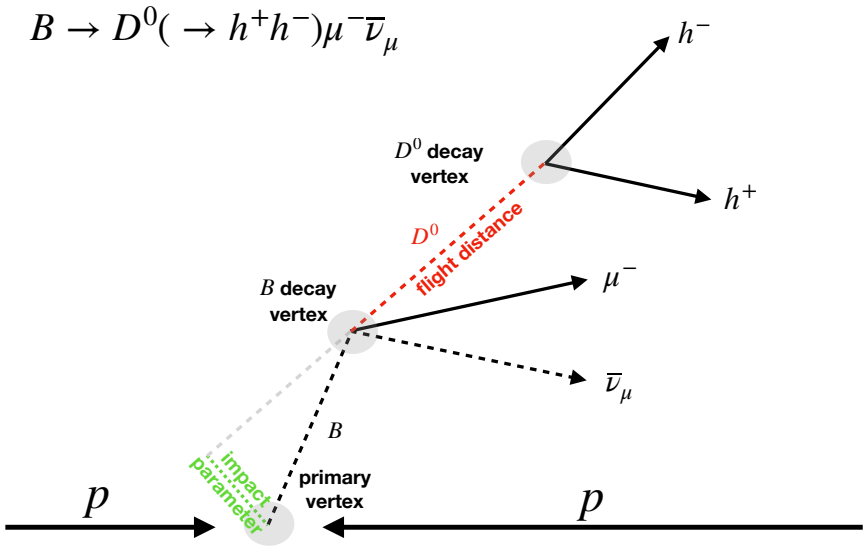

Figure 8: Schematic view of the decay topology in the y-z plane of $D^0 \to h^+h^-$ decays. The impact parameter, with respect to the primary vertex, and the flight distance for the D^0 meson is indicated. Both are typically of the size of a few millimetres. The relative scale is arbitrary and not realistic.

structed artefacts may lead to ghost tracks if unrelated hits are combined. Information from the tracking system is combined to compute a per track ghost probability. Events with a large ghost probability are discarded. Furthermore, as the signal pion and kaons come from an secondary D^0 vertex, a requirement on the χ^2(IP) is chosen, as well as a requirement on the minimum (transverse) momentum of (0.2)2 GeV/c to further suppress combinatorial background. χ^2(IP) is a quantity which expresses how well the impact parameter, of the corresponding particle, is compatible with the primary vertex. This quantity is expected for the D^0 daughters to be large. The impact parameter (IP) (usually a few millimetre) is the distance between the primary vertex and the minimal distance of the reconstructed track, as illustrated in figure 8 for D^0. Particle identification (PID) requirements are needed to reduce the background from wrongly identified particles. For particle identification a observable called log-likelihood difference (DLL) is used. For each charged particle, likelihood functions for several mass hypotheses are constructed using information from the RICH and calorimeter systems. To then test different mass hypotheses the difference between logarithms of the likelihoods for two different hypothesis is computed, here the difference between the K and π hypothesis $\mathrm{DLL}_{K\pi}$. This difference allows to separate kaons from pions because for pions the average $\mathrm{DLL}_{K\pi}$ value in general is smaller than zero and for kaons larger than zero.

The event reconstruction is done by the `DecayTreeFitter` (DTF) package [21]. To further reduce the background the reconstructed invariant mass of the D^0 meson, given by

$$m(D^0) = \sqrt{E^2(h^+h^-) - p^2(h^+h^-)} \tag{4.1}$$

where h stands for the final state pion or kaon and

$$E(h^+h^-) = E(h^+) + E(h^-), \tag{4.2}$$

$$\vec{p}(h^+h^-) = \vec{p}(h^+) + \vec{p}(h^-), \tag{4.3}$$

is checked to be near the expected mass of the D^0 (1864 MeV/c^2). Wrongly and partially reconstructed tracks, as not all particles are correctly identified, lead to a wrong mass hypothesis. The reconstructed mass of the D^0 is limited to the range $m(D^0) \in [1775, 1955]$ MeV/c^2. Additionally, the D^0 decay vertex should be reconstructed well enough, which is quantified by the χ^2/ndf value of the DTF. χ^2/ndf is required to be small. Furthermore, as the D^0 is expected to fly a certain distance, in the detector, it is required that the B and D^0 decay vertex can be well separated. With help of the flight distance L, reconstructed from the decay vertex positions, measured by the VELO, it is possible to reconstruct the decay-time t_D of the D-meson:

$$t_{D^0} = \frac{\mathrm{L} \cdot m(D^0)}{p(D^0)} \tag{4.4}$$

where $p(D^0)$ is the measured momentum of the D^0. A schematic plot of the $B \to D(\to h^+h^-)\mu\nu$ vertex with indicated flight distance for the D^0 meson can be seen in figure 8.

For the muon candidates the same kinematic conditions are demanded as for the pion and kaon candidates. Except, as the muon is lighter than the two mesons, it is expected that the muon has a higher momentum. To further suppress combinatorial background a minimum (transverse) momentum of (1)3 GeV/c is required. The PID requirements are also different for the muon candidate.

The B meson is expected to originate form the primary vertex. To reduce wrongly reconstructed $B \to D^0\mu\nu$ decays it is required that the distance of closest approach of the reconstructed B track and the primary vertex are compatible with each other. Additionally, the B decay vertex should be well reconstructed. Despite the missing momentum of the neutrino in $B \to D^0\mu\nu$ decays, the reconstructed B meson momentum as obtained from the vectorial sum of the charged final state tracks is expected to be fairly aligned with the reconstructed flight distance. A requirement of the angle between the reconstructed momentum and flight distance of the B candidate efficiently reduces the background from partially reconstructed multi-body decays. The angle is expected to be small if only a neutrino is missing in the reconstruction. Constraints on the reconstructed and corrected mass are set to further reduce the background from partially and wrongly reconstructed tracks. The corrected mass is defined as

$$m_{corr}(B) \equiv \sqrt{m^2(D^0\mu) + p_\perp^2(D^0\mu)} + p_\perp(D^0\mu) \tag{4.5}$$

and partially corrects for the unreconstructed particles in the decay of the B meson. Here, $p_\perp(D^0\mu)$ is the momentum of the $D^0\mu$ system transverse to the B flight direction, the momentum is used to partially account for the missing neutrino. An illustration of the transverse momentum can be found in figure 9.

4.2 Offline Selection

The offline selection and optimisation is inherited from the analysis presented in Ref. [22]. For this thesis the finally selected tuples are directly used, a more detailed and technical description can be found in the corresponding thesis [2]. For this analysis only data collected in Run 2 in the years 2016, 2017 and 2018 is analysed. Data for 2015 is excluded because of the missing turbo-line and as it would not significantly increase the statistical precision.

To avoid background from wrongly reconstructed decays the reconstructed muon is required to also be detected as a muon in the muon chamber, which is not necessarily the case. Additional is also asked that the reconstructed muon or B track were also already

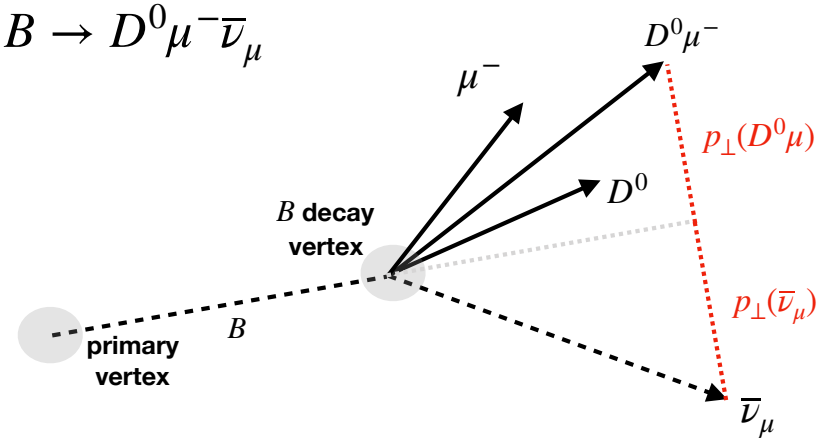

Figure 9: Schematic view of the decay topology in the y-z plane of $B \to D^0\mu^-\overline{\nu}_\mu$ decays. The transverse momentum for the $D^0\mu^-$ system with respect to the B flight direction is indicated. The relative scale is arbitrary and not realistic.

identified by the `HLT1`, before the full reconstruction. This reduces further that randomly associated tracks and particles, in combination with a wrongly reconstructed decay chain, fulfil the following topological selection and accidentally are treated as signal.

The particles are boosted in z-direction. Given momentum conservation, it is very likely that if the D decays upstream of the B decay vertex the D daughters fly upstream and leave the detector. Therefore, the chance is high that if the decay chain is fully reconstructed within the detector, but the D decays upstream of the B decay vertex, the reconstruction is wrong. To avoid this a cut which ensures that the D decays downstream of the parent B vertex ($vtx_z(D^0) - vtx_z(B)$) is applied. Additionally, a limit on the decay-time is set for $t/\tau_{D^0} > 0$ as this region is dominated by background. In principle, negative decay-times are possible due to resolution effects. The limits on the visible B mass ($m(B)$) and on the corrected mass ($m_{corr}(B)$) are tightened to reduce the background further. To ensure that the decay is correctly reconstructed a minimum quality on the reconstruction of the D^0 and B is expected (DTF $\chi^2/\text{ndf}(B) \in [0, 9.5]$,DTF $\chi^2/\text{ndf}(D^0) \in [0, 6.5]$). As the particle identification requirements made in the reconstruction on the D^0 daughters is very loose also this cut is tightened.

For the charge conjugation symmetrical final states $D^0 \to \pi^+\pi^-$ and $D^0 \to K^+K^-$ no time-dependent detection asymmetries is expected. However, for the control channel this is not the case, due to the fact that the negative charged kaon, K^-, differently interacts with the detector material than the positively charged kaon, K^+. This is especially true for low transfers momentum $p_T(K)$ (low energy) of the kaon, whereas for higher transverse momentum (higher energy) this effect is negligible. In figure 10 the influence of the raw

asymmetry against $p_T(K)$ is shown. As the flight distance of the D^0 candidate and $p_T(K)$ are correlated, the region $p_T(K) < 800MeV$ for $D^0 \to K^-\pi^+$ is excluded.

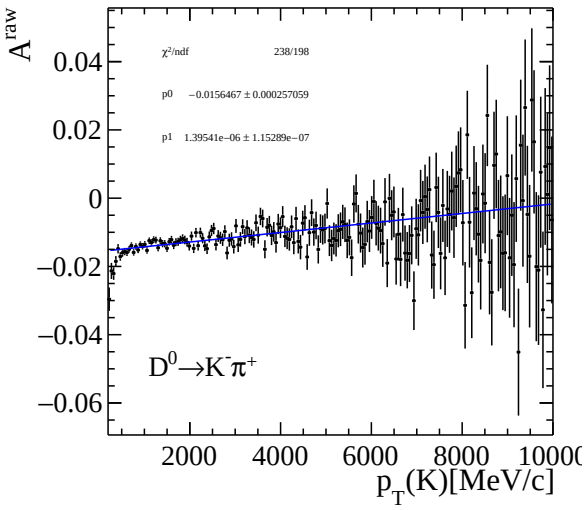

Figure 10: Raw asymmetry $\mathcal{A}_{\text{raw}}$ in bins of kaon p_T with linear fit overlaid for $D^0 \to K^-\pi^+$.

Wrongly identified particles coming from $D^0 \to K^-\pi^+$ decays are expected to peak about $70\,\text{MeV}/c^2$ to the left (right) in the D^0 mass for $D^0 \to \pi^+\pi^-$ ($D^0 \to K^+K^-$) decays[3]. To reduce the background from these decays the size of the mass window is limited to $[1820, 1939]\,\text{MeV}/c^2$ for $D^0 \to \pi^+\pi^-$ decays and $[1825, 1915]\,\text{MeV}/c^2$ for $D^0 \to \pi^+\pi^-$ decays. The fraction of misidentified particles from $D^0 \to K^-\pi^+$ decays by this limit is reduced to a negligible level, $\mathcal{O}(10^{-4})$ and $\mathcal{O}(10^{-5})$, respectively for the pion and kaon sample [23]). As summary the set of all offline preselection cuts is shown in table 2.

Lastly two kinematical cuts are applied to the data sample. First, one to reduce the background from misidentified B decays to final state decays involving a charmonium resonance (J/ψ or $\psi(2S)$). These decays are vetoed by a cut on the invariant mass of the combination of the muon candidate with the oppositely charged D^0 daughter particle under the dimuon-mass hypothesis, $55\,\text{MeV}/c^2 > m_{\mu^+\mu^-}(h^\pm\mu^\mp) - m_{J/\psi} > 45\,\text{MeV}/c^2$ with

$$m_{\mu^+\mu^-}(h^\pm\mu^\mp) = \sqrt{E^2_{\mu^+\mu^-}(h^\pm\mu^\mp) - p^2(h^\pm\mu^\mp)} \tag{4.6}$$

where

[3]If a $D^0 \to K^-\pi^+$ candidate is wrongly identified as $D^0 \to \pi^+\pi^-$ candidate the pion mass hypothesis is assigned to the kaon in the event reconstruction and, therefore, leads to a smaller reconstructed invariant D^0 mass. The same happens for $D^0 \to K^+K^-$ only that the heavier kaon mass is assigned to the wrongly identified pion and, therefore, leads to a heavier reconstructed invariant D^0 mass.

Variable	$D^0 \to \pi^+\pi^-$	$D^0 \to K^+K^-$	$D^0 \to K^-\pi^+$
$m(D)$	$[1820, 1939]\,\mathrm{MeV}/c^2$	$[1825, 1915]\,\mathrm{MeV}/c^2$	$[1780, 1940]\,\mathrm{MeV}/c^2$
t/τ_{D^0}	$[0, 10]$	$[0, 10]$	$[0, 10]$
DTF $\chi^2/\mathrm{ndf}(B)$	$[0, 9.5]$	$[0, 9.5]$	$[0, 9.5]$
DTF $\chi^2/\mathrm{ndf}(D^0)$	$[0, 6.5]$	$[0, 6.5]$	$[0, 6.5]$
$m(B)$	$[2.5, 5]\,\mathrm{GeV}/c^2$	$[2.5, 5]\,\mathrm{GeV}/c^2$	$[2.5, 5]\,\mathrm{GeV}/c^2$
$m_{corr}(B)$	$< 6\,\mathrm{GeV}/c^2$	$< 6\,\mathrm{GeV}/c^2$	$< 6\,\mathrm{GeV}/c^2$
$vtx_z(D^0) - vtx_z(B)$	$> 0\,\mathrm{mm}$	$> 0\,\mathrm{mm}$	$> 0\,\mathrm{mm}$
$\mathrm{DLL}_{K\pi}$ of D^0 daughters	< -2	> 5	$> 5(K^-)$, $< -2(\pi^+)$
$p_\mathrm{T}(K)$			$> 800\,\mathrm{MeV}/c$

Table 2: Additional preselection selection cuts applied on the output of the turbo line.

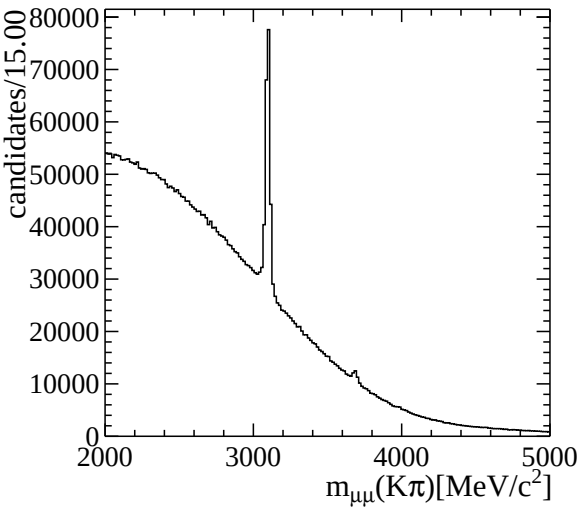

Figure 11: Distributions of the invariant mass of the muon-hadron combination with opposite charge under the dimuon mass hypothesis, produced with a subsample of $D^0 \to K^-\pi^+$ decays for illustration purposes.

$$E_{\mu^+\mu^-}(h^\pm\mu^\mp) = E_\mu(h^\pm) + E_\mu(\mu^\mp), \tag{4.7}$$

$$E_\mu(h^\pm) = \sqrt{m_\mu^2 + p^2(h^\pm)}, \tag{4.8}$$

$$p(h^\pm\mu^\mp) = p(h^\pm) + p(\mu^\mp) \tag{4.9}$$

$m_{J/\psi}$ is the J/ψ mass and m_μ the muon mass taken from Ref. [24]. These decays are only vetoed if the hadron is identified as muon. See figure 11 for a plot of the invariant mass distribution of the muon-hadron candidates with dimoun-mass hypothesis before the cut.

Secondly, regions in the phase space of the tag muon are identified to have large instrumental asymmetries, where muons of one charge are either bent out of the detector acceptance or deflected into the LHC beam pipe. To identify these kinematic regions the raw asymmetry is plotted as a function of p_x and p_z, as shown in figure 12. Muons with low forward momentum p_z and corresponding high momentum in $x-$direction are bend out of the detector. Whereas, muons in the momentum region limited by the black horizontal lines are deflected into the LHC beam pipe. To keep the detector asymmetry A_{det} low, as the muons are used to identify the flavour of the D meson which would directly bias the asymmetry, these regions are vetoed, using the following requirements:

$$\begin{aligned} &|p_x| < 0.315 \cdot p_z - 1032.5\,\text{MeV}/c \\ &|p_x| > 1000\,\text{MeV}/c \quad \text{OR} \quad |p_x| < 700\,\text{MeV}/c. \end{aligned} \tag{4.10}$$

In total three additional cuts to the analysis presented in Ref. [23] are applied the limits on the mass $m(D)$ and decay-time t/τ_{D^0} and the cut for small $p_T(K)$ on $D^0 \to K^-\pi^+$ decays.

As the background level is not reduced to a sufficient level after the trigger and preselection, a *Boosted Decision Tree* (BDT) has been trained to isolate the signal candidates from background made of randomly associated tracks [2]. The training has been performed separately for each signal channel ($D^0 \to \pi^-\pi^+$ and $D^0 \to K^-K^+$) and year of data taking using D^0 candidates in the sideband defined as $m(D^0) > 1900\,\text{MeV}/c^2$ ($D^0 \to \pi^-\pi^+$) and $1900\,\text{MeV}/c^2 < m(D^0) < 1920\,\text{MeV}/c^2$ ($D^0 \to K^-K^+$) as background candidates for the training. $D^0 \to K^-\pi^+$ candidates around the signal peak ($1844\,\text{MeV}/c^2 < m(D^0) < 1884\,\text{MeV}/c^2$) are used as signal proxy because of the negligible amount of background. In figure 13 the used signal and background regions are illustrated. To achieve an unbiased evaluation of the performance of the BDT, signal and background samples have been split in two halves, where one half is used for testing and performance checks and the other for training.

The BDT is using a number of variables which are expected to give a good separation between signal and background. The signal candidates are expected to be better described by the DTF than the background candidates. Also the D^0 is expected to fly a certain distance from the B decay vertex. Therefore, the impact parameters for the final state particles $D^0 \to \pi^-\pi^+$ and $D^0 \to K^-K^+$ are expected to be within a certain range in contrast to the background events. To ensure a certain quality of the reconstruction and also because of the lifetime the D^0 is expected to fly a significant distance from

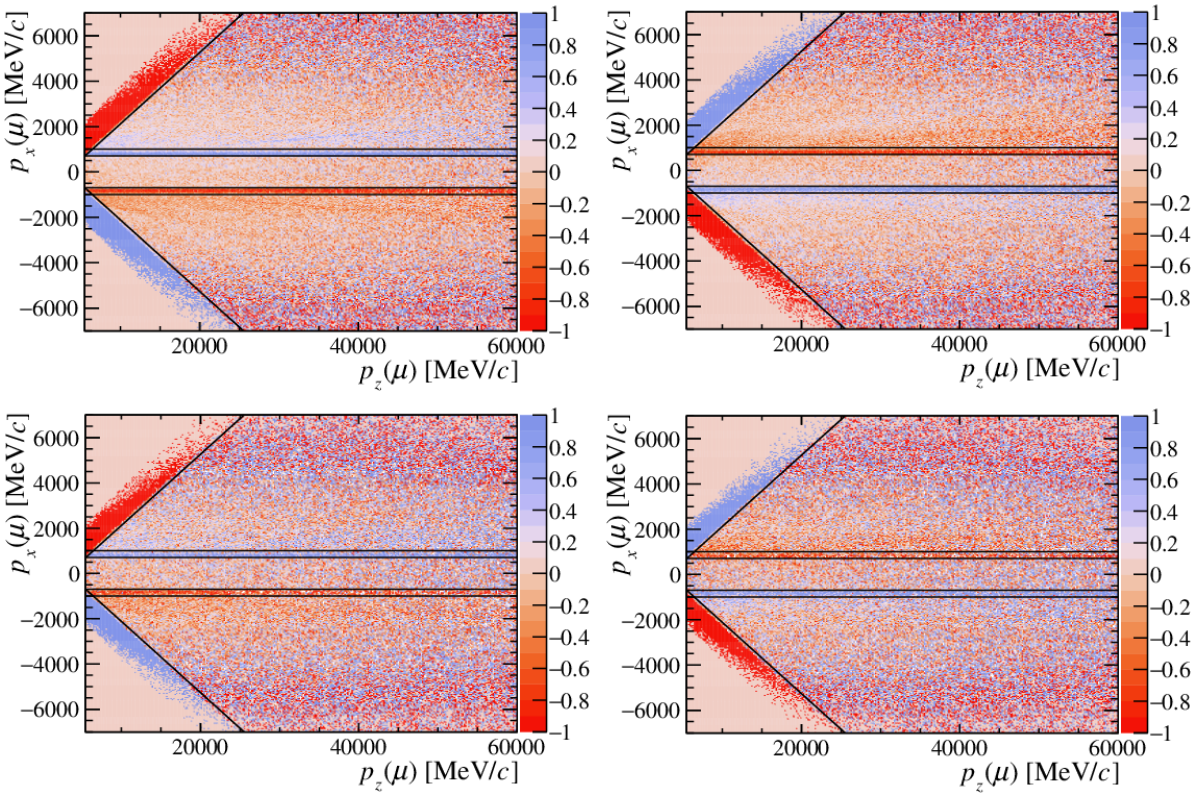

Figure 12: Raw asymmetry distributions as a function of p_x and p_z in [%] for $D^0 \to K^-K^+$ (top) and $D^0 \to \pi^-\pi^+$ (bottom) decays with the magnet polarity pointing up (left) and down (right). The black lines show the boundaries of the large raw asymmetry regions which are excluded by the fiducial cuts. The 2016 *MagDown* data sample is shown as an example. Similar distributions are obtained for 2017 and 2018 data sample. Figure taken from Ref. [2]

its production vertex, this cannot be guaranteed for background events. Because of momentum conservation final state particles arising from the D^0 are expected to have a higher transverse momentum in average than final state particles directly produced at the primary vertex. In addition to the already applied cuts on the visible B mass and corrected B mass, both variables are also used to train the BDT as wrongly reconstructed events are not expected to have the same distinct features around the nominal B mass. The background may peak around the nominal B mass but the peak of the signal candidates is expected to be narrower and more distinct. Lastly the BDT is also trained on the number of hits in the SPD. In the following all BDT input variables are listed:

- the DTF χ^2 per degree of freedom for the B and D^0 candidates, $\chi^2/\mathrm{ndf}(B)$ and $\chi^2/\mathrm{ndf}(D^0)$
- the logarithm of the flight distance (FD) significance of the D^0 candidate $\log\{\chi^2\,[\mathrm{FD}(D^0)]\}$

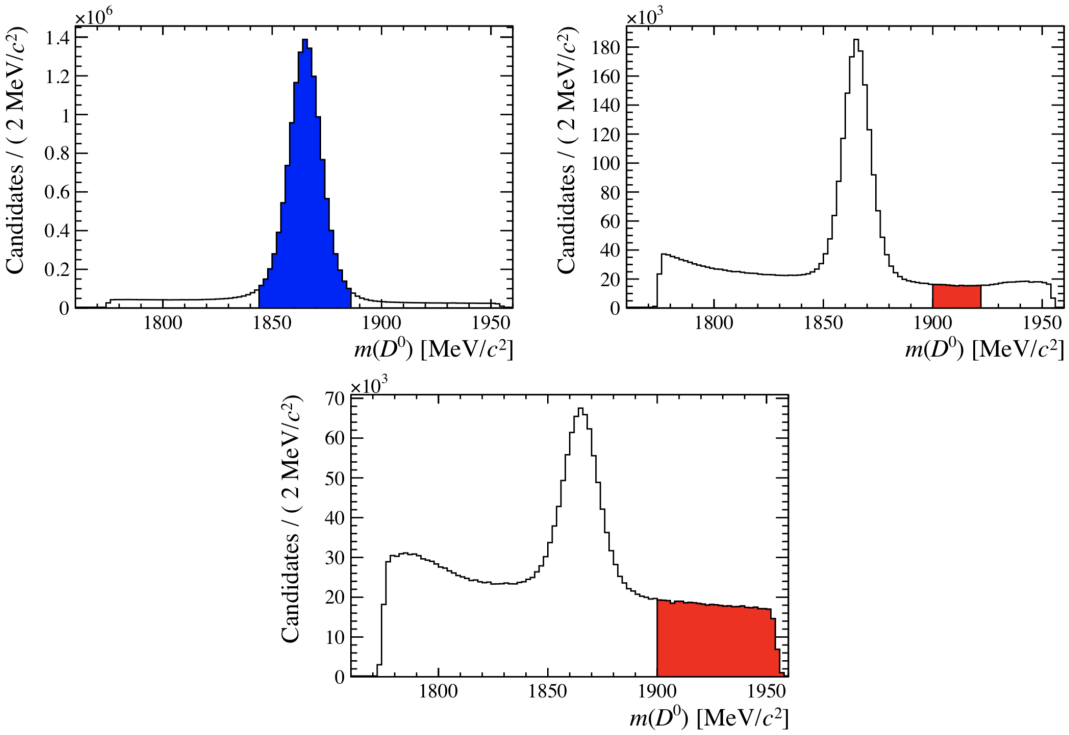

Figure 13: The m(D^0) distribution for $D^0 \to K^-\pi^+$ (top left),$D^0 \to K^+K^-$ (top right) and $D^0 \to \pi^+\pi^-$ (bottom) samples taken from 2016 with *MagDown* polarity. The signal region is highlighted in blue and the background regions in red. Figure taken from Ref. [2]

- the logarithm of the impact parameter (IP) significances of the D^0 daughter tracks $\log\{\chi^2\,[\mathrm{IP}(h^+)]\}$ and $\log\{\chi^2\,[\mathrm{IP}(h^-)]\}$
- the transverse momenta of the D^0 daughter tracks, $p_\mathrm{T}(h^+)$ and $p_\mathrm{T}(h^-)$,
- the $(vtx_z(D^0) - vtx_z(B))/(\sqrt{\sigma^2(vtx_z(D^0)) + \sigma^2(vtx_z(B))})$
- the visible and corrected masses of the B candidate $m(B)$ and $m_{corr}(B)$
- number of Scintillating Pad Detector (SPD) hits

The BDT assigns to each candidate a numerical factor between -1 and 1 depending on how likely the candidate is background or signal, respectively. The final BDT output distributions comparing the numerical factors between test and training sample for $D^0 \to \pi^-\pi^+$ and $D^0 \to K^-K^+$ can be found in figure 14. The optimal BDT cut to separate background from signal is chosen by maximising the figure of merit $S/\sqrt{S+B}$ for preselected candidates in a mass range corresponding to approximately three sigma of mass resolution around the nominal D^0 mass, S and B denote the signal and background yields in this range, respectively. The optimal cuts are `BDT>0.0` for $D^0 \to K^+K^-$ and

`BDT>-0.1` for $D^0 \to \pi^+\pi^-$. If an event contains more than one B candidate after the full selection, one is chosen at random. The fraction of candidates removed by this requirement is 0.4%. These BDT cuts lead to a 90% (75%) signal efficiency and rejects 55% (85%) of background candidates for $D^0 \to K^-K^+$ ($D^0 \to \pi^-\pi^+$).

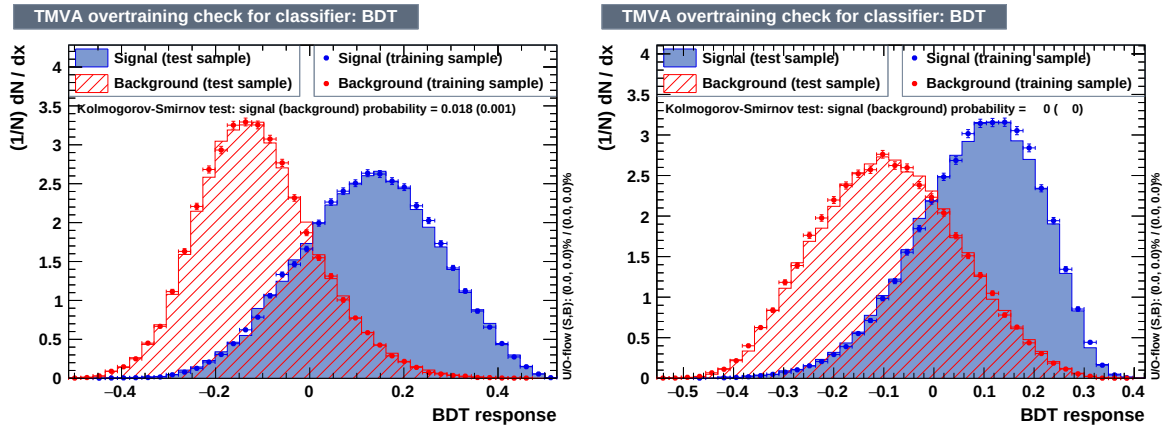

Figure 14: Distributions of the BDT response for $D^0 \to \pi^-\pi^+$ (left) and $D^0 \to K^-K^+$ (right) decays for the signal and background. The 2016 data sample is shown as an example. Taken from Ref. [2].

The D^0 mass spectra after the selection for $D^0 \to K^-\pi^+$, $D^0 \to K^+K^-$ and $D^0 \to \pi^+\pi^-$ decays can be seen in figure 15, where in total approximately 77M, 9M and 3M signal candidates with high purities (S/B) of roughly 5 ($D^0 \to K^+K^-$, $D^0 \to \pi^+\pi^-$) and 28 ($D^0 \to K^-\pi^+$) are selected; measured in a signal window of approximately $3\,\sigma$ of the mass resolution around the nominal D^0 mass peak position.

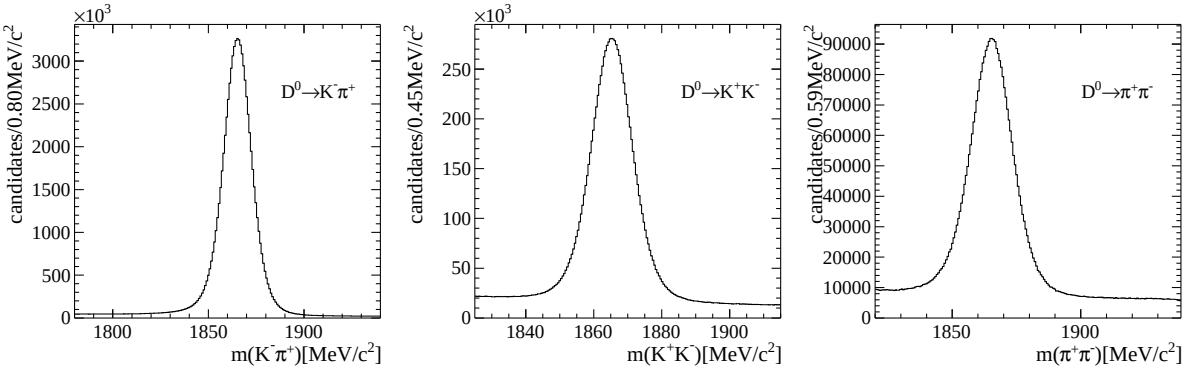

Figure 15: D^0 mass distribution of finally selected $D^0 \to K^-\pi^+$ (left), $D^0 \to K^+K^-$ (middle) and $D^0 \to \pi^+\pi^-$ (right).

5 Determination of A_Γ

In this chapter the measurement of A_Γ is explained.

At first a decay-time integrated fit to the invariant D^0 mass distribution of the selected data sample is performed. Afterwards the data sample is split in 20 approximately equally populated decay-time bins. The results of the integrated mass fit is used to simplify the fit model and perform a simplified fit to the data in each decay-time bin. From the resulting time-dependent asymmetry A_Γ is determined.

5.1 Mass fit model

After the full selection the data sample composes mainly of an unknown mixture of the following three components:

- signal $D^0 \to \pi^+\pi^-$ or $D^0 \to K^+K^-$ (or control $D^0 \to K^-\pi^+$) decays
- combinatorial background
- partially reconstructed background

The signal is expected to peak around the nominal D^0 mass, whereas the combinatorial and partially reconstructed backgrounds do not form a peak, as they do not originate from true D^0 candidates. Due to this fact it is possible to separate background and signal candidates statistically. The signal contribution is separated from the background by performing a fit to the invariant D^0 mass distribution $m(D^0)$. All fits are binned χ^2 fits. The χ^2 fit technique is a method of parameter estimation, given a statistical model and a set of measured observables. In Ref. [25] a detailed description can be found.

Given the finite resolution of the LHCb detector the shape of the signal peak is dominated by detector effects. These detector effects, due to the central limit theorem, are best described by a normal distribution. Additionally, a tail on the signal peak for the lower mass spectrum is observed, due to candidates with missing energy. One source for these missing energies could be Bremsstrahlung from the pion visible in the control sample due to the high statistic. To describe the slightly asymmetric behaviour a Johnson's S_U distribution is used. The Johnson's S_U [26] is a four-parametric function resulting from a variable transformation of a normal distribution, to allow for asymmetric tails, and has the following form:

$$\mathcal{J}(m|\mu_J, \sigma_J, \nu, \tau) = \frac{1}{\mathcal{N}_J} \frac{e^{-\frac{1}{2}r^2}}{c \cdot \sigma_J \cdot \tau \cdot \sqrt{z^2+1}}, \tag{5.1}$$

The following parametrisation is used to directly access the mean μ_J and the standard deviation σ_J of the Johnson's S_U PDF:

$$r = -\nu + \frac{\operatorname{asinh}(z)}{\tau}, \tag{5.2}$$

$$z = \frac{m - (\mu_J + c \cdot \sigma_J \cdot \sqrt{w}\sinh(\omega))}{c \cdot \sigma_J}, \tag{5.3}$$

$$c = \frac{w-1}{2\sqrt{w \cdot \cosh(2\omega) + 1}}, \tag{5.4}$$

$$w = e^{\tau^2}, \tag{5.5}$$

$$\omega = -\nu \cdot \tau. \tag{5.6}$$

ν and τ are the skewness and kurtosis, respectively, which describe the asymmetric tail. $\mathcal{N}_J$ is a normalisation factor. The sum of a Johnson's S_U $\mathcal{J}$ and a normal distribution $\mathcal{G}$ with an appropriate fraction f_1, also obtained by the fit, are used to describe the signal.

The background is dominated by combinatorial background which is randomly distributed over the complete mass range. Therefore, and to also account for the small fraction of partially reconstructed background, a normalised linear function is used to describe the background, given by:

$$\mathcal{T}(m|c_1) = \frac{1}{\mathcal{N}_L}(1 + c_1 m), \tag{5.7}$$

where $\mathcal{N}_L$ is a proper normalisation and c_1 the slope.

To directly obtain the statistical uncertainty for the raw asymmetry, the asymmetry is directly estimated by the fit. This is done by splitting up the data sample in D^0 and $\overline{D}^0$ candidates (for more details see subsubsection 2.5.1) and performing a simultaneous binned χ^2 fit to both data samples. Four probability density functions (PDFs) are defined to perform the simultaneous fit. Two of these describe the D^0 and $\overline{D}^0$ peak, which share certain parameters, and the remaining two describe the background in the D^0 and $\overline{D}^0$ tagged samples, respectively. This way the signal yield of the two tag categories (N^+ and N^-) can be expressed in terms of the raw asymmetry $\mathcal{A}_{raw}$ and the total yield $N = N^+ + N^-$ as $N^\pm = N(1 \pm \mathcal{A}_{raw})/2$. The final signal PDFs are defined for D^0 and $\overline{D}^0$ candidates as:

$$\mathcal{PDF}^{sig}_{D^0} = \frac{N}{2}(1 - \mathcal{A}_{raw})((1 - f_1)\mathcal{G}(m|\mu_G, \sigma_{G,D^0}) + f_1\mathcal{J}(m|\mu_J, \sigma_{J,D^0}, \nu_{D^0}, \tau_{D^0})) \tag{5.8}$$

$$\mathcal{PDF}^{sig}_{\overline{D}^0} = \frac{N}{2}(1 + \mathcal{A}_{raw})((1 - f_1)\mathcal{G}(m|\mu_G, \sigma_{G,\overline{D}^0}) + f_1\mathcal{J}(m|\mu_J, \sigma_{J,\overline{D}^0}, \nu_{\overline{D}^0}, \tau_{\overline{D}^0})) \tag{5.9}$$

μ_G and σ_G are mean and standard deviation of the normal distribution, respectively.

For the control channel $D^0 \to K^-\pi^+$ the signal position (*i.e.*, μ_G and μ_J) are shared for D^0 and $\overline{D}^0$ decays. Whereas the width and tail parameters ($\sigma_G, \sigma_J, \nu, \tau$) are free to float independently for D^0 and $\overline{D}^0$ decays. This is done to account for possible different detector effects, regarding the different final state particles $K^-\pi^+$ for D^0 and $K^+\pi^-$ for $\overline{D}^0$. Because of symmetric final state of the signal channel no different detector effects, for the different tags, are expected. All signal parameters for the signal channel are shared between D^0 and $\overline{D}^0$. Additionally, the mean positions of the normal distribution and the Johnson's S_U are shared ($\mu_G = \mu_J$). The fraction of the radiative tail is expected to be the same for D^0 and $\overline{D}^0$ candidates. The fraction f_1 is shared for the control and signal channel. All background parameters for the different tagged data samples are allowed to vary independently.

From these four PDFs one χ^2 value is constructed which is minimised to estimate the signal yield. The χ^2 value is defined by

$$\chi^2 = \sum_{i=1}^{N_{bin}} \frac{(O_{D^0,i} - E_{D^0,i})^2}{O_{D^0,i}} + \sum_{i=1}^{N_{bin}} \frac{(O_{\overline{D}^0,i} - E_{\overline{D}^0,i})^2}{O_{\overline{D}^0,i}} \tag{5.10}$$

where $O_{D^0,i}$ ($O_{\overline{D}^0,i}$) is the observed count in bin i of the D^0 ($\overline{D}^0$) mass spectrum, $E_{D^0,i}$ ($E_{\overline{D}^0,i}$) the expected count in bin i of the D^0 ($\overline{D}^0$) mass spectrum and N_{bin} the number of bins.

So far the mass fit model was implemented for the decay-time integrated dataset. To estimate the time-dependent slope of the raw asymmetry, the data, additionally to the tag, is split in 20 equally populated decay-time bins. The binning is not expected and should not influence the measurement, which is also validated by pseudo experiments (for more details see subsection 7.2). As the size of the data sample for one fit decreases by an order of magnitude, equally populated decay-time bins are chosen to guarantee a stable fit behaviour, due to smaller statistical fluctuations in the data sample. To further increase the stability of the fit in each decay-time bin, a decay-time integrated fit is performed, as explained in the previous paragraph, where all signal shape parameters are estimated. All signal shape parameters and the means are fixed as obtained from the time integrated fit, except for one global scale and shift factor for the width and the mean, respectively, in each decay-time bin. No further constraints on the background parameters are set. The slope can float freely in each decay-time bin. All decay-time bins are fitted independently from each other. As summary the shift of the signal position, the scale factor of the signal width, the number of signal events, the raw asymmetry for the signal, the two slopes describing the background for D^0 and $\overline{D}^0$, the total number of background events and the

asymmetry for the number of background events are estimated in each decay-time bin by the fit.

To estimate how well the fitted asymmetry describes the data, the raw asymmetry in each D^0 mass bin, obtained by counting, is compared to the asymmetry obtained by the fit in each mass bin. The decay-time-integrated mass spectra split by tag for $D^0 \to \pi^+\pi^-$, $D^0 \to K^+K^-$ and $D^0 \to K^-\pi^+$ is shown in figure 16 with fit projections overlaid. The measured and fitted raw asymmetry in bins of D^0 mass is shown in the right column. The bottom panel under the fit results and the asymmetries shows the pull distribution. The pull distribution is a graphical illustration of the goodness of the fit. The pull is the difference between the fit function and the data points normalised by the statistical uncertainty of the data.

For the signal channel the fitted PDF is in good agreement with the data sample, whereas a satisfactorily description of the asymmetries is confirmed for the signal and the control channel over the whole mass range. The total signal and background yields and asymmetries can be found in table 3. A raw asymmetry different from zero is observed, expected to origin mainly from the detection asymmetry and small fractions of production asymmetry.

All invariant mass distributions overlaid with fit results and the asymmetry plots can be found for every decay-time bin in appendix B. Additionally, all scale/shift factors, yields and background asymmetries of the mass fits in the various decay-time bins can be found in appendix C. The fitted PDFs and the description of the asymmetries by the PDFs is in good agreement with the data sample.

In addition to the asymmetry comparison of the raw and fitted asymmetry in each D^0 mass bin the p-value distribution for the asymmetry in the different decay-time bins is calculated. The p-value, probability value, represents the probability of the agreement between data and fit model and is expected, if the fit hypothesis is true, to be uniformly distributed between 0 and 1, which is also the case here (see figure 17). The p-values are

channel	N_{sig}	N_{bkg}	$\mathcal{A}_{\text{raw}}{}^{sig}$ $[10^{-4}]$	$\mathcal{A}_{\text{raw}}{}^{bkg}$ $[10^{-4}]$
$D^0 \to K^-\pi^+$	76448275 ± 9713	6913452 ± 4981	-114.4 ± 1.3	-181.5 ± 7.2
$D^0 \to K^+K^-$	9111162 ± 4984	3487539 ± 4384	-28.4 ± 3.7	143.2 ± 6.9
$D^0 \to \pi^+\pi^-$	2923918 ± 3241	1509380 ± 3015	-21.8 ± 6.9	-79.7 ± 10.7

Table 3: Signal and background yields and asymmetries as obtained from the decay-time integrated mass fits for all decay channels.

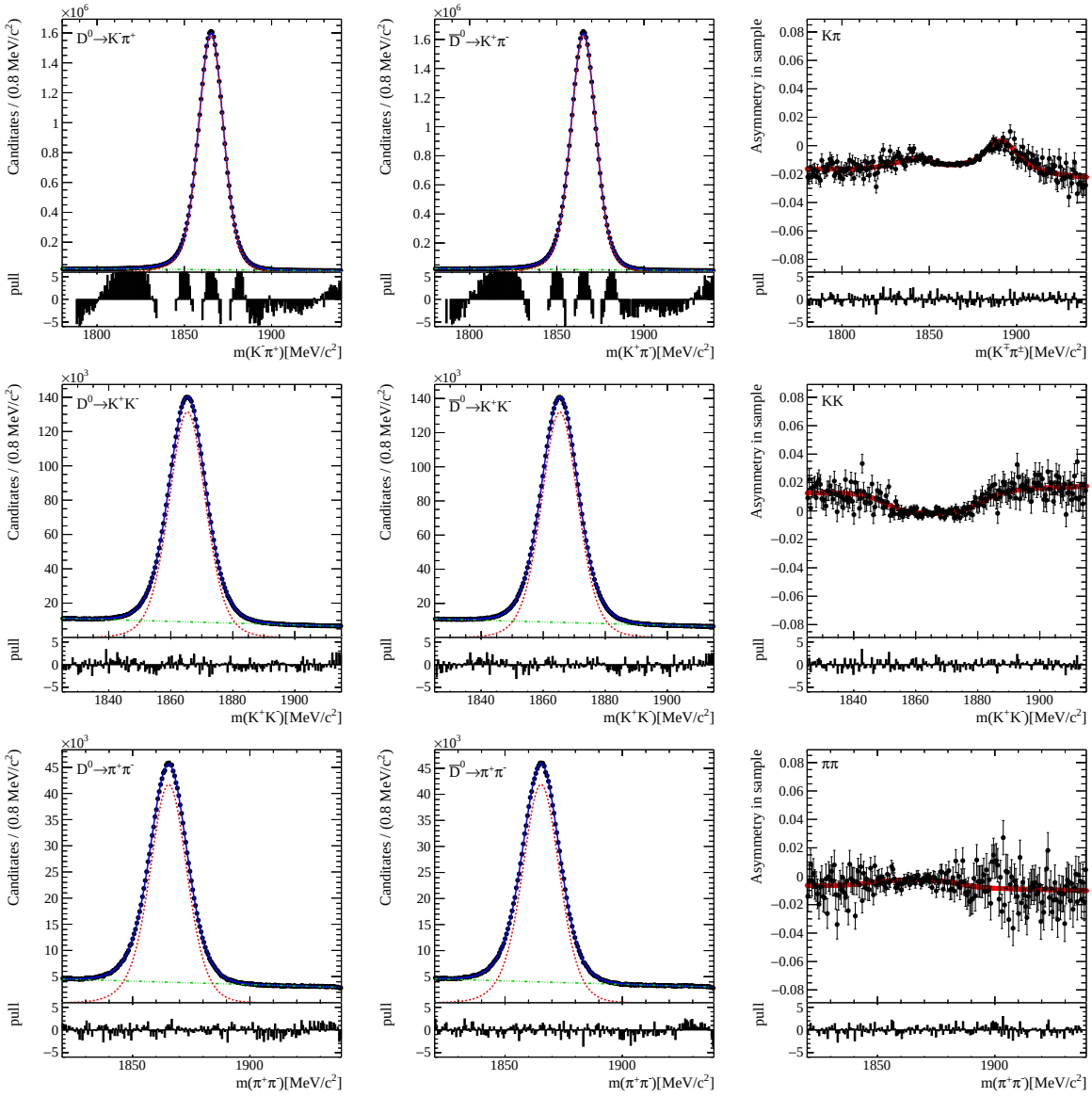

Figure 16: Mass spectra with fit projections overlaid for D^0 (left column) and $\overline{D}^0$ (middle column) candidates for $D^0 \to K^-\pi^+$ (top row), $D^0 \to K^+K^-$ (middle row) and $D^0 \to \pi^+\pi^-$ (bottom row). Also the measured and fitted raw asymmetry in bins of D^0 mass is shown (right column).

directly calculated from the χ^2 value between the raw and fitted asymmetry and gives the probability how well the fitted and the actual observed asymmetry agree. Lastly the fit procedure, including the error calculation, is validated and confirmed with pseudo experiments (for details on the pseudo experiments please see subsection 6.1 and to the validation please see subsection 7.1).

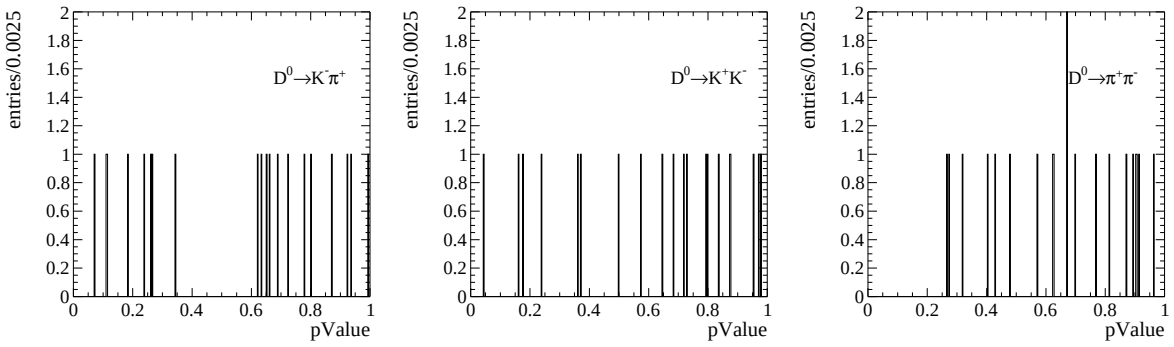

Figure 17: Distribution of the p-values as obtained from the mass fits in bins of decay time for $D^0 \to K^-\pi^+$ (left), $D^0 \to K^+K^-$ (middle) and $D^0 \to \pi^+\pi^-$ (right).

5.2 Estimating A_Γ

The decay-time is exponentially distributed. Therefore the average of the decay-time in each bin is slightly shifted to the lower decay-time bin boundary. To avoid a bias of the average decay-time by the observed background decay-time, the combinatorial background is removed by performing a so called *sideband subtraction* before averaging the decay-time in the signal region. As sideband two equal sized background regions in the D^0 mass symmetrically around the D^0 mass peak are chosen. The signal region consists of background candidates and signal candidates, whereas the background window is chosen in such a way that it only consists out of background candidates. After this is done the summed up decay-time in the sideband is subtracted from the summed up decay-time in the signal region, before being averaged over the number of signal candidates in the signal region:

$$\langle \tau \rangle = \frac{\sum_{i=1}^{N_{sig}} \tau_i - \left(\sum_{i=1}^{N_{bkg1}} \tau_i + \sum_{i=1}^{N_{bkg2}} \tau_i \right)}{N_{sig} - (N_{bkg1} + N_{bkg2})} \tag{5.11}$$

where τ_i is the D^0 decay-time for a single candidate, N_{sig} the number of candidates in the signal region $[1860, 1870]\,\mathrm{MeV}/c^2$ and N_{bkg1} and N_{bkg2} the number of events in the sidebands. The sidebands are defined in the following intervals $[1790, 1795]\,\mathrm{MeV}/c^2$ and $[1935, 1940]\,\mathrm{MeV}/c^2$ for $D^0 \to K^-\pi^+$ candidates, $[1825, 1830]\,\mathrm{MeV}/c^2$ and $[1900, 1905]\,\mathrm{MeV}/c^2$ for $D^0 \to K^+K^-$ candidates, $[1820, 1825]\,\mathrm{MeV}/c^2$ and $[1905, 1910]\,\mathrm{MeV}/c^2$ for $D^0 \to \pi^+\pi^-$ candidates. A linear background is assumed therefore is $N_{sig} - (N_{bkg1} + N_{bkg2})$ equal to the number of expected signal events in the signal region. Figure 18 shows the background subtracted decay-time distribution in the signal region for all decay modes. The binning scheme and the average decay-time in each bin is shown in table 7, appendix D.

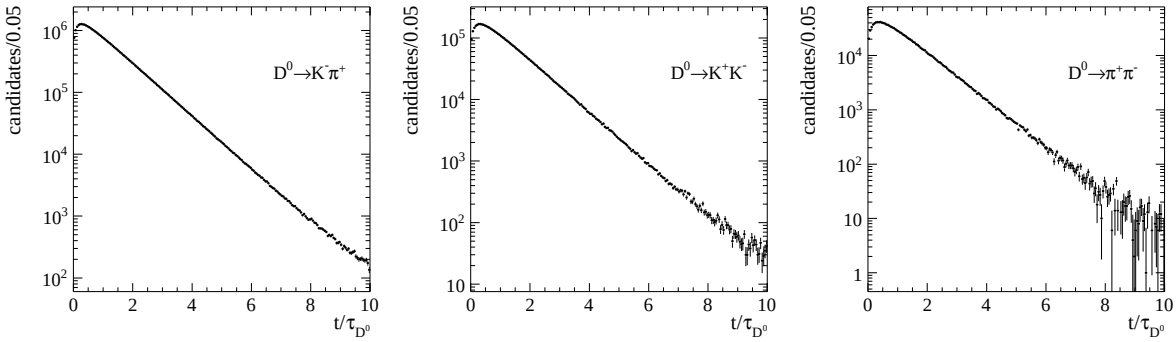

Figure 18: Background subtracted decay-time distribution of finally selected $D^0 \to K^-\pi^+$ (left), $D^0 \to K^+K^-$ (middle) and $D^0 \to \pi^+\pi^-$ (right).

The raw asymmetry for each decay-time bin is plotted over the average decay-time $\langle\tau\rangle$ and the negative slope (A_Γ) is determined by a linear fit. The final result can be seen in figure 19. Note that the error bars in the $x-$direction illustrate the bin width of the decay-time bins in the corresponding plots. The errors on the average decay-time are more than an order of magnitude smaller than the errors on $\mathcal{A}_{\text{raw}}$ and can therefore be neglected.

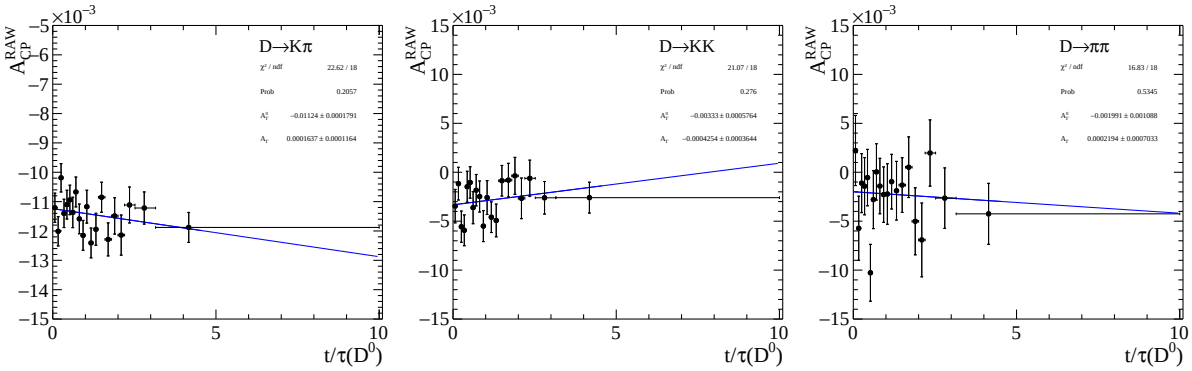

Figure 19: Raw asymmetry $\mathcal{A}_{\text{raw}}$ in bins of decay time with linear fit overlaid for $D^0 \to K^-\pi^+$ (left), $D^0 \to K^+K^-$ (middle) and $D^0 \to \pi^+\pi^-$ (right).

The final results for the different signal and for the control channel are:

$$A_\Gamma(K^-\pi^+) = (\ \ 1.6 \pm 1.2) \times 10^{-4}$$
$$A_\Gamma(K^-K^+) = (-4.3 \pm 3.6) \times 10^{-4}$$
$$A_\Gamma(\pi^-\pi^+) = (\ \ 2.2 \pm 7.0) \times 10^{-4}$$

The uncertainties are statistical. Values for A_Γ (K^-K^+) and A_Γ $(\pi^-\pi^+)$ compatible with each other and with zero are observed. The results are compatible with no CP-violation.

Additionally, the control mode ($D^0 \to K^-\pi^+$) is consistent with zero, as expected, which gives a good additional crosscheck for the analysis strategy, given due to the higher statistic in the control channel. Nevertheless, additional cross checks are shown in section 7.

6 Systematic uncertainties

In this chapter the influence of the three major systematic uncertainties is studied. In table 6 the results of the systematic uncertainties as obtained by toy studies are summarised.

The following sources of systematic uncertainties are expected to influence the measurement:

- *Neglected decay-time acceptance and resolution.* The finite resolution has a large impact as more candidates are shifted from higher decay-times to lower decay-times than the opposite for D^0 and $\overline{D}^0$ which directly introduces a systematic bias which scales with the true value of A_Γ.

- *Wrongly tagged D^0 and $\overline{D}^0$ candidates.* The tag is directly correlated with the asymmetry. Wrongly reconstructed candidates, due to wrongly associated muons not originating from the $B \to D\mu X$ transition, can have a wrong flavour tag even though they peak in the D^0 mass. Therefore, it is possible that some D^0 and $\overline{D}^0$ candidates are wrongly tagged, with a certain *mistag* probability. Wrongly tagged D^0 and $\overline{D}^0$ candidates are expected to damp the observed *CP* asymmetry.

- *Parameterisation of the signal and background mass shapes.* The signal yields are measured with the help of binned χ^2 fits to the D^0 mass as explained in detail in section 5. The specific choice of the parameterisation of the PDF (Johnson's S_U + normal distribution for signal, linear description of the background) can directly bias the measured asymmetry.

These effects are studied using large samples of pseudo-experiments using a realistic estimation of the experimental resolution, acceptance and mistag probabilities. Details are given in the following subsections. Furthermore possible unexpected biases are investigated due to decay-time dependent nuisance asymmetries and the BDT selection using the $D^0 \to K^-\pi^+$ control sample. Also uncertainties related to the limited knowledge of the D^0 lifetime and the uncertainty of the detector length scale are studied. The lifetime of the D^0 meson is known to a relative precision of $\sigma_{\tau_{D^0}}/\tau_{D^0} = 0.37\%$ [24], which propagates to an uncertainty of A_Γ of $\Delta A_\Gamma = A_\Gamma \cdot \sigma_{\tau_{D^0}}/\tau_{D^0} \sim \mathcal{O}(10^{-6})$. Similarly, the uncertainty on the z length scale of the detector of $\sigma_z/z = 0.022\%$ [27] translates into an uncertainty of $\Delta A_\Gamma = A_\Gamma \cdot \sigma_z/z \sim \mathcal{O}(10^{-8})$. These two uncertainties are negligible compared to other systematic uncertainties and will be ignored in the following.

6.1 Pseudo experiments

To test the main contributing systematic uncertainties pseudo-data is generated, which is used to simulate possible systematic uncertainties. This is done by generating 1000 toy samples with different configurations on which the measurement is repeated. It follows a short description on how in general the toy samples are generated. For the pseudo-data events with a specific decay-time, a mass and a tag (muon charge) are generated, separately for signal and background. The number of events generated for signal and background has the same statistic as observed from data fluctuated by a Poisson distribution. The number of signal events and background events used in the generation can be found in table 4. For background candidates the decay-time and tag are generated as observed in data. The background mass shape is generated according to the decay-time integrated fit.

The resolution is estimated using simulated candidates and to account for any possible changes the resolution for all systematic uncertainties is increased by 10 %. The acceptance is estimated by dividing the observed decay-time in $D^0 \to K^-\pi^+$ candidates (background subtracted) by the convolution of an exponential decay law, for the D^0-meson, with the given resolution. The signal decay-time τ^{true} is then generated by an exponential decay law which is convoluted by the resolution function:

$$\tau_{Gen} = \tau^{true} * Res \tag{6.1}$$

with the resolution function Res calculated by the difference of the reconstructed decay-time τ^{reco} from the simulated candidates and τ^{true}. Afterwards events are selected according to the calculated acceptance. The resolution and the resulting acceptance used for the toy generation is shown in figure 20.

The tag is generated time-dependent for different values of A_Γ^{Gen} (slope) and $\mathcal{A}_{\text{raw}}(t=0)$ (offset). A region of $A_\Gamma^{Gen} \in [-0.003, 0.003]$ is scanned for a better estimate of the systematic uncertainties and to check possible dependencies between A_Γ^{Gen} and A_Γ. This range is chosen to cover expectations even including new physics. For $\mathcal{A}_{\text{raw}}(t=0)$ the measured decay-time integrated asymmetry is taken. The probability to produce a D^0 event is:

$$P(\mu^-|D^0) = 0.5 \cdot (1 - (\mathcal{A}_{\text{raw}}(t=0) - A_\Gamma^{Gen})) \tag{6.2}$$

The generated asymmetries, as observed in data, can be found in table 4. After the generation the toy samples are treated like data, which means that A_Γ is extracted by the same procedure than it was in data.

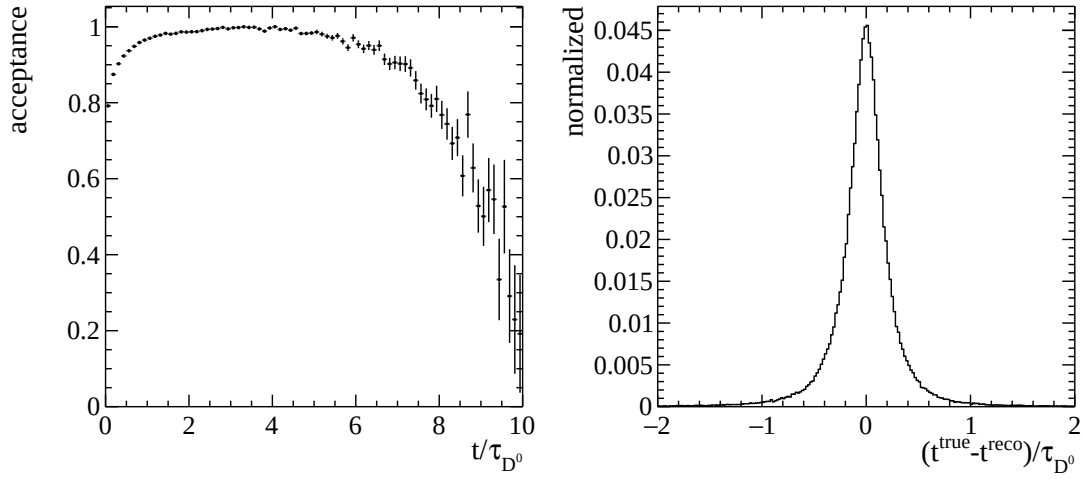

Figure 20: Acceptance (left) and resolution (right) histograms used in the generation of pseudo data. Find details in the text.

Parameter	$D^0 \to K^+K^-$	$D^0 \to \pi^+\pi^-$
N_{sig}	$9.1M$	$2.9M$
N_{bkg}	$3.5M$	$1.5M$
$\mathcal{A}_{\text{raw}}(t=0)$	$-28 \cdot 10^{-4}$	$-22 \cdot 10^{-4}$
$\mathcal{A}_{\text{raw}}{}^{bkg}(t=0)$	$143 \cdot 10^{-4}$	$-80 \cdot 10^{-4}$
A_Γ^{bkg}	$-72 \cdot 10^{-4}$	$60 \cdot 10^{-4}$

Table 4: Default parameters used in the generation of the pseudo experiments.

6.2 Decay-time acceptance and resolution

The effect of a non-uniform decay-time acceptance and a finite resolution can bias the observed time-dependent asymmetries. A systematic bias which scales with A_Γ^{Gen} is expected.

The observed bias on A_Γ is shown in figure 21 as a function of its input value. The bias is dominated by the effect of the decay-time resolution and shows a linear dependence on the input value, resulting in a multiplicative bias. Because of the still precise experimental knowledge of A_Γ, at the current level and to have an independent estimate of the systematic uncertainties the current world average is used to estimate the multiplicative systematic uncertainties[4]. The A_Γ multiplicative factors are $5.7 \cdot 10^{-2}$ for $D^0 \to K^+K^-$ and $5.1 \cdot 10^{-2}$ for $D^0 \to \pi^+\pi^-$. This translates into a systematic uncertainty of $0.3 \cdot 10^{-4}$ for $D^0 \to K^+K^-$

[4]This is only possible as the measured value of A_Γ in this thesis is compatible with the world average.

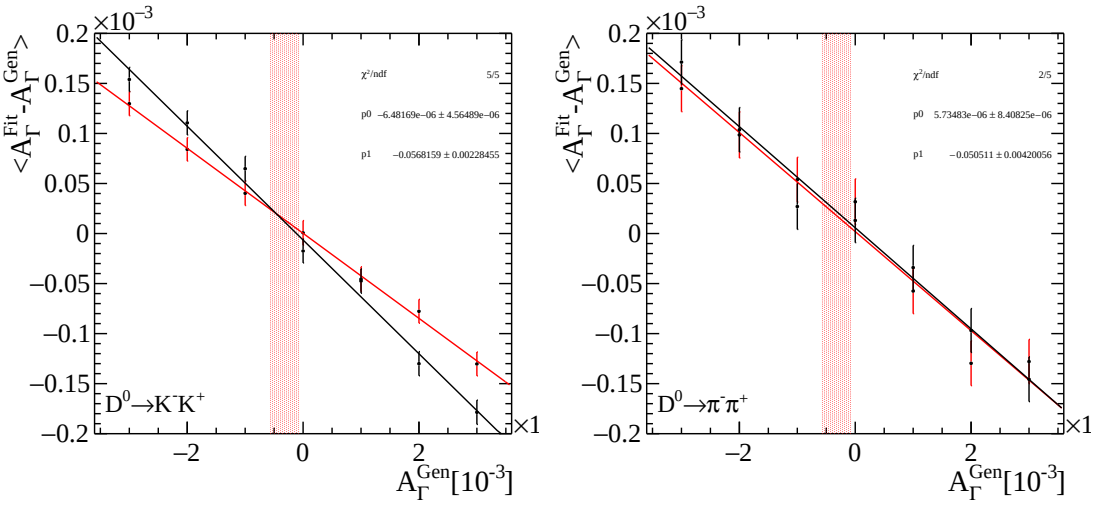

Figure 21: Bias observed when considering decay time acceptance and resolution for $D^0 \to K^+K^-$ (left) and $D^0 \to \pi^+\pi^-$ (right). A linear function is fitted to determine the systematic uncertainty. Find details in the text.

and $0.4 \cdot 10^{-4}$ for $D^0 \to \pi^+\pi^-$ taking the largest bias observed within an 1σ confidence interval around the world average of $A_\Gamma = (-3.2 \pm 2.6) \cdot 10^{-4}$ [28].

6.3 Wrongly tagged D^0 and $\overline{D}^0$ candidates

The charge of the muon from the b-hadron decay is used to tag the flavour of the neutral D^0 meson at production time. But the reconstruction of the b-hadron decay is not perfect and so there is a certain probability that the muons are wrongly identified. These wrongly associated muons with mistag probabilities ω_{D^0} and $\omega_{\overline{D}^0}$ for D^0 and $\overline{D}^0$ mesons, respectively, bias the observed asymmetries. In the limit of small asymmetries it is possible [29], by defining the average mistag rate $\bar{\omega}(t)$ and their difference $\Delta\omega(t)$, to express the raw asymmetry by the following linear expression:

$$\mathcal{A}_{\text{raw}}(t) = (1 - 2\bar{\omega}(t))\big[\mathcal{A}_{CP}(t) + A_{prod} + A_{det}\big] - \Delta\omega(t), \tag{6.3}$$

with

$$\overline{\omega}(t) = 0.5 \cdot (\omega_{D^0}(t) + \omega_{\overline{D}^0}(t)), \quad \Delta\omega(t) = \omega_{D^0}(t) - \omega_{\overline{D}^0}(t) \tag{6.4}$$

The average mistag rate directly dilutes the measured asymmetry, whereas $\Delta\omega(t)$ only influences the measured value of A_Γ if it is time-dependent, otherwise it just shifts $\mathcal{A}_{\text{raw}}$ by a constant factor and would therefore be negligible.

The mistag probabilities are studied with help of the $D^0 \to K^-\pi^+$ control channel. In contrast to the charge-symmetric final states of the signal modes the $K^-\pi^+$ final state is almost self-tagged which allows to study the ratio of "wrong sign" $((K^\mp\pi^\pm)\mu^\pm)$ over "right sign" $((K^\mp\pi^\pm)\mu^\mp)$ final states for D^0 mesons. The wrong sign decays, in contrast to the right sign decays, are suppressed by the CKM matrix. Therefore all wrong sign decays arise from suppressed decays, D^0-meson mixing and wrongly tagged decays. To be insensitive to the kaon detection asymmetry the following ratios are defined:

$$R_{D^0} = \frac{N((K^-\pi^+)\mu^+)}{N((K^-\pi^+)\mu^-)}, \qquad R_{\overline{D}^0} = \frac{N((K^+\pi^-)\mu^-)}{N((K^+\pi^-)\mu^+)} \tag{6.5}$$

In this way, all kaon and pion detector effects do cancel because of the fraction, and only effects due to the muon are visible. To access randomly associated combinations, the ratio R_{D^0} is corrected for the known rate of wrong sign decays arising from mixing and doubly-Cabbibo suppressed decays using the measurements from Ref. [30], the correction on the final mistag probability is of $\mathcal{O}(10^{-3})$. The ratio R_{D^0} is then transformed into the mistag probability using the relation $\omega_{D^0} = R_{D^0}/(1 + R_{D^0})$. To take into account the different selection criteria, the wrong sign over right sign ratio is estimated with the $D^0 \to K^+K^-$ selection applied on the $D^0 \to K^-\pi^+$ sample and the $D^0 \to \pi^+\pi^-$ selection applied on the $D^0 \to K^-\pi^+$ sample. For this purpose the BDT selection trained on the $D^0 \to K^+K^-$ ($D^0 \to \pi^+\pi^-$) data sample is applied to the control channel before the wrong sign over right sign ratio is estimated. The resulting mistag probabilities are shown as a function of decay time separately for D^0 and $\overline{D}^0$ in figure 22. On the left the mistag rate is shown for the $D^0 \to K^+K^-$ and on the right for $D^0 \to \pi^+\pi^-$ selection. The difference between D^0 and $\overline{D}^0$ mistag rate $\Delta\omega(t)$ is shown in the panel below, respectively for the different selections. The time-dependence in the mistag rate is introduced by the fact, that it is more likely that the wrongly associated muon originates from a decay closer to the primary vertex than where the missed muon was correctly produced and therefore the (wrongly) reconstructed flying distance increases for mistaged events. The fraction of mistaged events compared to correctly tagged events increases over the decay-time.

To study the impact on the measurement the time-dependent mistag rate is used to alter the generated tag. This is done by introducing a fraction of mistagged events, given by the mistag probability in figure 22, to the total number of generated events. In figure 22 in the lower frame the mean of the measured A_Γ as function of generated A_Γ is shown, linear subtracted by resolution and acceptance effects. This way it is possible to see only the effect introduced by the mistag. A linear dependence of the bias on the input A_Γ is observed. The offset is expected to be introduced by $\Delta\omega(t)$, while the slope is expected to be introduced by $\overline{\omega}$. Here again the uncertainty is evaluated for the $1\,\sigma$ range of the

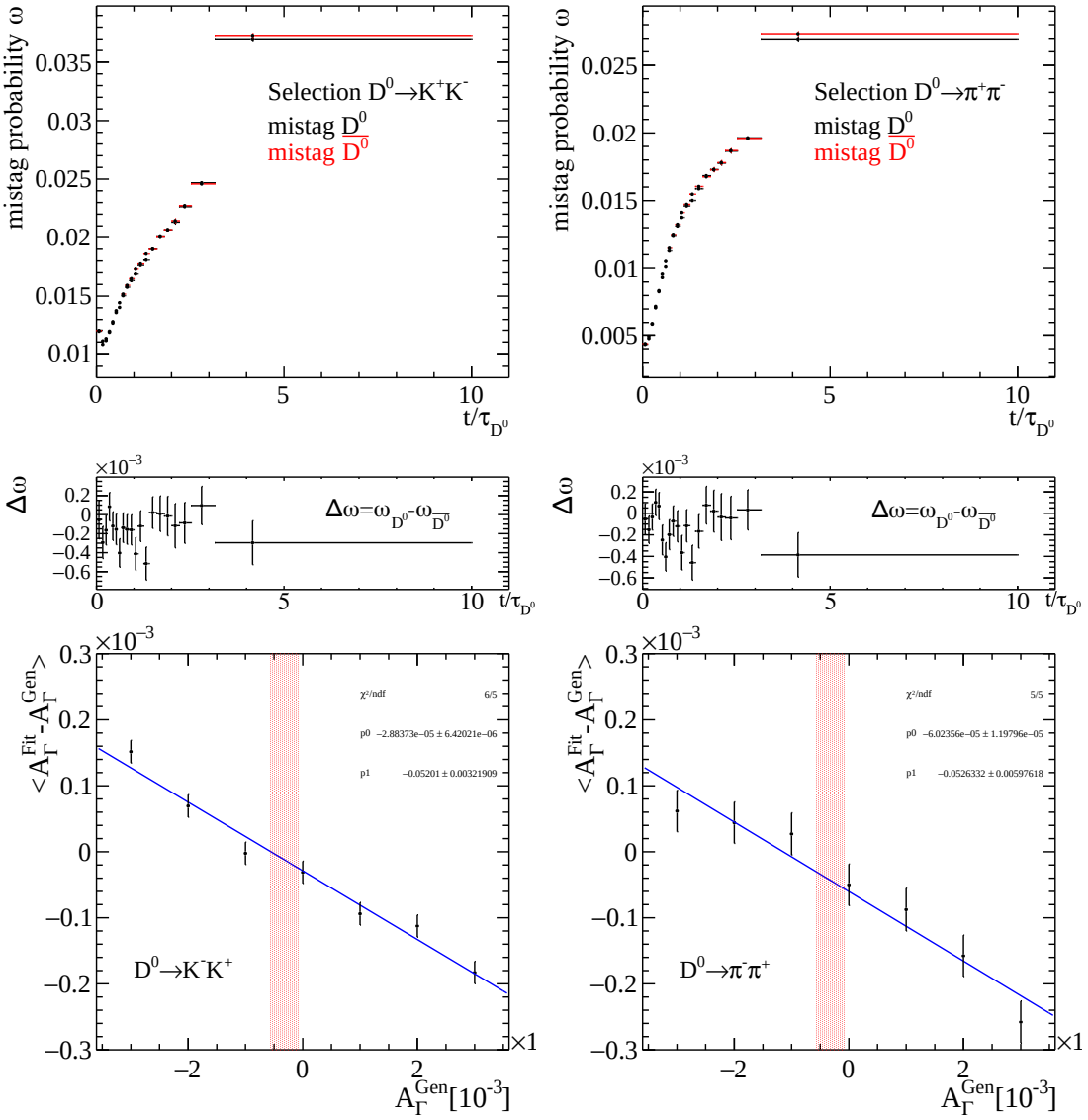

Figure 22: (Top) Mistag probability ω for D^0 and $\overline{D}^0$ candidates used in the generation of pseudo experiments as measured in the control mode $D^0 \to K^-\pi^+$. The mistag probabilities are determined individually after applying the $D^0 \to K^+K^-$ BDT (left) and $D^0 \to \pi^+\pi^-$ BDT (right). (Bottom) Bias observed when considering the mistag probabilities in the toy generation as function of the signal A_Γ.

world average, which yields a systematic uncertainty of $0.3 \cdot 10^{-4}$ for $D^0 \to K^+K^-$ and $0.6 \cdot 10^{-4}$ for $D^0 \to \pi^+\pi^-$ (combining additive offset and dilution effects). From figure 22 one would not expect an additive contribution, as the slope of $\Delta\omega(t)$ is compatible with zero, therefore is interesting to notice here that the uncertainty introduced by $\Delta\omega(t)$ is of the same size than the statistical uncertainty on the slope of $\Delta\omega(t)$ and therefore limited

by the statistics of the control sample. Also important to notice here is that for the world average ($A_\Gamma = (-3.2 \pm 2.6) \cdot 10^{-4}$) [28] the systematic uncertainties for the resolution and acceptance and the mistag cancel each other out, but to be conservative both uncertainties are evaluated independently from each other.

6.4 Mass model

The signal yields are measured using binned χ^2 fits to the reconstructed D^0 mass as explained in detail in section 5. To investigate potential biases caused by the choice of the parameterisation of the PDF, toy data are generated with alternative mass shapes for background and signal. With these alternatively generated toy samples, the measurement of A_Γ is then repeated using the default mass fit model. Remember: The signal in the default mass fit model is described by a Johnson's S_U + normal distribution and the background by a linear function. First it is tested how the default model behaves for a symmetric signal mass peak, *i.e.* no Bremsstrahlung. This is done by generating data distributed symmetrically by two normal distributions. The best possible shape for the two normal distributions is estimated by performing a fit to the decay-time integrated data for $D^0 \to \pi^+\pi^-$ and $D^0 \to K^+K^-$ respectively. Then the impact of a radiative tail for the lower mass spectrum in addition to the signal hypothesis is tested. Therefore, an alternative model is chosen which is expected to describe the tail as good as possible in the mass window. The shape of the alternative mass model is taken from Ref. [2]. To simulate the data as best as possible all pseudo experiments are generated with acceptance and resolution. After the fit procedure is complete the effect of the resolution and the acceptance are linear subtracted to evaluate the effect of the parametrisation independent from other systematic sources.

The background assumption is tested by first assuming a different background shape (exponential background) and secondly by introducing misidentified $D^0 \to K^-\pi^+$ candidates in the toy generation. The signal candidates are produced according to the default mass fit model. The shape of the exponential function is determined by performing an simultaneous fit to the invariant D^0 and $\overline{D}^0$ mass with the default mass model for the signal and an exponential background to the decay-time integrated data set. Even though the misidentified particles are neglected in the measured mass window, after the applied cut on the D^0 mass window, a small fraction of misidentified particles is still present. The shape and fraction of the misidentified $D^0 \to K^-\pi^+$ candidates is taken from Ref. [2] . The shape of the misidentified particles is given by a normal distribution. In table 5 all shape parameters and the number of misidentified events in the measured D^0 mass window, as obtained from Ref. [2], are summarised.

Parameter	$D^0 \to K^+K^-$	$D^0 \to \pi^+\pi^-$
N_{misID}	360	1500
μ	1939.80	1787.27
σ	8.67	13.15

Table 5: Expected number of misidentified $D^0 \to K^-\pi^+$ candidates in the measured mass window and their shape parameters.

The bias is expected to be independent of A_Γ^{Gen}. Nevertheless, as additional crosscheck and to further validate the measurement, the mean of the residuals, as obtained by the pseudo-experiments, is shown as function of A_Γ^{Gen} in figure 23. No dependency to A_Γ^{Gen} is observed. As systematic uncertainty the RMS across the observed variations for different input signal asymmetries, between the different background and signal models is taken. The systematic uncertainty for $D^0 \to K^+K^-$ is $0.3 \cdot 10^{-4}$ and for $D^0 \to \pi^+\pi^-$ is $0.3 \cdot 10^{-4}$.

6.5 Summary of systematic uncertainties

All non-negligible systematic uncertainties larger than $\mathcal{O}(10^{-6})$ are summarised in table 6. Dominant sources of systematic uncertainties are the mass-model, decay-time resolution and time-dependent mistag probabilities.

All uncertainties are treated as independent from each other and are summed up quadratically for the total systematic uncertainty. The total systematic uncertainty amounts to $0.5 \cdot 10^{-4}$ for $D^0 \to K^+K^-$ and $0.8 \cdot 10^{-4}$ for $D^0 \to \pi^+\pi^-$, which is small compared to the statistical precision of the measurement ($3.6 \cdot 10^{-4}$ and $7.0 \cdot 10^{-4}$).

Uncertainty	$D^0 \to K^+K^-$ $[10^{-4}]$	$D^0 \to \pi^+\pi^-$ $[10^{-4}]$
Decay time resolution and acceptance	0.3	0.4
mistag	0.3	0.6
Mass model	0.2	0.3
Total systematic	0.5	0.8
Statistical	3.6	7.0

Table 6: Summary of non-negligible systematic uncertainties.

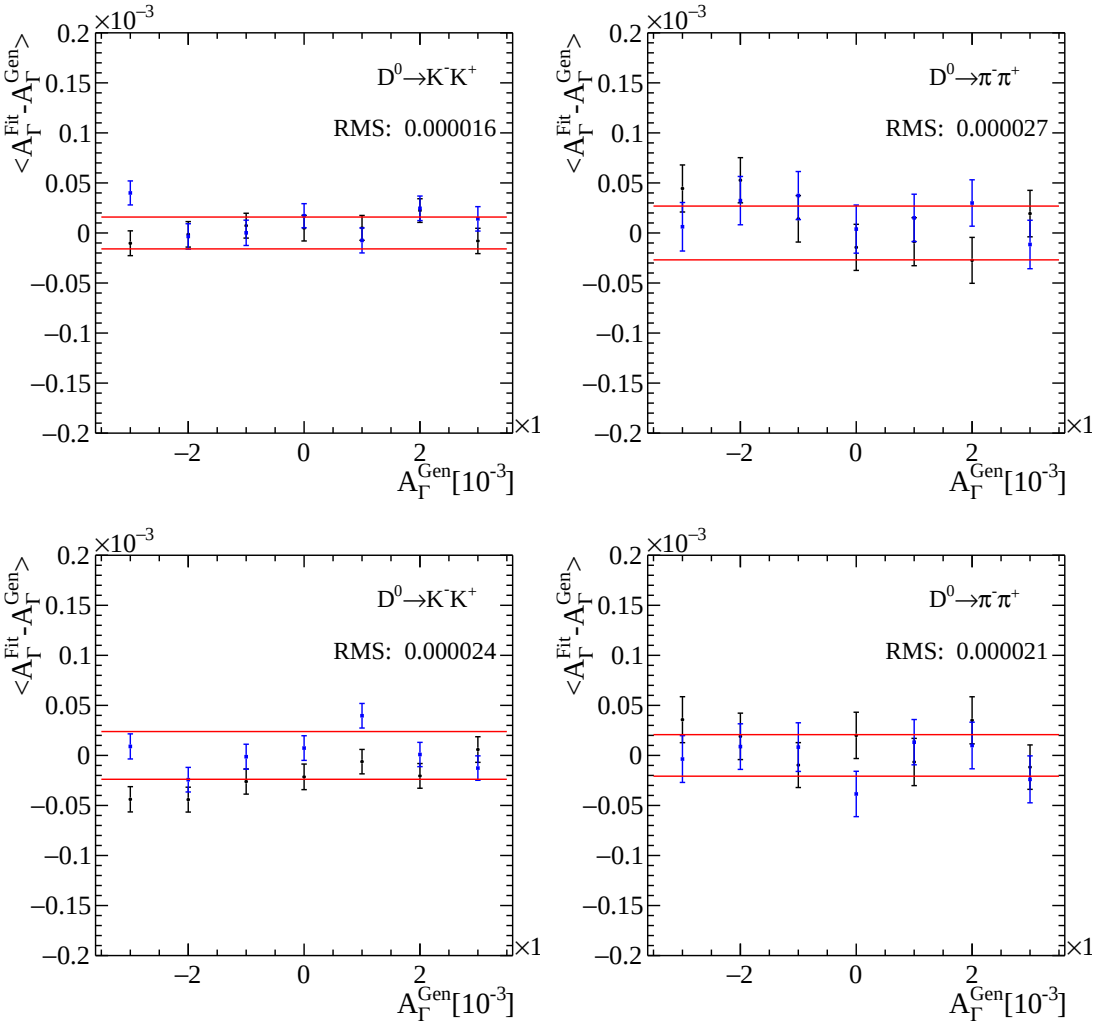

Figure 23: Systematic study of the effect due to the specific choice of the parameterisation of the signal and background PDFs. The residuals are shown as obtained by generating pseudo-experiments with alternative signal (top row) and background (bottom row) models and re-fitting with the default model. Find details on the PDFs in the main text.

7 Crosschecks

To test the internal consistency of the measurement and test for systematic effects that have not been considered so far, several checks are performed.

In detail will be first discussed how the fit is validated. Afterwards, to not miss any possible sources of systematic uncertainties, is checked that the binning scheme, decay-time-dependent production and detection asymmetries and the MVA selection do not introduce any systematic effects. At last several splittings to the data sample are performed to show that the measurement is not biased by the corrected B mass and the magnet polarity.

7.1 Fit validation

To test that the fit returns unbiased estimates of the true asymmetry and its uncertainties, large samples of pseudo-experiments have been generated with hypothetical A_Γ^{Gen} values ranging from -3×10^{-3} to 3×10^{-3} in steps of 1×10^{-3}. To have a good estimate if the fit works the distribution of the pull, defined as $(A_\Gamma^{fit} - A_\Gamma^{Gen})/\sigma^{fit}$, is used. The pull is a direct estimation of how well A_Γ^{Gen} can be measured. For a correct estimate of A_Γ a mean of zero and for a correct error estimation of A_Γ a width of 1 for the pull distribution is expected. To estimate the mean and pull width a normal distribution to the distribution of the pull is fitted. The different pull distributions with the fit projection overlaid can be found in appendix E. In figure 24 an example of the pull distribution (corresponding to $A_\Gamma^{Gen} = 0$) with fit projection is overlaid. In the bottom row all resulting means and widths from the pull distribution are compared. The widths and means are all compatible with 1 and 0, respectively, validating that the fitting procedure works correctly and yields unbiased results and error estimates.

7.2 Decay-time binning scheme

To test if the chosen decay-time binning has any influence on the measurement, different binning schemes are tested. This is done by generating a large amount of toy samples with different seeds and a given A_Γ^{Gen}. The sample is then split in 15, 20 (default), 25 decay-time bins. The subsequent determination of A_Γ does not reveal any biases. Corresponding plots can be found in appendix D. To directly compare the difference between the binning schemes the weighted mean over all A_Γ^{Gen} is computed for every binning scheme and decay. This result can be found in figure 25 the pull mean and width

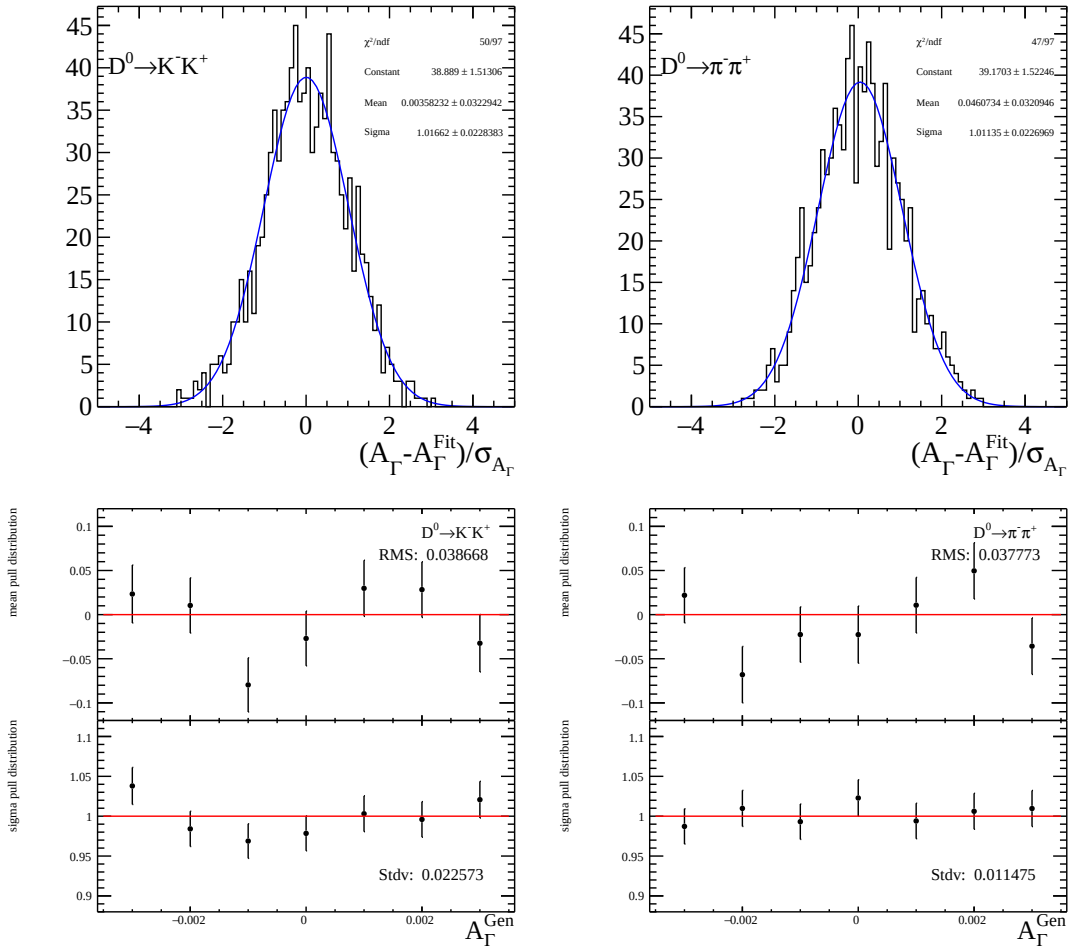

Figure 24: (Top) Distributions of the A_Γ pulls for $D^0 \to K^+K^-$ (left) and $D^0 \to \pi^+\pi^-$ (right) pseudo-experiments generated with input $A_\Gamma = 0$, with Gaussian fit overlaid. (Bottom) Distributions of the pull mean and width, as a function of the input value of A_Γ.

are again compatible with 0 and 1.

7.3 Decay-time-dependent production and detection asymmetries

The control channel is not sensitive to *CPV* asymmetries, so any asymmetry measured in $D^0 \to K^-\pi^+$ decays must be caused by detector effects. As explained in subsection 2.5, the measured raw asymmetry contains contributions from the production asymmetry A_{prod} of the parent b hadron, and detection asymmetries A_{det} of the final state particles. A priori, these nuisance asymmetries do not depend on the decay time of the D^0 meson and appear as constant offset in the measurement of A_Γ. However, due to selection

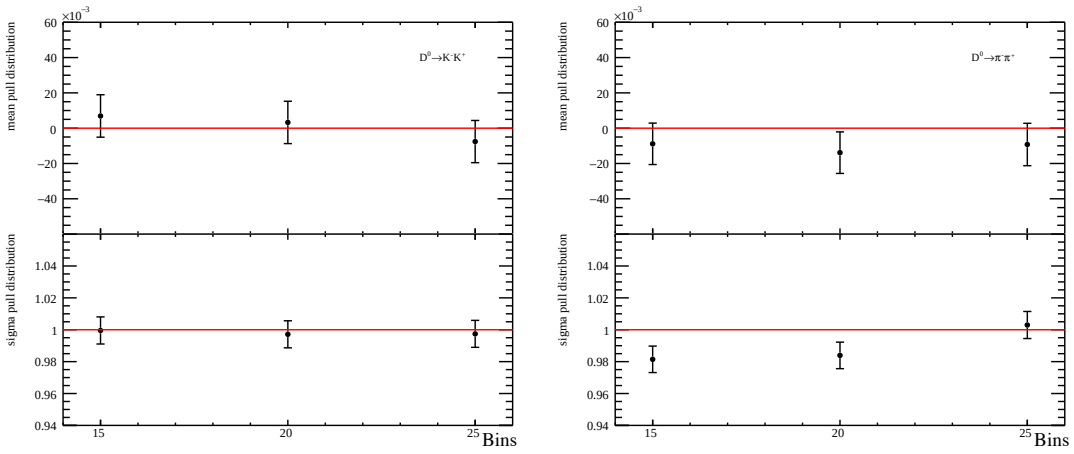

Figure 25: Distributions of the pull mean and width, as a function of the number of bins averaged over $A_\Gamma^{Gen} \in [-0.003, 0.003]$.

requirements, correlations between the kinematics of the final state particles and the decay-time can be introduced. If further the nuisance asymmetries are correlated with these kinematics, also a dependency of detector induced asymmetries on the decay-time is possible, this can fake a non-zero A_Γ. For the control channel $D^0 \to K^-\pi^+$ A_Γ is

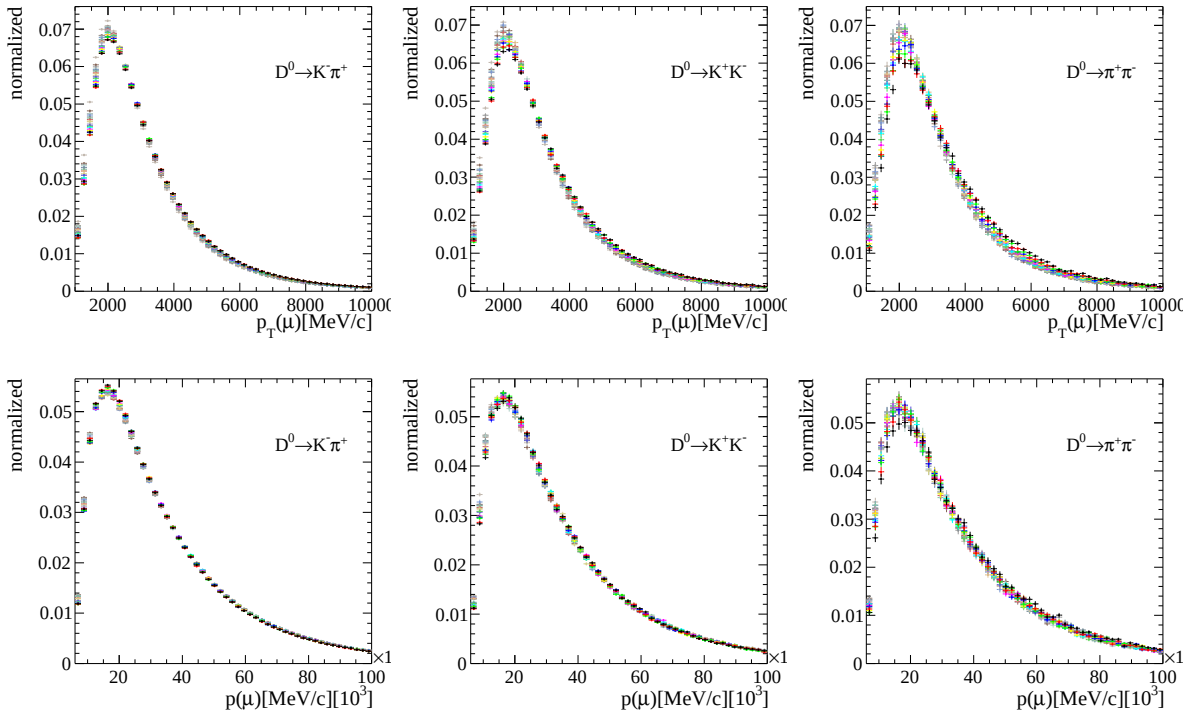

Figure 26: Tag muon kinematics measured in the individual decay time bins for $D^0 \to K^-\pi^+$ (left), $D^0 \to K^+K^-$ (middle) and $D^0 \to \pi^+\pi^-$ (right).

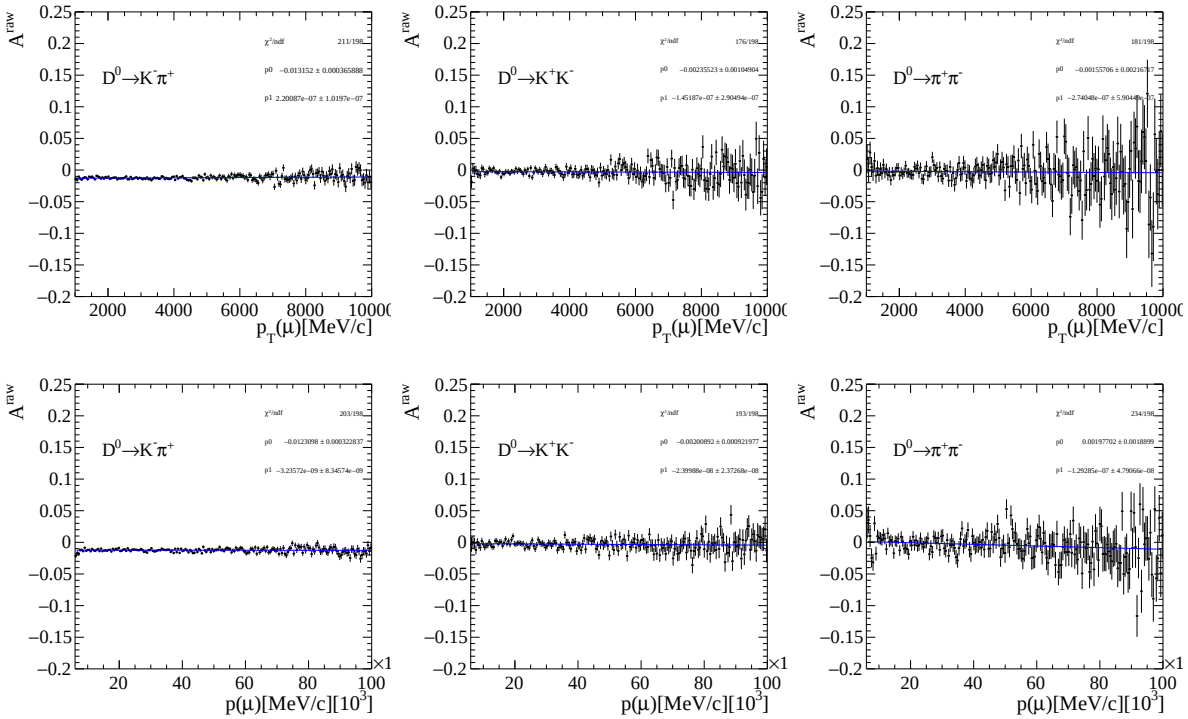

Figure 27: Raw asymmetry $\mathcal{A}_{\text{raw}}$ in bins of tag muon kinematics with linear fit overlaid for $D^0 \to K^-\pi^+$ (left), $D^0 \to K^+K^-$ (middle) and $D^0 \to \pi^+\pi^-$ (right).

measured to be $(1.6 \pm 1.2) \cdot 10^{-4}$, *i.e.* consistent with zero within uncertainties, indicating no unaccounted time-dependent nuisance asymmetries. Nevertheless, by construction of A_Γ, only the muon detection asymmetries are expected to possibly bias the measurement. Therefore, the muon kinematics in bins of decay-time are compared, as shown in figure 26, where the muon p and p_T spectra measured in all decay-time bins are overlaid. From these plots it is visible that there is a small correlation between the muon kinematics and the D^0 decay-time in particular for the $D^0 \to \pi^+\pi^-$ sample.

To check that this correlation does not propagate into a bias of A_Γ the raw asymmetry is measured as a function of the muon kinematics (p and p_T) in figure 27. For this purpose background subtracted decays in the signal window are used (for more details to the background subtraction see equation 5.11). To check if a bias is introduced a linear fit, to each of the asymmetry distributions, as function of muon momenta is performed. The measured slope is compatible with zero. The raw asymmetry can be treated as independent of the muon kinematics and hence also independent of the decay-time. Therefore, no additional systematic uncertainty is assigned.

7.4 Bias due to BDT selection

As explained in section 4, the selection is adopted from a time-integrated measurement. To check that the BDT selection is not causing any time-dependent asymmetries, A_Γ is determined on the control channel with and without signal BDT selection applied. By comparing the resulting two values of A_Γ it is possible to test if the BDT selection introduces a time-dependent asymmetry. The comparison of the time-dependent asymmetries is shown in figure 28, where the asymmetries in each decay-time bin shows only very small variations. The measured values of A_Γ agree to a level of $(0.0 \pm 0.2) \cdot 10^{-4}$ ($D^0 \to K^+K^-$ BDT selection) and $(0.6 \pm 0.4) \cdot 10^{-4}$ ($D^0 \to \pi^+\pi^-$ BDT selection) and are therefore consistent with statistical fluctuations. Therefore no additional systematic uncertainty is applied.

7.5 Consistency checks

The measurement is repeated in different independent subsamples. In an ideal case the measured value of A_Γ should be independent of the magnet polarity. Nevertheless, a splitting by the polarity and the year of data taking is used to additional confirm the robustness and reliability of this analysis. The result can be found in figure 29, no bias is observed. The measurement is also repeated in bins of the corrected mass of the parent b-hadron, as the (neglected) probability for B decays to final state particles via intermediate particles rises for lower corrected masses, resulting in potentially wrong

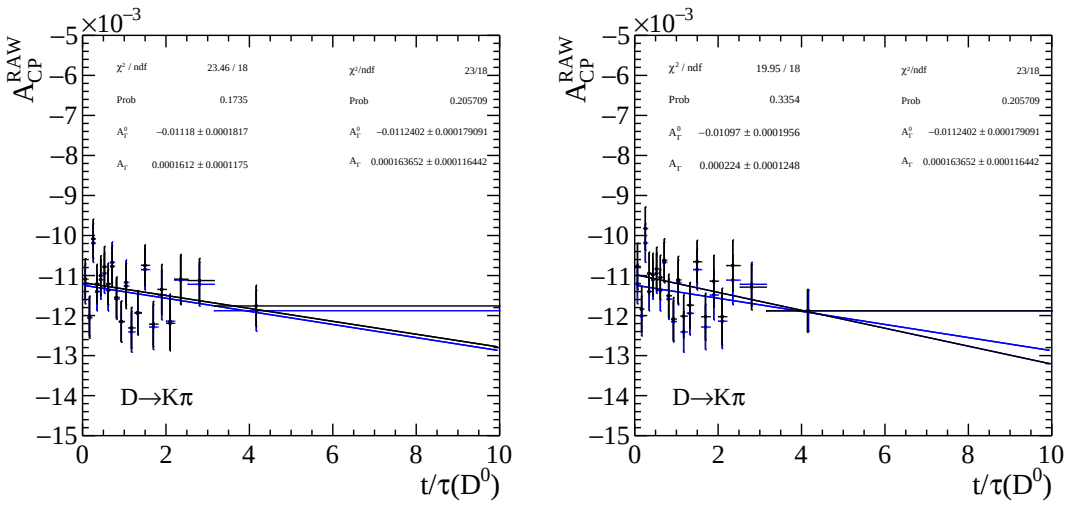

Figure 28: Raw asymmetry $\mathcal{A}_{\text{raw}}$ for $D^0 \to K^-\pi^+$ decays with $D^0 \to K^+K^-$ (left) and $D^0 \to \pi^+\pi^-$ (right) BDT selection applied (in black) and no BDT (in blue) as reference.

decay-time reconstruction for lower corrected masses [31], this assumption is based on Monte Carlo simulations. The results can be found in figure 30. No unexpected variations are observed.

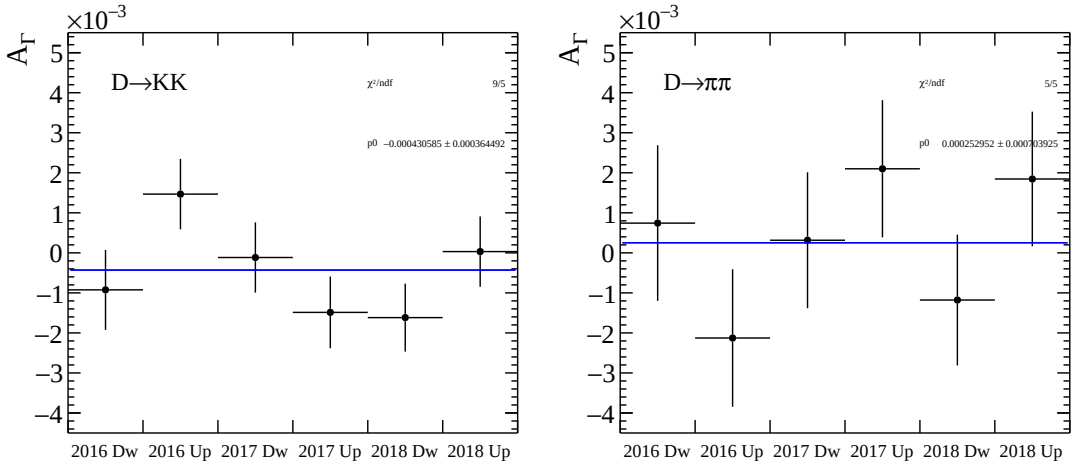

Figure 29: Measurement of A_Γ in $D^0 \to K^+K^-$ (left) and $D^0 \to \pi^+\pi^-$ (right) decays in subsamples split by year of data taking and magnet polarity.

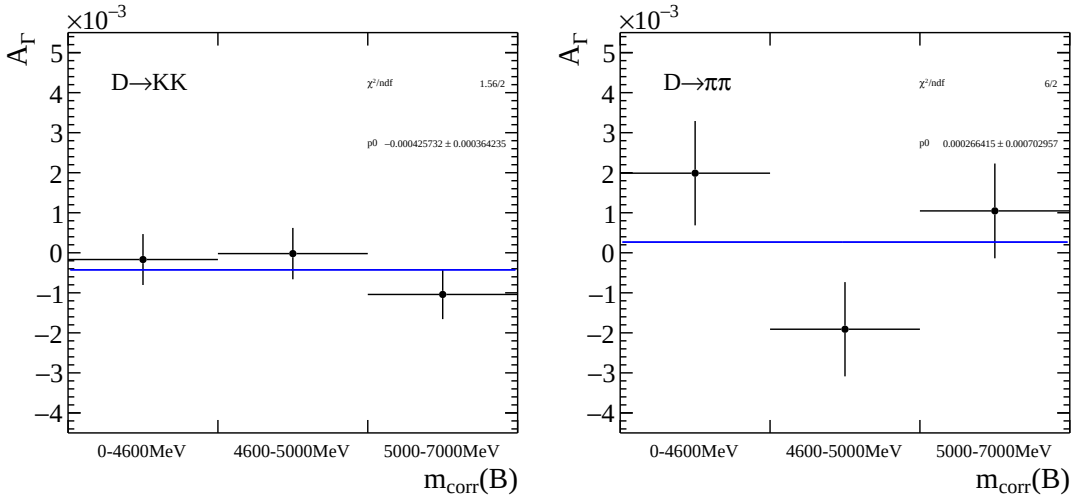

Figure 30: Measurement of A_Γ in $D^0 \to K^+K^-$ (left) and $D^0 \to \pi^+\pi^-$ (right) decays in subsamples split the corrected mass of the B-hadron candidate.

8 Summary

This thesis describes the measurement of the asymmetry (A_Γ) between the effective lifetime of D^0 and $\overline{D}^0$ in $D^0 \to K^+K^-$ and $D^0 \to \pi^+\pi^-$ decays. A_Γ is a powerful observable for indirect *CP* violation. The measurement is performed using data from proton-proton collision corresponding to a integrated luminosity of about $5.4\,\text{fb}^{-1}$, collected by LHCb during the years 2016-2018. By using D^0, arising from $B \to D^0\mu\nu$, it is possible to determine the flavour of the D^0 at production time. In this thesis is outlined how the event is reconstructed and the offline selection, used to reduce the background from various sources, is explained. After this, to further optimise the measurement, a small number of new selection criteria are applied to the data sample. Then the data is split by flavour and decay-time, and the asymmetry between the number of D^0 and $\overline{D}^0$ candidates is estimated statistically as function of the decay-time. From the time-dependent asymmetry the negative slope is then extracted.

A study with pseudo-experiments is performed, which simulates the features of the real data. Using these pseudo-experiments several sources of systematic uncertainties are identified and evaluated. These pseudo-experiments are also used to validate the procedure of the measurement and vice versa. The final unblinded results of this measurements are:

$$A_\Gamma(D^0 \to \pi^+\pi^-) = (\ \ 2.2 \pm 7.0 \pm 0.8) \times 10^{-4},$$
$$A_\Gamma(D^0 \to K^+K^-) = (-4.3 \pm 3.6 \pm 0.5) \times 10^{-4}.$$

The result is compatible with the absence of indirect *CP* violation in charm decays. As A_Γ is predicted to be $A_\Gamma \approx 0.3 \times 10^{-4}$ [32], therefore, these results are in agreement with the standard model predictions. This measurement further improves the world average of A_Γ. Through the increased statistic in this sample it was possible to reach the same precision than the prompt measurement in Run 1 [33] and twice the precision from the semileptonic measurement in Run 1 [34]. All values are compatible with each other. The new LHCb wide averages for A_Γ are:

$$A_\Gamma(D^0 \to \pi^+\pi^-) = (\ \ 2.5 \pm 4.3 \pm 0.7) \times 10^{-4},$$
$$A_\Gamma(D^0 \to K^+K^-) = (-4.4 \pm 2.3 \pm 0.6) \times 10^{-4}.$$

where the statistic and systematic uncertainties, with the exception of the systematic uncertainties resulting from effects due to the decay-time resolution, are treated as independent. This is a valid approach due to the different selection criteria for the semileptonically tagged measurements and the different measurement procedure for the promptly tagged measurement. Under the assumption that A_Γ is universal, *i.e.* the same for both decays, the total average is:

$$A_\Gamma = (-2.9 \pm 2.0 \pm 0.6) \times 10^{-4}$$

So far the main limiting factor for A_Γ is still the statistical precision, which is planned to be further improved in Run 3.

References

[1] LHCb collaboration, R. Aaij *et al.*, *Updated measurement of decay-time-dependent CP asymmetries in $D^0 \to K^+K^-$ and $D^0 \to \pi^+\pi^-$ decays*, LHCb-PAPER-2019-032, in preparation.

[2] F. Betti, *CP violation in $D^0 \to K^+K^-$ and $D^0 \to \pi^+\pi^-$ decays and lepton-flavour universality test with the decay $B^0 \to D^{*-}\tau^+\nu_\tau$*, 2019.

[3] A. Di Canto, D. J. Unverzagt, D. S. Mitzel, and S. Stahl, *Measurement of A_Γ in semi-leptonically tagged $D^0 \to K^+K^-$ and $D^0 \to \pi^+\pi^-$ decays with Run2 data* , .

[4] G. R. Farrar and M. E. Shaposhnikov, *Baryon asymmetry of the universe in the minimal standard model*, Phys. Rev. Lett. **70** (1993) 2833.

[5] A. D. Sakharov, *Violation ofCPin variance,casymmetry, and baryon asymmetry of the universe*, Soviet Physics Uspekhi **34** (1991) 392.

[6] LHCb collaboration, R. Aaij *et al.*, *Observation of CP violation in charm decays*, `arXiv:1903.08726`, submitted to PRL.

[7] V. Weisskopf and E. Wigner, *Berechnung der natürlichen linienbreite auf grund der diracschen lichttheorie*, Zeitschrift für Physik **63** (1930) 54.

[8] LHCb Collaboration, R. Aaij *et al.*, *Measurement of D^0–$\overline{d}^0$ mixing parameters and search for cp violation using $D^0 \to K^+\pi^-$ decays*, Phys. Rev. Lett. **111** (2013) 251801.

[9] CDF Collaboration, T. Aaltonen *et al.*, *Evidence for $D^0 - \overline{d}^0$ mixing using the cdf ii detector*, Phys. Rev. Lett. **100** (2008) 121802.

[10] Belle Collaboration, M. Starič *et al.*, *Evidence for D^0–$\overline{d}^0$ mixing*, Phys. Rev. Lett. **98** (2007) 211803.

[11] BABAR Collaboration, B. Aubert *et al.*, *Evidence for D^0–$\overline{d}^0$ mixing*, Phys. Rev. Lett. **98** (2007) 211802.

[12] T. Pajero, *Measurement of the CP violation parameter A_Γ in $D^0 \to K^+K^-$ and $D^0 \to \pi^+\pi^-$ decays with LHCb Run 2 data*, 2017. Presented 23 Oct 2017.

[13] M. Bobrowski, A. Lenz, J. Riedl, and J. Rohrwild, *How Large Can the SM Contribution to CP Violation in $D^0 - \bar{D}^0$ Mixing Be?*, JHEP **03** (2010) 009, `arXiv:1002.4794`.

[14] Y. Grossman, A. L. Kagan, and Y. Nir, *New physics and CP violation in singly Cabibbo suppressed D decays*, Phys. Rev. D **75** (2007) 036008.

[15] LHCb Collaboration, A. A. Alves *et al.*, *The LHCb Detector at the LHC*, JINST **3** (2008) S08005, Also published by CERN Geneva in 2010.

[16] L. R. Evans and P. Bryant, *LHC Machine*, JINST **3** (2008) S08001. 164 p, This report is an abridged version of the LHC Design Report (CERN-2004-003).

[17] LHCb, *Lhcb webpage*, .

[18] LHCb Outer Tracker Group, R. Arink *et al.*, *Performance of the LHCb Outer Tracker*, JINST **9** (2014) P01002, arXiv:1311.3893.

[19] LHCb, A. A. Alves, Jr. *et al.*, *The LHCb Detector at the LHC*, JINST **3** (2008) S08005.

[20] J. R. Harrison, *Radiation damage studies in the LHCb VELO detector and searches for lepton flavour and baryon number violating tau decays*, PhD thesis, Manchester U., 2014.

[21] W. D. Hulsbergen, *Decay chain fitting with a Kalman filter*, Nucl. Instrum. Meth. **A552** (2005) 566, arXiv:physics/0503191.

[22] LHCb, R. Aaij *et al.*, *Observation of CP violation in charm decays*, arXiv:1903.08726.

[23] F. Betti *et al.*, *Observation of CP violation in charm decays*, .

[24] Particle Data Group, M. Tanabashi *et al.*, *Review of particle physics*, Phys. Rev. **D98** (2018) 030001.

[25] S. Baker and R. D. Cousins, *Clarification of the Use of Chi Square and Likelihood Functions in Fits to Histograms*, Nucl. Instrum. Meth. **221** (1984) 437.

[26] N. L. Johnson, *Systems of frequency curves generated by methods of translation*, Biometrika **36** (1949) 149.

[27] LHCb collaboration, R. Aaij *et al.*, *Precision measurement of the B_s^0–$\overline{B}_s^0$ oscillation frequency in the decay $B_s^0 \to D_s^- \pi^+$*, New J. Phys. **15** (2013) 053021, arXiv:1304.4741.

[28] Heavy Flavor Averaging Group, Y. Amhis *et al.*, *Averages of b-hadron, c-hadron, and τ-lepton properties as of summer 2016*, Eur. Phys. J. **C77** (2017) 895, arXiv:1612.07233, updated results and plots available at https://hflav.web.cern.ch.

[29] A. Jaeger, *Measurement of indirect CP asymmetries in $D^0 \to K^{K^+}$ and $D^0 \to \pi^{\pi^+}$ decays with the LHCb experiment*, 2015. Presented 15 Apr 2015.

[30] LHCb collaboration, R. Aaij *et al.*, *Updated determination of D^0-$\overline{D}^0$ mixing and CP violation parameters with $D^0 \to K^+\pi^-$ decays*, Phys. Rev. **D97** (2018) 031101, arXiv:1712.03220.

[31] LHCb collaboration, R. Aaij *et al.*, *Measurement of the charm-mixing parameter y_{CP}*, Phys. Rev. Lett. **122** (2019) 011802, arXiv:1810.06874.

[32] A. Cerri *et al.*, *Opportunities in Flavour Physics at the HL-LHC and HE-LHC*, arXiv:1812.07638.

[33] LHCb, R. Aaij *et al.*, *Measurement of the CP violation parameter A_Γ in $D^0 \to K^+K^-$ and $D^0 \to \pi^+\pi^-$ decays*, Phys. Rev. Lett. **118** (2017) 261803, arXiv:1702.06490.

[34] LHCb, R. Aaij *et al.*, *Measurement of indirect CP asymmetries in $D^0 \to K^-K^+$ and $D^0 \to \pi^-\pi^+$ decays using semileptonic B decays*, JHEP **04** (2015) 043, arXiv:1501.06777.

[35] Particle Data Group, C. Patrignani *et al.*, *Review of particle physics*, Chin. Phys. **C40** (2016) 100001.

A Approximation of A_Γ as indirect asymmetry

In this chapter all necessary steps are summarised to linearise $\mathcal{A}_{CP}$ and to identify A_Γ as the negative linear slope of $\mathcal{A}_{CP}$.

A.1 Derivation of direct and indirect *CP* asymmetry

Even though this deviation is for D^0 and $\overline{D}^0$ to the *CP* final states $\pi^+\pi^-$ and K^+K^- for simplification the final state f_{CP} in this derivation is denoted as f. The notation of this derivation is inherited from Ref. [12, 35]. The time-dependent *CP* asymmetry is defined by:

$$\mathcal{A}_{CP} := \frac{\Gamma(D^0(t) \to f) - \Gamma(\overline{D}^0(t) \to f)}{\Gamma(D^0(t) \to f) - \Gamma(\overline{D}^0(t) \to f)} \tag{A.1}$$

with the decay width Γ given by

$$\begin{aligned} \Gamma(D^0(t) \to f) &= N_f \left| g_+(t) A_f + \frac{q}{p} g_-(t) \overline{A}_f \right|^2, \\ \Gamma(\overline{D}^0(t) \to f) &= N_f \left| \frac{p}{q} g_-(t) A_f + g_+(t) \overline{A}_f \right|^2 \end{aligned} \tag{A.2}$$

By inserting equation 2.9 into the expression of Γ and using equation 2.13 and equation 2.6 it follows:

$$\begin{aligned} \Gamma(D^0(t) \to f) =& \frac{N_f}{2} e^{-\Gamma t} |A_f|^2 \Big[\left(1 + |\lambda_f|^2\right) \cosh(y\Gamma t) + \left(1 - |\lambda_f|^2\right) \cos(x\Gamma t) \\ &+ 2\mathcal{R}e\left(\lambda_f\right) \sinh(y\Gamma t) - 2\mathcal{I}m\left(\lambda_f\right) \sin(x\Gamma t) \Big] \\ \Gamma(\overline{D}^0(t) \to f) =& \frac{N_f}{2} e^{-\Gamma t} \left|\overline{A}_f\right|^2 \Big[\left(1 + \left|\lambda_f^{-1}\right|^2\right) \cosh(y\Gamma t) + \left(1 - \left|\lambda_f^{-1}\right|^2\right) \cos(x\Gamma t) \\ &+ 2\mathcal{R}e\left(\lambda_f^{-1}\right) \sinh(y\Gamma t) - 2\mathcal{I}m\left(\lambda_f^{-1}\right) \sin(x\Gamma t) \Big] \\ =& \frac{N_f}{2} e^{-\Gamma t} |A_f|^2 \left|\frac{p}{q}\right|^2 \Big[\left(1 + |\lambda_f|^2\right) \cosh(y\Gamma t) - \left(1 - |\lambda_f|^2\right) \cos(x\Gamma t) \\ &+ 2\mathcal{R}e\left(\lambda_f\right) \sinh(y\Gamma t) + 2\mathcal{I}m\left(\lambda_f\right) \sin(x\Gamma t) \Big] \end{aligned} \tag{A.3}$$

This expression can now be inserted into the definition of $\mathcal{A}_{CP}$.

$$
\begin{aligned}
\mathcal{A}_{CP}(t) = &\Big[\left(R_m^2 - 1\right) \left(1 + |\lambda_f|^2\right) \cosh(y\Gamma t) + \left(R_m^2 + 1\right) \left(1 - |\lambda_f|^2\right) \cos(x\Gamma t) \\
&+ 2 \left(R_m^2 - 1\right) \mathcal{R}e\left(\lambda_f\right) \sinh\left(y\Gamma t\right) - 2 \left(R_m^2 + 1\right) \mathcal{I}m\left(\lambda_f\right) \sin\left(x\Gamma t\right) \Big] / \\
&\Big[\left(R_m^2 + 1\right) \left(1 + |\lambda_f|^2\right) \cosh(y\Gamma t) + \left(R_m^2 - 1\right) \left(1 - |\lambda_f|^2\right) \cos(x\Gamma t) \\
&+ 2 \left(R_m^2 + 1\right) \mathcal{R}e\left(\lambda_f\right) \sinh\left(y\Gamma t\right) - 2 \left(R_m^2 - 1\right) \mathcal{I}m\left(\lambda_f\right) \sin\left(x\Gamma t\right) \Big]
\end{aligned}
\tag{A.4}
$$

The above equation can be simplified to the following expression, assuming small mixing parameters x and y:

$$
\mathcal{A}_{CP}(t) = \mathcal{A}_{CP}^{\text{dir}} + \mathcal{A}_{CP}^{\text{ind}} \cdot \Gamma t + \mathcal{O}((x\Gamma t)^2) + \mathcal{O}((y\Gamma t)^2) \tag{A.5}
$$

where $\mathcal{A}_{CP}^{\text{dir}}$ is constant over time and only non-zero if CP violation in decay is present ($R_f \neq 1$), whereas the slope of $\mathcal{A}_{CP}$ is given by:

$$
\mathcal{A}_{CP}^{\text{ind}} := -\frac{2\eta_{CP}(f)R_f^2}{(1 + R_f^2)^2} \left[(R_m R_f + R_m^{-1} R_f^{-1}) y \cos\phi_f - (R_m R_f + R_m^{-1} R_f^{-1}) x \sin\phi_f\right] \tag{A.6}
$$

A.2 Simplification of A_Γ as indirect asymmetry

A_Γ is defined as the asymmetry between the effective lifetimes of initially produced D^0 and $\overline{D}^0$ mesons decaying into CP-even final states:

$$
A_\Gamma := \frac{\hat{\tau}(\overline{D}^0 \to f) - \hat{\tau}(D^0 \to f)}{\hat{\tau}(\overline{D}^0 \to f) + \hat{\tau}(D^0 \to f)} = \frac{\hat{\Gamma}(D^0 \to f) - \hat{\Gamma}(\overline{D}^0 \to f)}{\hat{\Gamma}(D^0 \to f) - \hat{\Gamma}(\overline{D}^0 \to f)} \tag{A.7}
$$

$\hat{\tau} = 1/\hat{\Gamma}$ is the effective lifetime as obtained from the decay-time spectrum by an exponential decay law. For the calculation of A_Γ is it possible to simplify equation A.3 to the following expression by assuming small mixing parameters x and y.

$$
\begin{aligned}
\Gamma(D^0(t) \to f) &= \mathcal{N}_f e^{-\Gamma t} \left|A_f\right|^2 \left[1 + \mathcal{R}e(\lambda_f) y\Gamma t - \mathcal{I}m(\lambda_f) x\Gamma t + \mathcal{O}((x\Gamma t)^2) + \mathcal{O}((y\Gamma t)^2)\right] \\
\Gamma(\overline{D}^0(t) \to f) &= \mathcal{N}_f e^{-\Gamma t} \left|\overline{A}_f\right|^2 \left[1 + \mathcal{R}e(\lambda_f^{-1}) y\Gamma t - \mathcal{I}m(\lambda_f^{-1}) x\Gamma t + \mathcal{O}((x\Gamma t)^2) + \mathcal{O}((y\Gamma t)^2)\right]
\end{aligned}
\tag{A.8}
$$

Expanding λ_f according to $\lambda_f = -\eta_{CP}(f) \cdot R_m R_f e^{i\phi_f}$, one obtains:

$$
\begin{aligned}
\Gamma(D^0(t) \to f) &\approx \mathcal{N}_f e^{-\Gamma t} \left|A_f\right|^2 \left[1 - \eta_{CP}(f) \mathrm{R}_m \mathrm{R}_f \left(y \cos\phi_f - x \sin\phi_f\right) \Gamma t\right] \\
\Gamma(\overline{D}^0(t) \to f) &\approx \mathcal{N}_f e^{-\Gamma t} \left|\overline{A}_f\right|^2 \left[1 - \eta_{CP}(f) \mathrm{R}_m^{-1} \mathrm{R}_f^{-1} \left(y \cos\phi_f + x \sin\phi_f\right) \Gamma t\right]
\end{aligned}
\tag{A.9}
$$

With help of the relation $e^{-\Gamma t}(1 - z\Gamma t + \mathcal{O}((z\Gamma t)^2)) \approx e^{-\hat{\Gamma} t}$, which is valid for small z, is it possible to approximate the time-dependency of Γ at first order by a exponential function, defining the effective decay width $\hat{\Gamma} := \Gamma(1 + z)$ follows:

$$\begin{aligned}\hat{\Gamma}(D^0(t) \to f) &= \mathcal{N}_f e^{-\Gamma t} \left|A_f\right|^2 \left[1 + \eta_f^{CP} \mathrm{R}_m \mathrm{R}_f \left(y \cos\phi_f - x \sin\phi_f\right) \Gamma t\right] \\ \hat{\Gamma}(\overline{D}^0(t) \to f) &= \mathcal{N}_f e^{-\Gamma t} \left|\overline{A}_f\right|^2 \left[1 + \eta_f^{CP} \mathrm{R}_m^{-1} \mathrm{R}_f^{-1} \left(y \cos\phi_f + x \sin\phi_f\right) \Gamma t\right]\end{aligned} \tag{A.10}$$

Inserting the effective decay-width now in equation A.7 yields:

$$A_\Gamma = \frac{\eta_{CP}(f)}{2} \left[(R_m R_f + R_m^{-1} R_f^{-1}) y \cos\phi_f - (R_m R_f + R_m^{-1} R_f^{-1}) x \sin\phi_f\right] \tag{A.11}$$

By inserting $\mathcal{A}_{CP}^{\mathrm{ind}}$ and assuming a small contribution of R_f [22] can A_Γ be simplified in the following way:

$$A_\Gamma = -\frac{1}{4} \frac{\left(1 + R_f^2\right)^2}{R_f^2} \cdot \mathcal{A}_{CP}^{\mathrm{ind}} \approx -\mathcal{A}_{CP}^{\mathrm{ind}} \tag{A.12}$$

B Additional Material on mass fits

In the following the mass spectrums for each decay-time bin, respectively for D^0 and $\overline{D}^0$, with fit projection overlaid are shown.

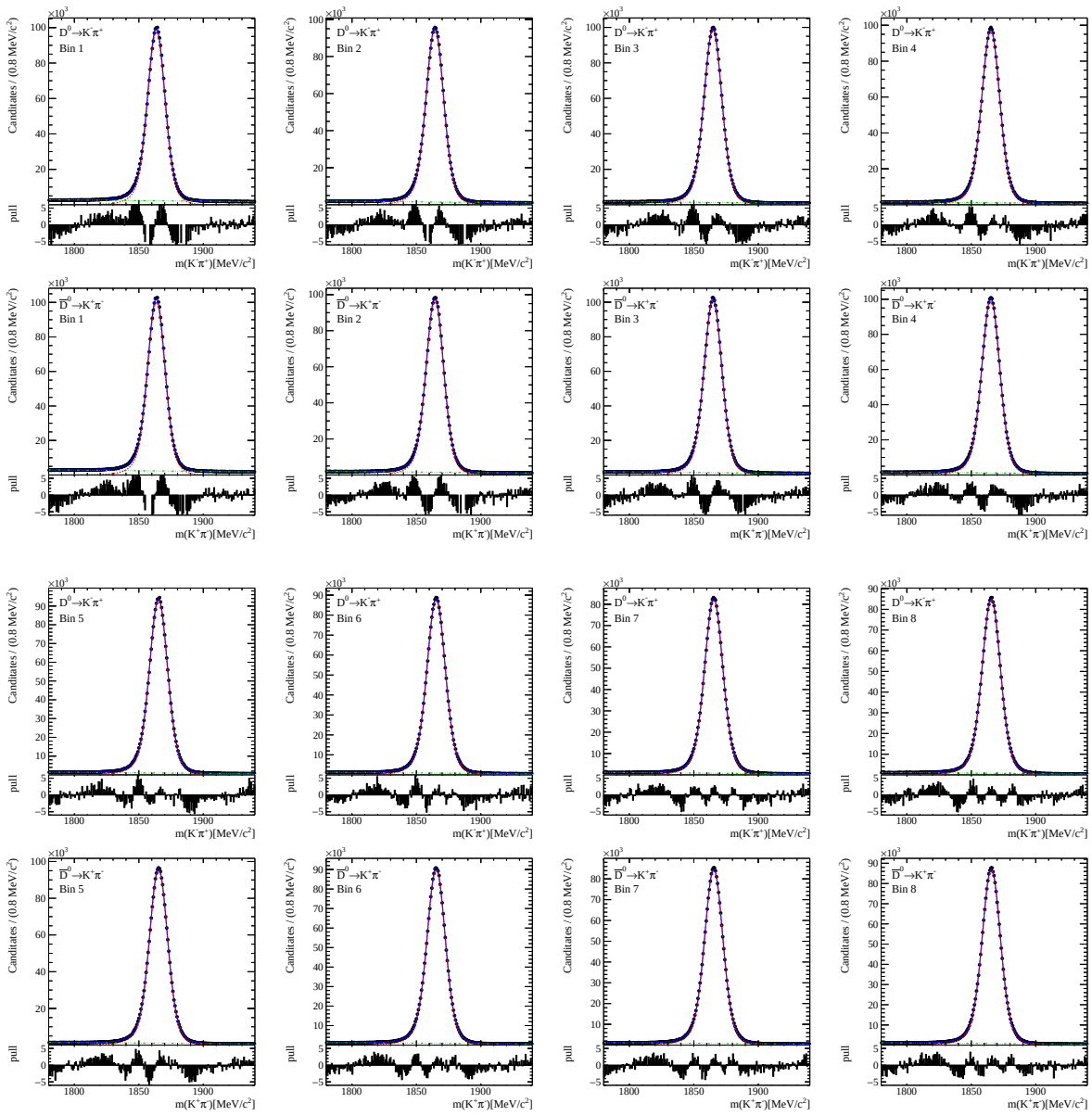

Figure 31: Mass fits in the decay time bins for $D^0 \to K^-\pi^+$ decays (bins 1-8).

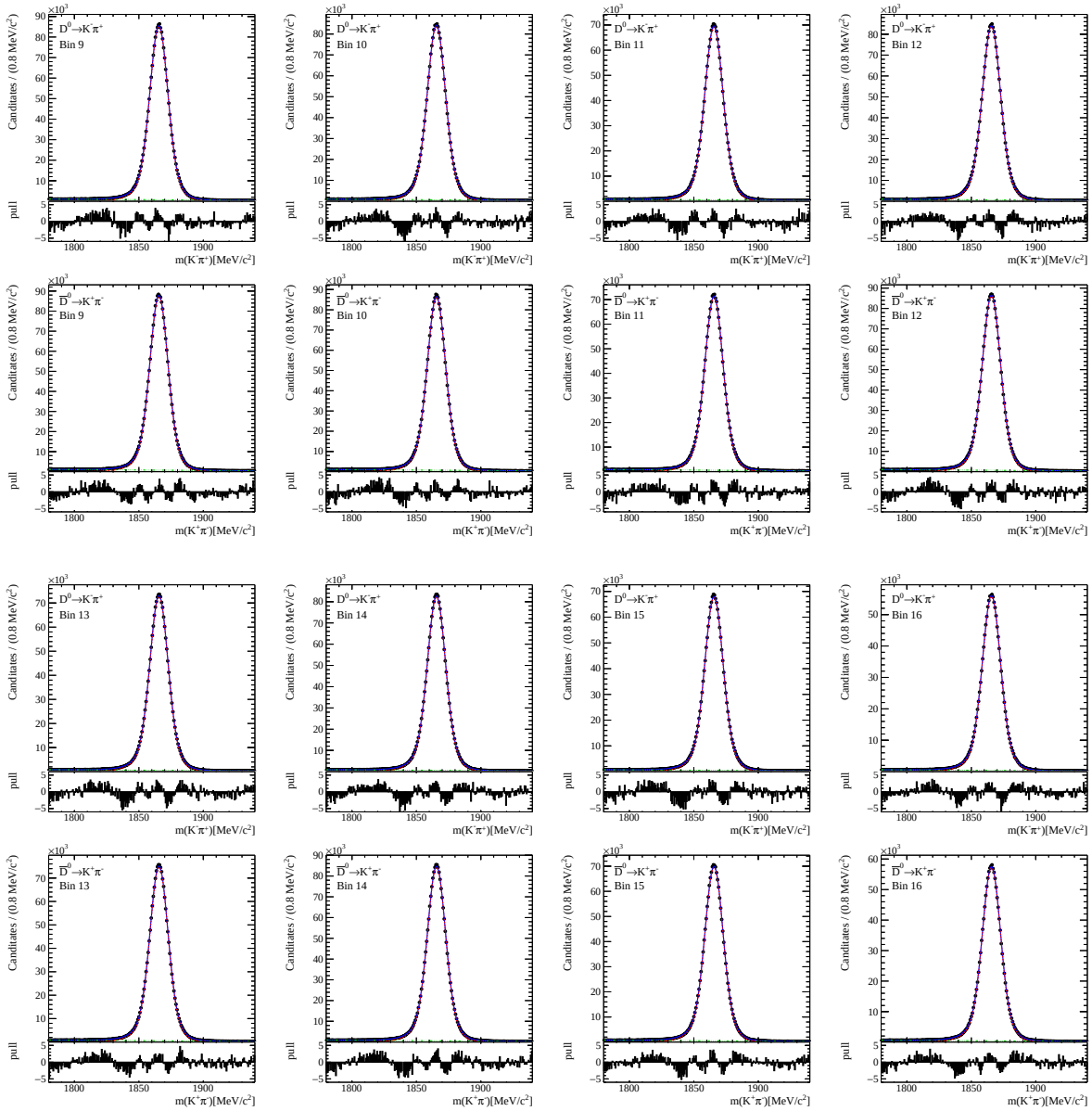

Figure 32: Mass fits in the decay time bins for $D^0 \to K^-\pi^+$ decays (bins 9-16).

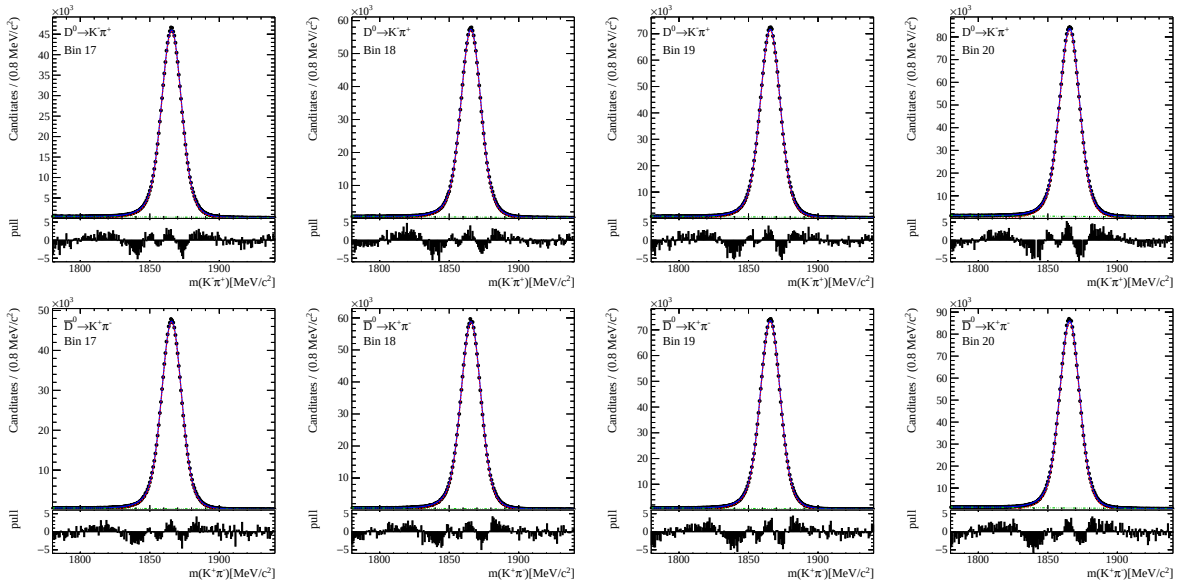

Figure 33: Mass fits in the decay time bins for $D^0 \to K^-\pi^+$ decays (bins 16-20).

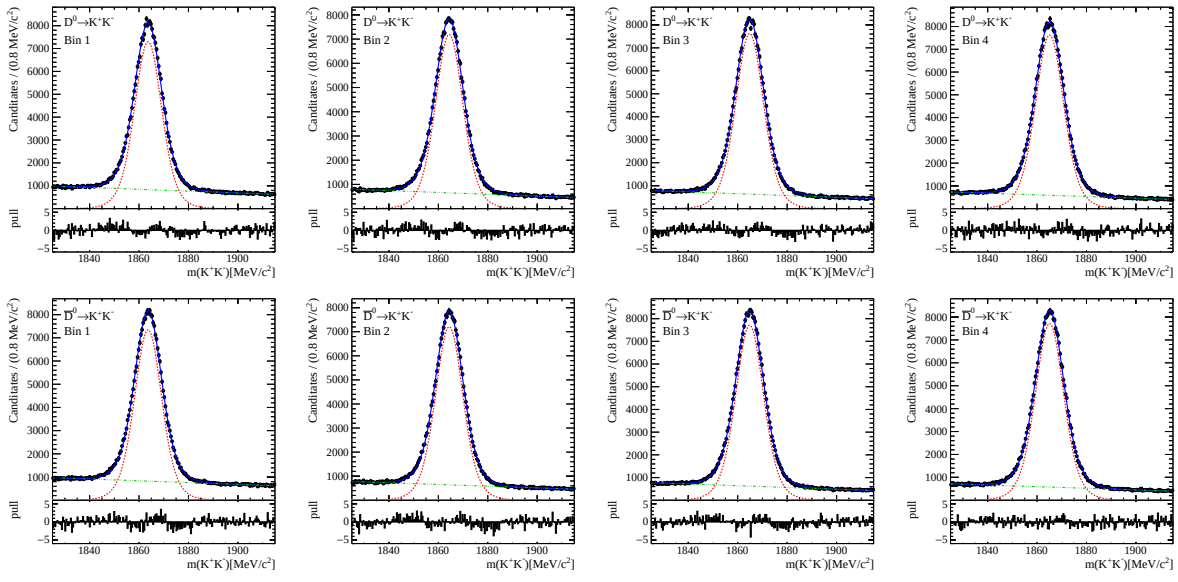

Figure 34: Mass fits in the decay time bins for $D^0 \to K^+K^-$ decays (bins 1-4).

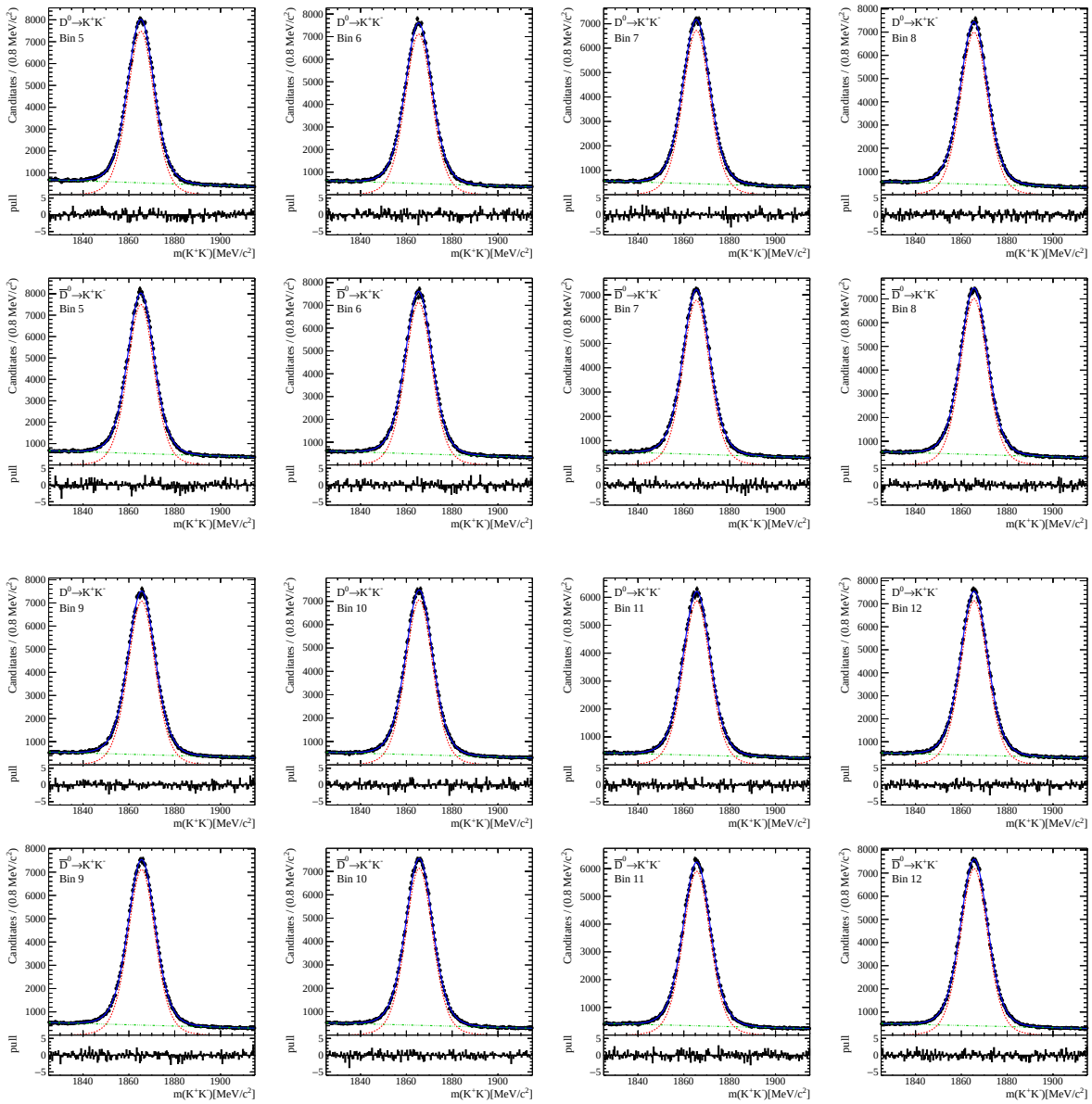

Figure 35: Mass fits in the decay time bins for $D^0 \to K^+K^-$ decays (bins 5-12).

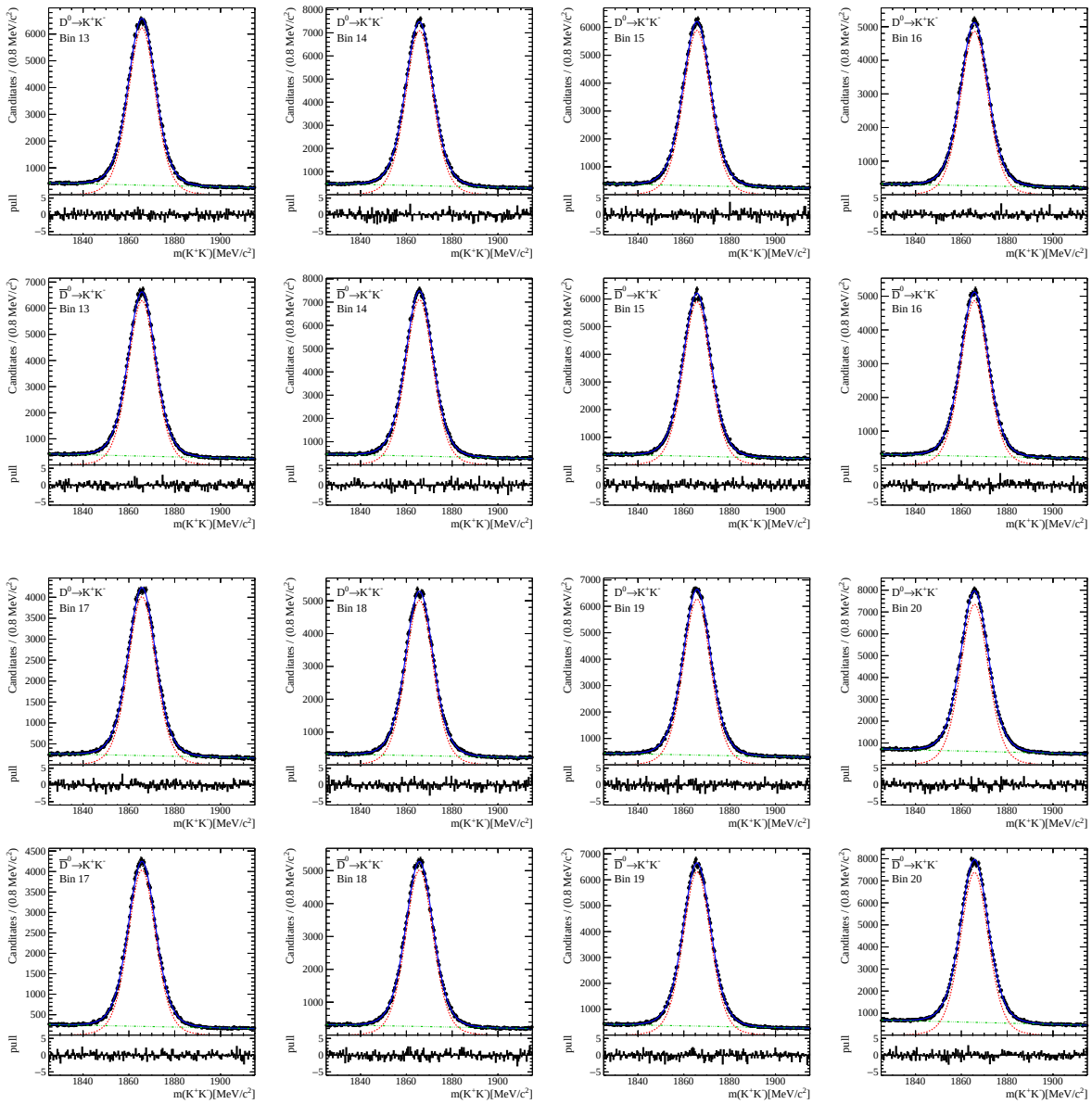

Figure 36: Mass fits in the decay time bins for $D^0 \to K^+K^-$ decays (bins 13-20).

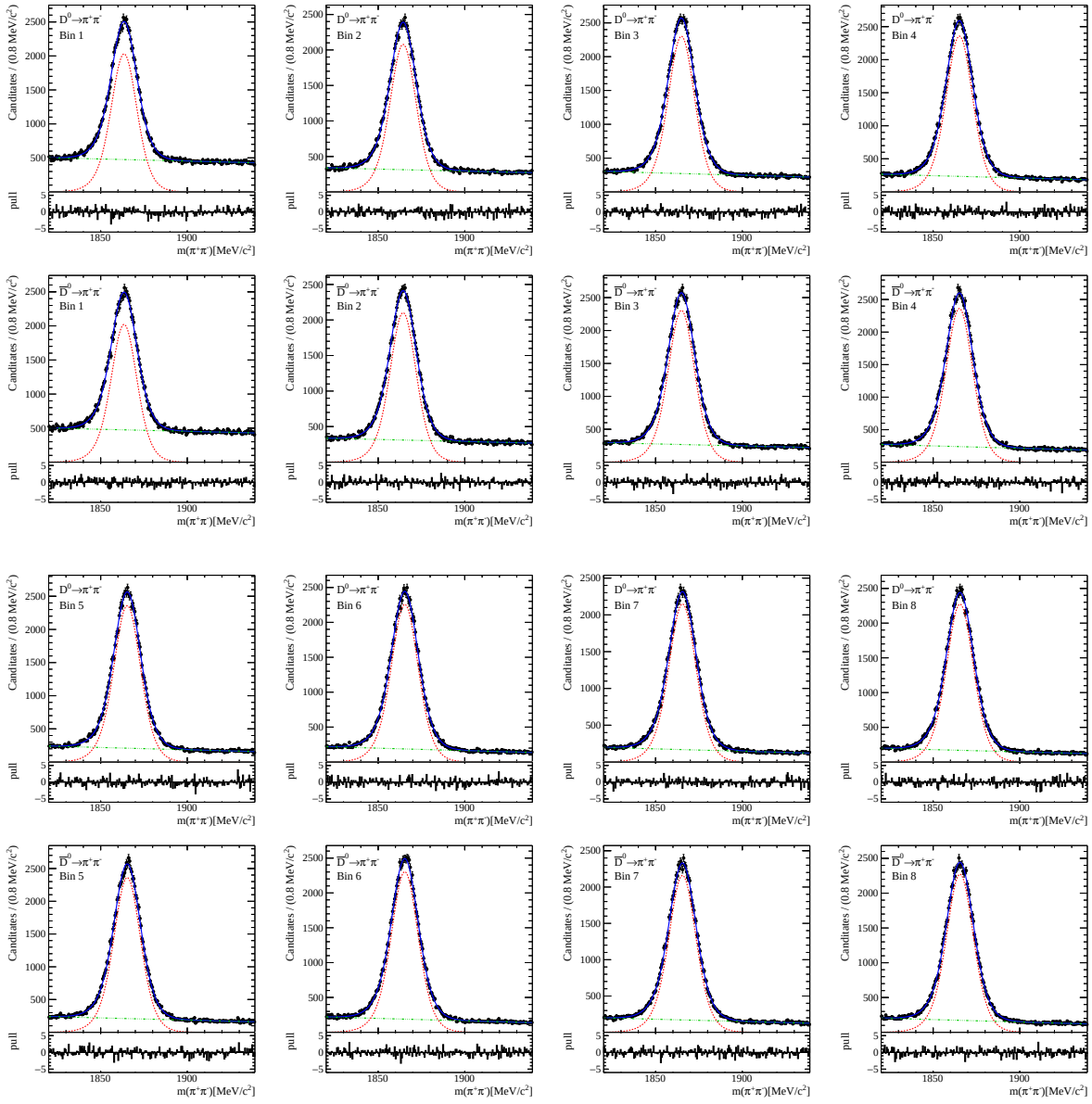

Figure 37: Mass fits in the decay time bins for $D^0 \to \pi^+\pi^-$ decays (bins 1-8).

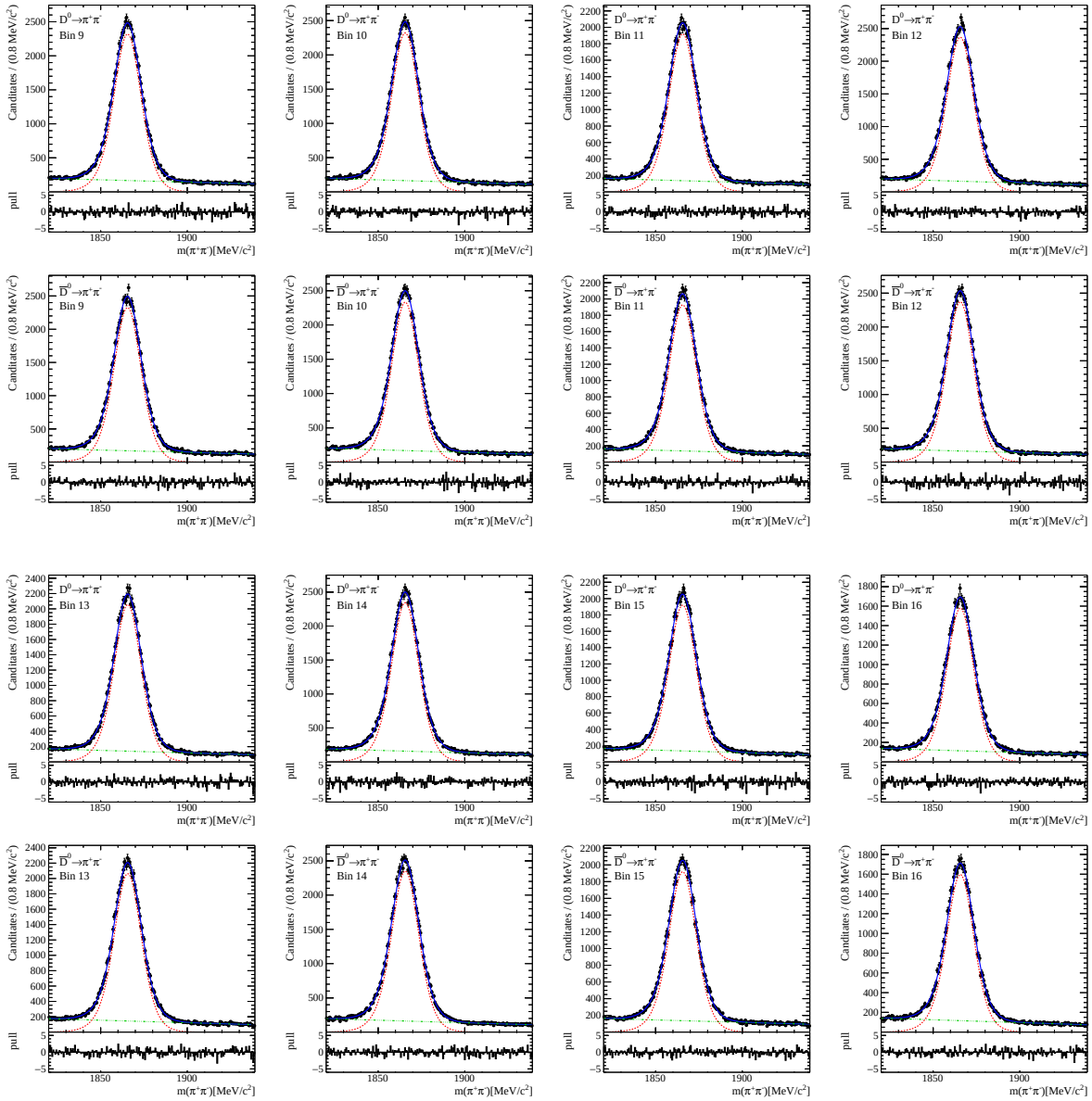

Figure 38: Mass fits in the decay time bins for $D^0 \to \pi^+\pi^-$ decays (bins 9-16).

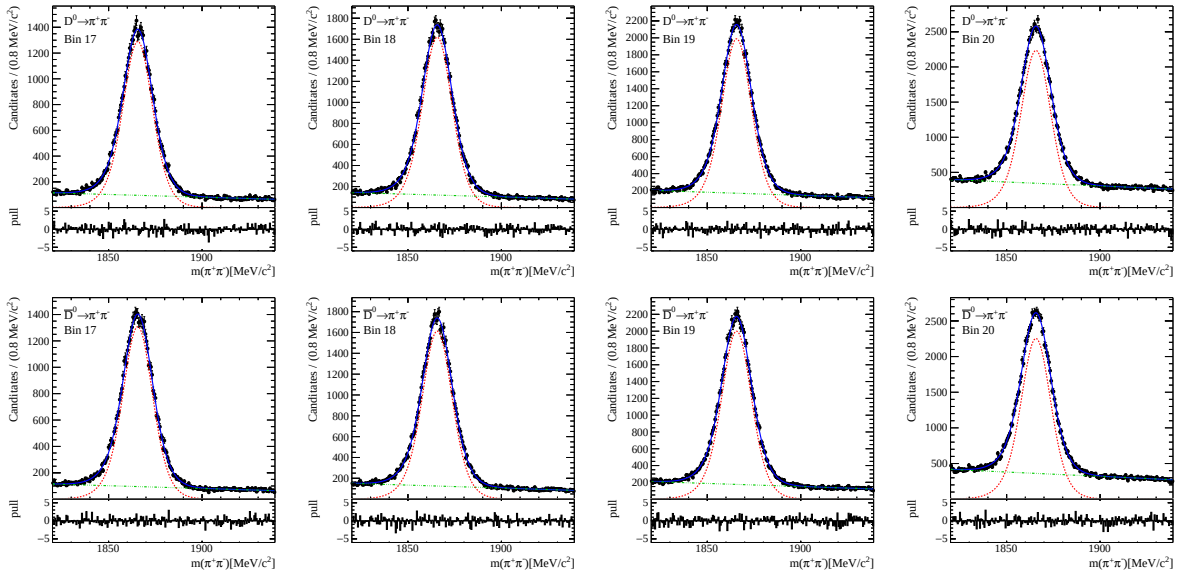

Figure 39: Mass fits in the decay time bins for $D^0 \to \pi^+\pi^-$ decays (bins 17-20).

C Fit results in each decay-time bin

In the following the fit results for all decay-time bins are summarised.

The scale factors for the width of the signal distributions and the shift of the mean as determined in the individual decay-time bins are shown in figure 40. All further parameters which are free to float in the decay-time binned fits (N_{sig}, N_{bkg}, $\mathcal{A}_{\mathrm{raw}bkg}$) are shown in figure 41.

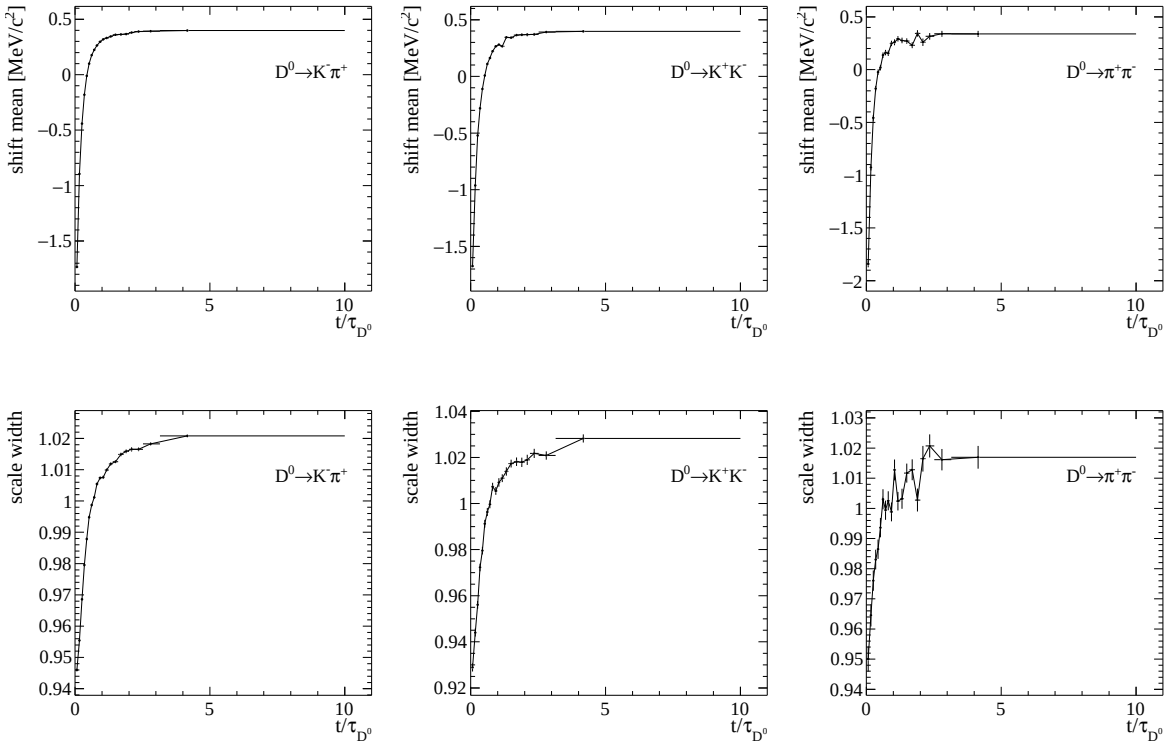

Figure 40: Shift of the mean position (top) and scale factor for the width (bottom) as obtained in the decay time binned fits for $D^0 \to K^-\pi^+$ (left row), $D^0 \to K^+K^-$ (middle row) and $D^0 \to \pi^+\pi^-$ (right row).

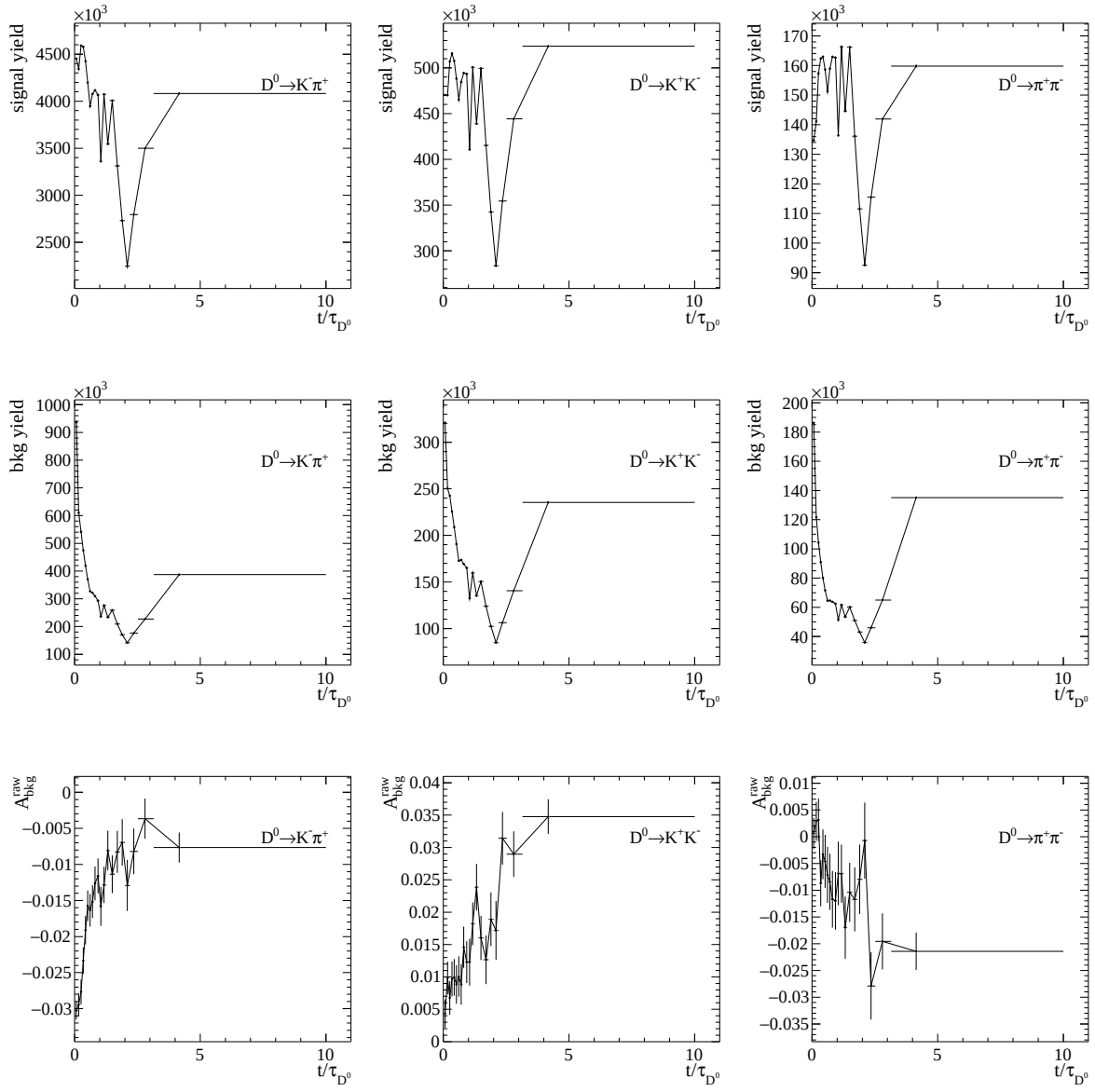

Figure 41: Signal yields (top column), background yields (middle column) and background raw asymmetries (bottom column) as obtained in the decay-time binned fits for $D^0 \to K^-\pi^+$ (left row), $D^0 \to K^+K^-$ (middle row) and $D^0 \to \pi^+\pi^-$ (right row).

D Additional material concerning the binning scheme and the average decay-time in each bin

In the following the binning scheme used for this analysis is summarised, including the average decay-time in each decay-time bin (table 7). Additional, all plots regarding the test of different binning schemes are shown (figure 42).

bin	decay-time range $[t/\tau_{D^0}]$	average decay-time $\langle t \rangle$ $[t/\tau_{D^0}]$
1	[0.00,0.12]	0.07
2	[0.12,0.21]	0.17
3	[0.21,0.30]	0.26
4	[0.30,0.39]	0.34
5	[0.39,0.48]	0.43
6	[0.48,0.57]	0.52
7	[0.57,0.66]	0.61
8	[0.66,0.76]	0.72
9	[0.76,0.87]	0.81
10	[0.87,0.99]	0.93
11	[0.99,1.10]	1.04
12	[1.10,1.25]	1.17
13	[1.25,1.40]	1.32
14	[1.40,1.60]	1.50
15	[1.60,1.80]	1.70
16	[1.80,2.00]	1.90
17	[2.00,2.20]	2.10
18	[2.20,2.52]	2.35
19	[2.52,3.15]	2.80
20	[3.15,10.0]	4.19

Table 7: Decay-time binning and average decay-time per bin. The same average decay time is found for each decay channel.

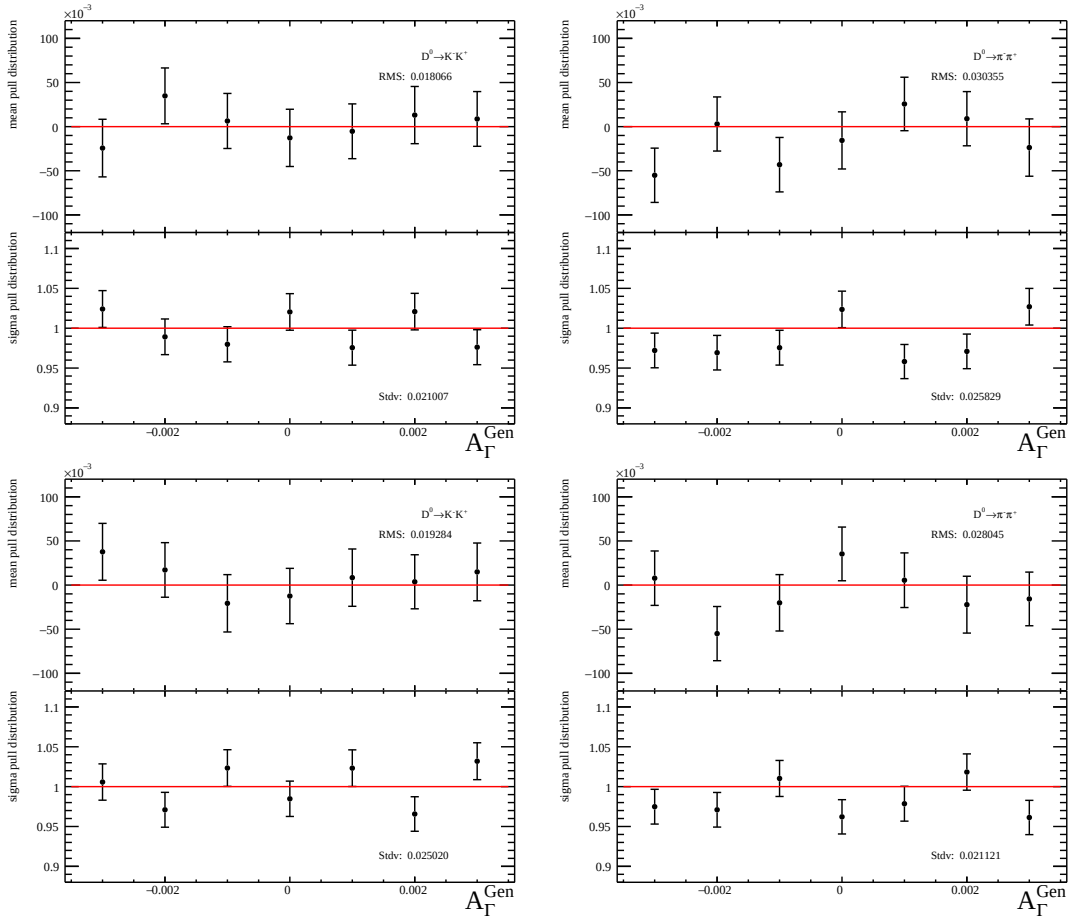

Figure 42: Systematic study of the effect due to the specific choice of the binning. Shown are the pull mean and width for different binning schemes for independently generated pseudo experiments. The top row corresponds to 15 decay-time bins the bottom row to 25 decay-time bins.

E Additional material on toy experiments

In the following the pull distributions for the validation of the fit, with a normal distribution overlaid, for the different values of A_Γ^{Gen} are shown.

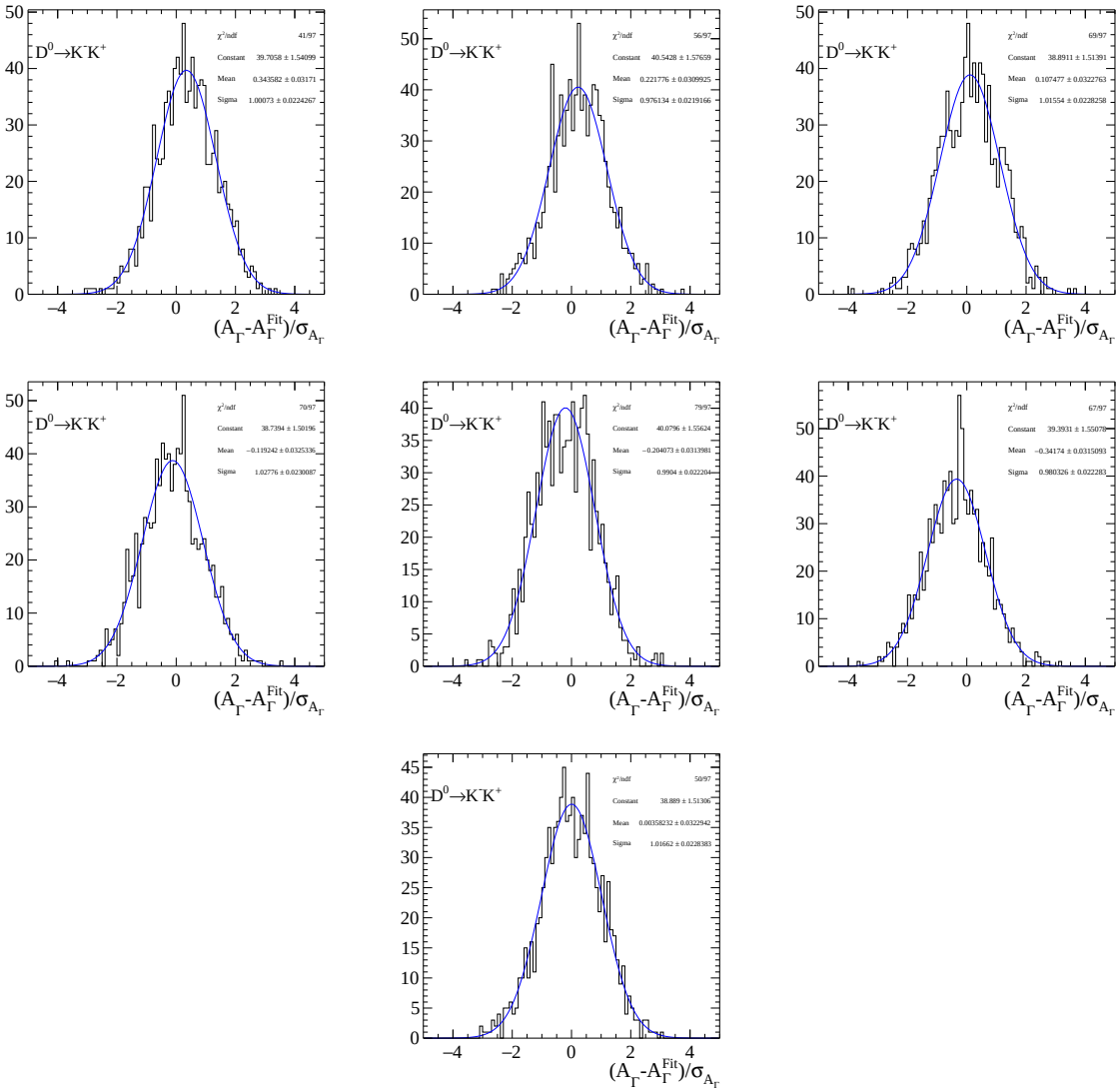

Figure 43: Pull distributions as obtained in the $D^0 \to K^+K^-$ pseudo experiments described in section 6 for (top row from left to right) $A_\Gamma = -0.003, -0.002, -0.001$, (middle row from left to right) $A_\Gamma = 0.001, 0.002, 0.003$) and (bottom row) $A_\Gamma = 0$.

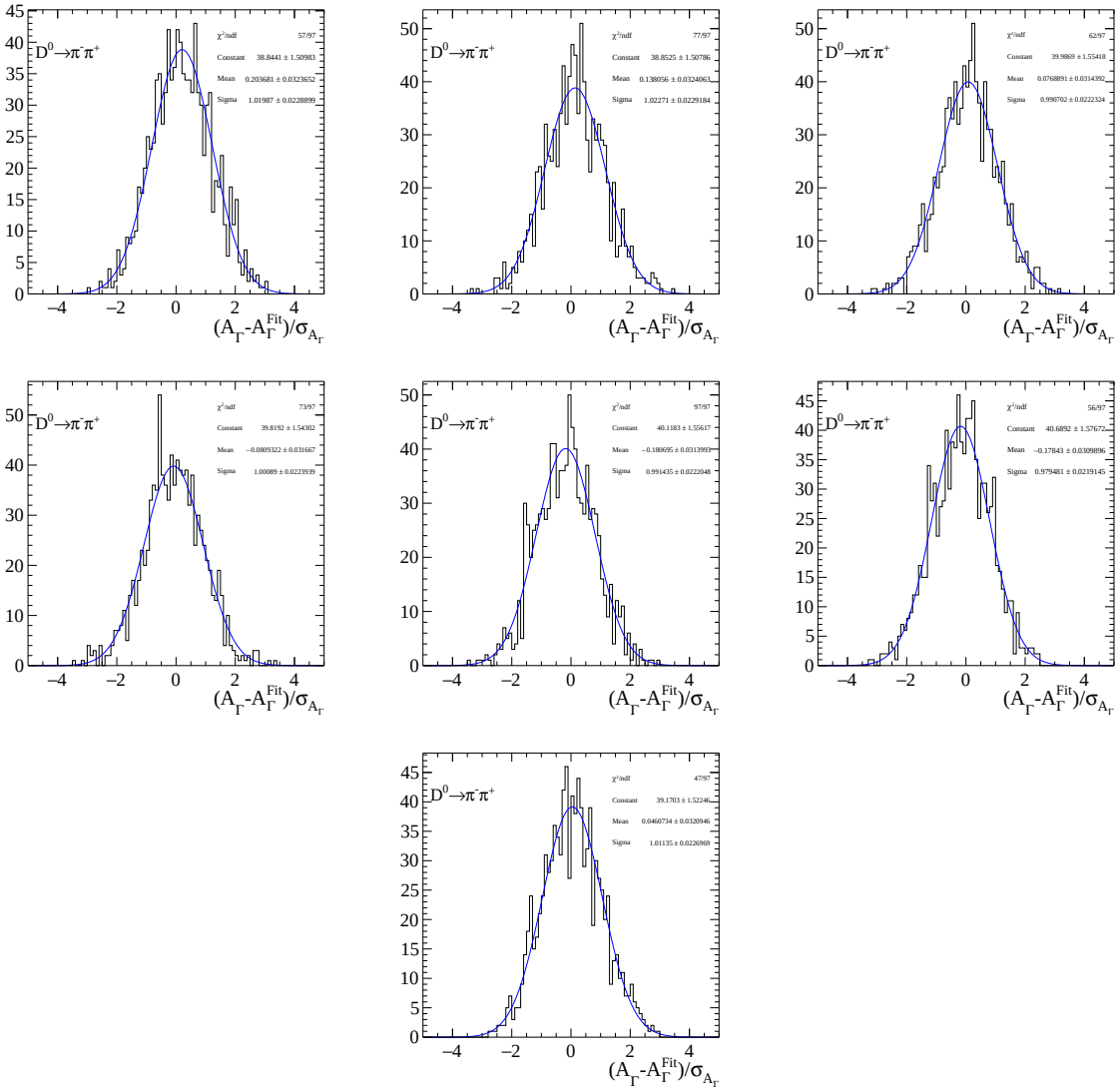

Figure 44: Pull distributions as obtained in the $D^0 \to \pi^+\pi^-$ pseudo experiments described in section 6 for (top row from left to right) $A_\Gamma = -0.003, -0.002, -0.001$, (middle row from left to right) $A_\Gamma = 0.001, 0.002, 0.003$) and (bottom row) $A_\Gamma = 0$.

Eigenständigkeitserklärung

Hiermit bestätige ich, dass ich die vorliegende Arbeit selbständig verfasst habe und keine anderen als die angegebenen Quellen und Hilfsmittel benutzt habe.

Unterschrift .....